The University Of Sheffield.

Unified Sensing, Diagnosis and Active Self-Healing

A thesis submitted in partial fulfillment of the requirements for the degree of Doctor of Philosophy

Kuponu Oluwafemi Sedoten

Department of Automatic Control and Systems Engineering

The University of Sheffield, UK

March 2018

This thesis is dedicated to God, my wife, daughter, parents and sibling.

Declaration

I, Kuponu Oluwafemi Sedoten, confirm that the work presented in this thesis is my own. Where information has been derived from other sources, I confirm that this has been indicated in the work.

Kuponu Oluwafemi Sedoten

March 2018

Acknowledgements

My utmost gratitude to the Almighty God for the success of this doctoral programme.

A big thank you to my lovely wife for her great support and perseverance all through the programme.

To my parents and sibling, I am indebted for the prayers, support and the platform provided to build on.

I would like to thank Dr. Simon Pope for supervising this project. I have benefited immensely from your support and guidance, and for this, am grateful. Many thanks to Professor Visakan Kadirkamanathan and Dr. Bishakh Bhattacharya for their role in this project. I would also like to express my gratitude to Mr. Craig Bacon for setting up the laboratory for this project.

I like to thank my research colleagues for the great conversations and feedbacks. You have provided building blocks on which this project has been developed.

Finally, I would like to acknowledge the financial support of the Department of Automatic Control and Systems Engineering of the University of Sheffield and the Lagos State Government all through my programme.

Abstract

The application of self-healing material in industrial systems has the potential to improve reliability and save cost. This is because faults do occur in systems, and for life critical or remote or difficult to access ones, current maintenance practices may be insufficient. When such systems are self-healed, the materials making up the systems regain some or all of its lost physical properties to keep the systems functioning. However, a majority of self-healing approaches are not yet at the level of industrial integration. These self-healing approaches are passive and do not guarantee a match between the damage and healing rate. A significant step in their advancement is the development of an integrated sensing, fault diagnosis and active self-healing system, which is the focus of this thesis.

A mathematical model based on a previously experimented electromechanical self-healing process, whose healing mechanism combines piezoelectricity and electrolysis is developed. The model demonstrates the poor match between the damage and healing rate due to the ineffectiveness of the healing process to counteract the onset of damage, the dominant effect of uncertainties and disturbances on the healing process, the dependence of healing on the location of the healing mechanism relative to the fault location, etc. In addition, nonlinearities, such as the inherent dead-zone of the chosen healing mechanism affect the response of the healing process. The model also provides a benchmark for the work in this thesis.

The model is then the foundation for the development of a novel active self-healing system. This is a closed loop system that takes advantage of sensing and adaptive sliding mode feedback control with the modelled healing mechanism to achieve a desired response. Importantly, it is shown in simulation

that adaptive feedback control (sliding mode control) can minimize the effect of uncertainties, regulate the healing rate of a self-healing system to meet user or environmental demands, such as the damage rate, and compensate for the non-linear dead-zone associated with this healing mechanism.

Finally, a novel fault diagnosis method that combines the beam curvature, proportional orthogonal decomposition, Hölder exponent and supervised regression is presented as a step to define the environmental demands. This essentially captures the effect of damage of a beam structure. It is combined with the active self-healing system, leading to a novel framework for an integrated sensing, fault diagnosis and closed loop active self-healing system. It is shown through simulation that the proposed active system can potentially estimate the damage rate, provide adequate actuation to match the healing rate with the estimated damage rate and provide real time insight into the healing dynamics.

Table of Contents

List of Figures

List of Tables

Nomenclature

List of Acronyms

AC	Alternating current
CFRP	Carbon fibre reinforced plastic
DA	Diels-Alder
DC	Direct current
FRP	Fibre reinforced plastic
MIAC	Model identification adaptive control
MRAC	Model reference adaptive control
NRMSE	Normalised root mean square error
POD	Proportional orthogonal decomposition
PVDF	Poly vinylidene fluoride
PVDF-HFP	Poly vinylidene fluoride-co-hexafluropropylene
PZT	Lead Zirconate Titanate
rDA	retro-Diels-Alder
SMC	Sliding mode control
SMP	Shape memory polymer
TP	Thermoplastic polymer
TRL	Technological readiness level

List of Symbols

α	Hölder exponent
χ	Dimension $N \times n_o$
$\dot{Q}_a$	Actual current
$\dot{Q}_d$	Desired current or reference model
ϵ_{33}^T	Dielectric permittivity
η_a	Anode over-potentials
η_c	Cathode over-potentials
η_{ohmic}	Ohmic resistance
$\hat{E}_{rev}$	E_{rev} estimate
κ	Radius of curvature of beam
λ_c, k^*, ϵ	Control design parameters
ω	Natural frequency of beam
ρ	Density of beam
ρ_c, η, K_d	Control design parameters
ρ_{sh}	Density of healing agent
Θ	Stiffness of beam
$\tilde{\phi}, \hat{V}_{p^r}$	Adaptive control parameters
φ	Spatial basis function
ϑ	Dimension $n_o \times 1$
ζ	Weightings
A	Cross sectional area of beam
a	Crack depth
A_n	Noise amplitude
A_p	Cross-sectional area of piezoelectric material
a_{est}	Estimated crack depth
b	Translational parameter
c^d	Unknown amplitudes of damaged signal
c^u	Unknown amplitudes of undamaged signal
c_k	Unknown amplitude of signal
C_p	Capacitance of piezoelectric material

D_3	Electric displacement
d_{33}	Coupling coefficient of a piezoelectric material
E	Young's modulus of beam
$E(x,t)$	Error signal
E_3	Electric field
E_p	Young's modulus of piezoelectric material
E_{rev}	Reversible potential
$f(t)$	Applied force
g	Gain
h	Depth of beam
h_p	Piezoelectric patch thickness
I	Second moment of inertia of beam
$index(t)$	Monitoring index at time t
k_p	Stiffness of piezoelectric material
L	Length of beam
l_1	Crack location
l_{est}	Estimated crack location
m	Positive slope
M_p	Mass of piezoelectric stack
$M_{c_{est}}$	Estimated mass
N	Hölder coefficient
n	Number of modes
Q_p	Total piezoelectric Charge
R_p	Piezoelectric stack resistance
s	Sliding surface
S_3	Strain
s_w	Scaling parameter
s_{33}^E	Compliance constant
s_ϵ	Tuning error
t	Time
T_3	Stress

t_f	Fault time
U	Control input
V	Applied voltage
v	Poisson's ratio
V_p	Piezo-induced voltage
$V_{f_{est}}$	Estimated volume
V_{p^r}	Smooth DC piezo-induced voltage
W	Lyapunov function
w	Width of beam
W_f	Wavelet transform
$x(t)$	Relative stack displacement of piezoelectric material
Y	Deflection of beam
Y_l	Left deflection of beam
Y_r	Right deflection of beam
z	Number of piezoelectric layers

Chapter 1

Introduction

1.1 Introduction

In-service engineering systems are constantly exposed to conditions that cause gradual degradation of the material composition of the systems (Dash and Venkatasubramanian, 2000; Venkatasubramanian, 2005). The conditions could be environmental or physical, e.g. the turbulence, earthquake or unwanted vibrations, collision with debris or other systems, human error etc.; it could also be chemical or electrical conditions e.g. electric sparks, corrosion, fire, etc. These eventually lead to faults such as cracks in systems like airliners, ships, pipelines, bridges, satellites, buildings, etc. In order to prevent these faults and extend the remaining useful life of engineering systems, maintenance strategies are usually put in place. Traditionally, this includes schedule-based and condition-based maintenance. These strategies improve reliability, prevent environmental hazards and maximize profit returns on system utility. In schedule-based maintenance, industries employ periodic assessment of engineering systems to maximize system utility. Maintenance is carried out by a team of specialists but this approach is quite passive because failure can occur before the schedule period and may lead to damages as well as financial loss. Condition-based maintenance is achieved by observing certain dynamics of a system using different techniques like fault detection and diagnosis to

make decisions as to when maintenance is carried out. This is a proactive approach that dictates what, how, where and when to carry out maintenance; and it potentially provides a closer to optimal solution. However, effective and reliable implementation requires proven and tested sensing and signal processing solutions.

Despite these maintenance strategies, systems still experience faults during operation. This could be as a result of wear and tear, negligence on the part of the maintenance team, disturbances, incipient faults that cannot be easily identified or a newly developed fault during operations. The effect of these faults (partial or total) can be minimal or catastrophic to normal operations, environment or human lives. The implication of any downtime can also lead to financial costs or inconvenience. Examples include fragmentation of an in-flight China airline flight 611 aircraft caused by human negligence (Aviation Safety Council, 2005); removal of Delta flight 2412 aircraft wing panel due to undetected incipient fault (Smith and Janet DiGiacomo, 2014); Rena Plaza Factory collapse caused by cracks (with over 1000 lives lost) (BBC, 2013); pipeline oil spill caused by undetected incipient cracks and human negligence, resulting to environmental hazard and high clean-up cost (National Transportation Safety Board, 2010). The severity of fault may be disastrous, particularly for systems that are life critical or are difficult and/or remotely accessed. Examples include airliners, buildings, bridges, satellites, ships, turbines, nuclear reactors, underground infrastructures such as tubes, water or gas pipes, etc. This challenge indicates a need for a more robust approach (temporary or permanent), particularly for systems that cannot be easily stopped during operations. A way to do this is to introduce self-healing, whereby materials or components of a system can recover full or partial functionality in event of a fault through healing. This would be particularly useful as composite materials have seen increased usage in these kinds of systems because of its lightness, resistance to damage, cost efficiency, environmental impact, etc. Composite material constitutes about 50% of the total material of

a Boeing 787 Dreamliner (Hale, 2006) and composite turbine blades are starting to replace metallic ones. The proposed self-healing material can potentially offer economic and environmental benefits, improve reliability and avert disastrous event that could be life threatening. Hence, a critical look at self-healing in this thesis.

1.2 Literature Review on Self-healing Materials

Self-healing materials are inspired by the healing capabilities of biological organisms. For example, blood clots are formed around a cut in the skin before triggering transportation of cells, oxygen and nutrients towards the cut. These help to build new tissues and eventually heal the cut. In materials, healing leads to improved material properties that have been affected by damage. A vast range of material properties can be healed but notable ones are mechanical properties such as Young's modulus or stiffness, hardness, tensile strength etc. Experimental investigation of self-healing includes the use of materials such as polymers, metals and ceramics (Hager et al., 2010). With a few exceptions (e.g. paints (Hager et al., 2010)), most reported self-healing works are in technological readiness levels (TRL) 1 to 3, i.e. basic concept to laboratory use (Blaiszik et al., 2010). Nonetheless, interest in self-healing materials is growing (Hall et al., 2015; Huang et al., 2016; Huyang et al., 2016; Huyang and Sun, 2016; Ivanov and Stabnikov, 2017; Kessler, 2007; Mignon et al., 2017b; Sherir et al., 2016; Trask et al., 2013; Wang et al., 2016; Wen et al., 2016; Wu et al., 2016a,b). For example, Burattini et al. (2009) demonstrated the capability of non-covalent interaction of a polymer to self-heal after a fracture; Wu et al. (2015) developed a self-healing dental composite that can heal cracks; Mignon et al. (2017a) worked on developing materials with self-healing potential; Soroushian et al. (2012) and Sayayr et al. (2014) investigated the potential of electromechanical materials for self-healing, etc. Self-healing materials are generally categorised

as intrinsic or extrinsic and can be autonomic or non-autonomic in the way healing is initiated (Blaiszik et al., 2010; Frei et al., 2013; Hager et al., 2010).

1.2.1 Intrinsic Self-healing

In intrinsic self-healing, materials are healed through chemical reactions at the vicinity of the damage. The reaction causes a fill-up at the area of interest e.g. a melting thermoplastic flows to take up space and solidifies to complete the healing. Typical reactions are thermally reversible reactions, thermoplastic, hydrogen bond, ionomeric coupling, molecular diffusion and chain interlocking (Blaiszik et al., 2010; Yue et al., 2014; Zhong and Post, 2015). Thermally reversible self-healing involves a reversible reaction that leads to the polymerisation of the damaged areas. Importantly, this self-healing approach is mostly non-autonomic because the reaction can only be initiated by some form of energy e.g. temperature, radiation, oxygen, electric current, change in pH, etc. (Thakur and Kessler, 2015; Urdl et al., 2017; Zhong and Post, 2015). Commonly used covalent reversible reactions are Diels-Alder (DA), retro-Diels-Alder (rDA), alkoxymine group reaction, disulphide chemistry, etc. (Blaiszik et al., 2010; Liu et al., 2013a; Urdl et al., 2017; Zhong and Post, 2015). Experiments have been performed in temperature range of $100 - 150°C$ to initiate self-healing using DA or rDA reaction of multi-furan and multi-maleimide after a damage had occurred (Blaiszik et al., 2010; Chen et al., 2002, 2003; Yuan et al., 2008). Another high temperature triggered reversible reaction is the use of alkoxymine group for self-healing; self-healing occurs at a temperature of $125 - 130°C$ (Yuan et al., 2011; Zhong and Post, 2015). The high temperature requirement may not be practical in most applications and incorporation into existing materials may be daunting. In an attempt to reduce the high energy limitation of a thermally reversible reaction, a moderately driven thermal approach using disulphide chemistry during covalent bonding to mend the damaged area was presented at $60°C$ (Canadell et al., 2011; Zhong and Post, 2015). Non-covalent thermally reversible reaction like hydrogen bonding requires even lower temper-

atures. Self-healing based on hydrogen bonding involves reassembling of broken supramolecular networks after damage at room temperature. $\pi - \pi$ stacking on the other hand reseals supramolecular network at high temperature of about $80 - 100°C$ during a self-healing process (Burattini et al., 2009; Wei et al., 2014; Zhong and Post, 2015). These reversible reactions have found application in ballistics where the heat generated from a fired bullet passing through an elastomer is used to intrinsically mend the depleted region (Frei et al., 2013). The self-healed polymer showed improved tensile and compressive strength when compared with damaged polymer. Another typical application of intrinsic self-healing based reversible reaction is hydrogel. Self-healing applications of hydrogel are vast and are still emerging in different fields. For example, coating and sealant in industrial processes as well as tissue adhesive, drug administering and cell delivery in bioengineering (Wei et al., 2014).

Thermoplastic is another method of intrinsic self-healing where a thermoplastic acting as the healing agent is initiated in a polymeric composite material by heat (Blaiszik et al., 2010). The melting thermoplastic flows to the damage area to mix with the matrix material. This intrinsic approach has shown that the healed damaged area experiences increased mechanical strength in a thermosetting composite materials (Hayes et al., 2007, 2006; Luo et al., 2009). A possible setback is the high viscosity of the selected thermoplastic resin. The viscosity of the healing agent is very crucial in achieving material stasis. Healing agent must flow as fast as possible to improve the healing rate and subsequently negate the effect of the damage rate (Yue et al., 2014). One way to overcome high viscosity is by increasing the temperature and choosing healing agents with low viscosity. However, increasing temperature comes with longer cooling and healing time.

Overall, intrinsic self-healing can be applied numerous times but has limited applications because of its high energy requirement and suitability for small damage areas (Zhong and Post, 2015). Also, a trigger which most times are

externally supplied is required to initiate healing and does not necessarily make this approach autonomous.

1.2.2 Extrinsic Self-healing

In extrinsic self-healing, capsules or vascules containing the healing agents are physically placed in materials without altering the properties of the materials. The capsules or vascules are inert to healing agents and materials (Blaiszik et al., 2010). Damage to the material leads to rupture of the capsules or vascules and the flow of healing agents to the damaged area. The healing agents take up the void and solidify to complete the self-healing process. Materials may also house catalysts to speed up the healing process. A demonstration of a capsule based self-healing is shown in Figure 1.1.

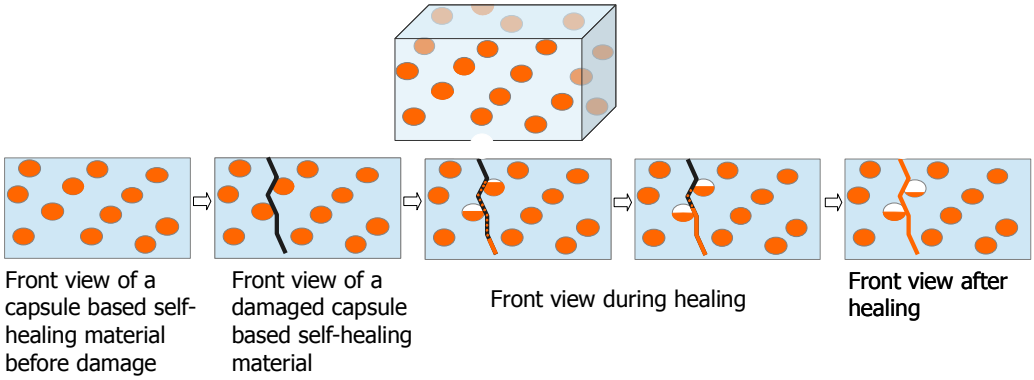

Figure 1.1: A description of a capsule based self-healing approach.

This concept has been applied to composite materials to initiate self-healing by different authors (Brown et al., 2003; Keller et al., 2007; Mergheim and Steinmann, 2013; Yeom et al., 2002; Yeom and Oh, 2000).

In one study, microcapsules of calcium lactate (healing agent) and bacteria (catalyst) were placed in a cementitious composite (Zemskov et al., 2012). The process of self-healing begins when a crack occurs in the concrete, and with the aid of water, the calcium lactate bleeds through and reacts with the bacteria to form limestone in the cracked region. This is autonomic as no external energy is required to initiate healing. In addition, investigation has shown how

different pH levels affect the triggering and release of healing capsules placed in concretes (Dong et al., 2015). The potential to reduce or prevent the collapse of buildings and bridges has inspired research in producing self-healing concretes (Huang et al., 2016; Ivanov and Stabnikov, 2017; Mignon et al., 2017a,b; Sherir et al., 2016; Wang et al., 2016).

In clinical dentistry, dental composite materials with self-healing capabilities are being investigated as an alternative to traditional dental materials (Huyang et al., 2016; Huyang and Sun, 2016; Wen et al., 2016; Wu et al., 2016a, 2015, 2016b). This retains the filling and aesthetics properties of traditional dental materials and adds capabilities to self-heal cracks and prevent bio-degradation. Microcapsules containing a mixture of strontium fluoroaluminosilicate and polyacrylic acids (Huyang and Sun, 2016) and another containing Triethylene glycol dimethacrylate-N and N-dihydroxyethyl-p-toluidine (Wu et al., 2016b) act as healing agents. While toxic concerns have been raised with some microcapsule contents (Wertzberger et al., 2010; White et al., 2001), the latter is deemed safe for dental application (Wu et al., 2016b).

The number of times healing can be initiated in capsule based self-healing is dependent on the number of capsules placed in the material. This places a limitation on applicability, particularly for materials exposed to continuous harsh conditions. Nonetheless, healing agents such as calcium lactate, dicyclopentadiene, rapeseed, fluorescent fluid, etc., have been stored in microcapsules and used to heal cracked composite materials (Jones et al., 2007; Mirabedini et al., 2015; Song et al., 2016; Zemskov et al., 2012). It is expected that more functional applications will emerge particularly with the success in embedding microcapsules in a polyelectrolyte multilayer (Zhu et al., 2016).

Alternatively, a vascular self-healing approach provides more flexibility to the design of composite material (Bleay and Loader, 2001). The architectural layout is such that a vascular network is formed by capillary tubes or hollow tubes placed within a composite material. This arrangement does not alter the mechanical properties of the material. The vascular networks are either

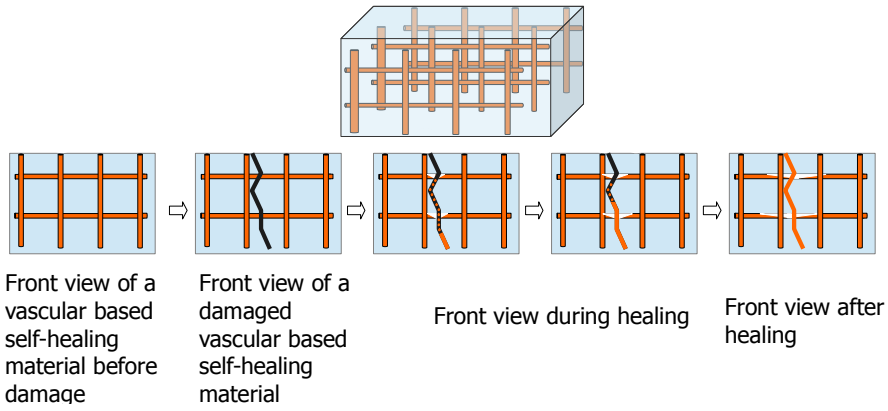

Figure 1.2: A description of a vascular based self-healing approach.

constructed in one, two or three-dimension and healing agents may be provided by external supply; increased dimensionality adds higher degree of reliability and flexibility because the damaged area enjoys multiple connectivity. An illustration of the vascular self-healing can been seen in Figure 1.2. If connected to an external source, the vascular network enjoys access to more healing agent. The healing agent is externally fed into the network and flows to the damaged area for repair. In the experiment carried out by Yue et al. (2014), a thiol-alkyne click chemistry was chosen as the healing agent because of its high product and expedient rate of reaction. The click reactant stored in a capillary tube is placed in a rubber matrix to form a composite. During fracture, the reactant bleeds to the damaged area where a reaction stimulated by UV light quickens the healing rate. After 5 minutes of exposure, an increase of up to 30% was recorded for the modulus and 100% in 10 minutes compared to the damaged composite. Other similar illustrations of vascular based self-healing have been well documented (Hamilton et al., 2010; Hansen et al., 2009; Toohey et al., 2009b).

1.3 Research Motivation and Related Work

The majority of self-healing mechanisms remain passive and reactive to damage. This means that there is no measure of capturing the incipient cause

Table 1.1: Some self-healing approaches with integrated sensing capabilities

Sensing Type	Damage Detected	Self-healing System	Material Healed
Pressure	Delamination, microcracks	Vascular	FRP(Norris et al., 2012; Trask et al., 2013)
Fibre Optics	Delamination	Vascular	CFRP (Minakuchi et al., 2014)
Pressure	Cracks, delamination, debonding	Vascular	CFRP(Trask et al., 2011)
Photo-resistor	Cracks	Intrinsic	TP (Hurley and Huston, 2011a)
Acoustic emission	Cracks	Vascular	Epoxy (Toohey et al., 2007, 2009a)
Acoustic emission	Cracks	Intrinsic	TP (Hurley and Huston, 2011b)
Fibre Optics	Cracks	Intrinsic	SMP (Garcia et al., 2010)

FRP - Fibre reinforced plastic CFRP - Carbon fibre reinforced plastic TP - Thermoplastic polymer
SMP - Shape memory polymer

of damage and healing is passively initiated only after damage. Nonetheless, some progress has been reported in integrated sensing and self-healing with the aim of improving the reliability of local detection, diagnosis and efficiency of healing. Some of the progress is shown in Table 1.1. A damage detection system was introduced into a pressurised channel of a vascular network (Trask et al., 2013). This was a controlled system that monitored the pressure drop to trigger an action. A low pressure sensor whose output was monitored through a microprocessor was connected to the pressurized vascule. Once subjected to an impact, the pressure in the pressurised vascule drops rapidly. This event triggers a 12v pump that delivers resin from an external reservoir to the damage zone. A distributed sensor has also been mounted on an optic fibre network on a composite plate (Minakuchi et al., 2014). The vascular network and an external channel supplying the healing agent are pressurised such that the vascular network has a higher pressure. The distributed sensors are mounted at different segments of the vascular network to measure the pressure and transmit the measured signals via the fibre network for assessment. In this arrangement, the distributed sensors help locate a pressure drop in any segment and initiates the release of healing agent to the area of interest.

Perhaps, a more active way of utilising the advantage of integrated sensing is to add control. Controlling the manner in which healing is triggered and the materials are healed will go a long way to improving the structural reliability of materials. To this effect, an experiment was performed to demonstrate a coordinated self-healing approach (Hurley and Huston, 2011a). An intrinsically

driven self-healing was developed by placing a high resistive alloy wire in an ethylene vinyl acetate (EVA) thermoplastic material to act as the healing agent. Unlike the other intrinsic approaches, a photo-resistive sensing gathers information as the sensor reacts with light. Magnitude of the voltage drop gathered from the sensor readings determines the extent of damage. With a given voltage threshold four standard deviation less than the mean value of a damaged free training set, analysis was carried out to determine outliers of the gathered data using Stewhart's technique. Based on the analysis, current is passed through the wire to melt the EVA and seal a crack. Once the photo-resistive sensor records a voltage at the same level as the set voltage threshold, the current stops flowing and the healing process stops. This closed loop approach introduces some form of controlled on/off regulation to activate or deactivate the heating element but does not take advantage of feedback to regulate the healing rate and can only detect the onset of abrupt faults.

An interesting approach is the potential of using electromechanical materials in self-healing systems. These are materials that can convert mechanical energy into electrical energy and vice-versa, such as piezoelectric materials. The potential of such materials is that they can be used as actuators and sensors. Polymers currently used that exhibit such characteristics are Lead Zirconate Titanate (PZT), poly vinylidene fluoride (PVDF) and dielectric elastomers (Wang and Wu, 2012; Zhong and Post, 2015). Such electromechanical materials have been combined with the principle of electrolysis to demonstrate a self-healing process (Sayayr et al., 2014; Soroushian et al., 2012). In this setup, the electrical energy generated by the electromechanical material provides the voltage needed by the electrolysis process to drive healing agent to the damaged zone. A full description of the self-healing process is detailed in Section 2.2 of Chapter 2. Like other self-healing approaches, this material faces the challenge of balancing the healing and damage rate. Self-healing is only possible when the piezo-induced potential energy is greater than the inherent over-potentials of electrolysis. Only then is the charge sufficient to drive the electrochemical

process. In practice, materials are exposed to varying stress level over time and the stress may not generate enough potential energy to drive the healing process. Also, another inherent problem is the duration of deposition of the healing agent. The duration of the piezo-induced energy must be sufficient to deposit the required healing agent during healing. Despite the obvious potentials of the electromechanical material, this design does not benefit from the advantages that embedded sensing or control systems design provides. The arrangement is an analog open loop system with a unity gain in a forward path.

1.4 Problem Definition

A range of approaches through which different materials can be self-healed from a chemical engineering perspective have been reviewed. The core of these approaches is primarily focussed on proposing and understanding the self-healing mechanism. A typical self-healing process is insensitive to the propagation of faults and healing is passively triggered when damage occurs (see Figure 1.3). These designs generally suffer from several inherent limitations that restrict their applicability in the real world and have arguably prevented technological progress past TRL 3 (Blaiszik et al., 2010; Kuponu et al., 2016). These include:

1. Healing is initiated passively and does not take into account the propagation of a fault to detect the damage at an early stage and initiate healing.

2. Self-healing is typically an open loop process with no regulation of the healing process to counteract the onset of damage. As a result, the process is unable to achieve the desired healing response over a period of time. Handling of uncertainty/disturbance is also poor.

3. The location of healing mechanisms determine the effectiveness of healing. This means that maximum healing is not guaranteed at the fault location.

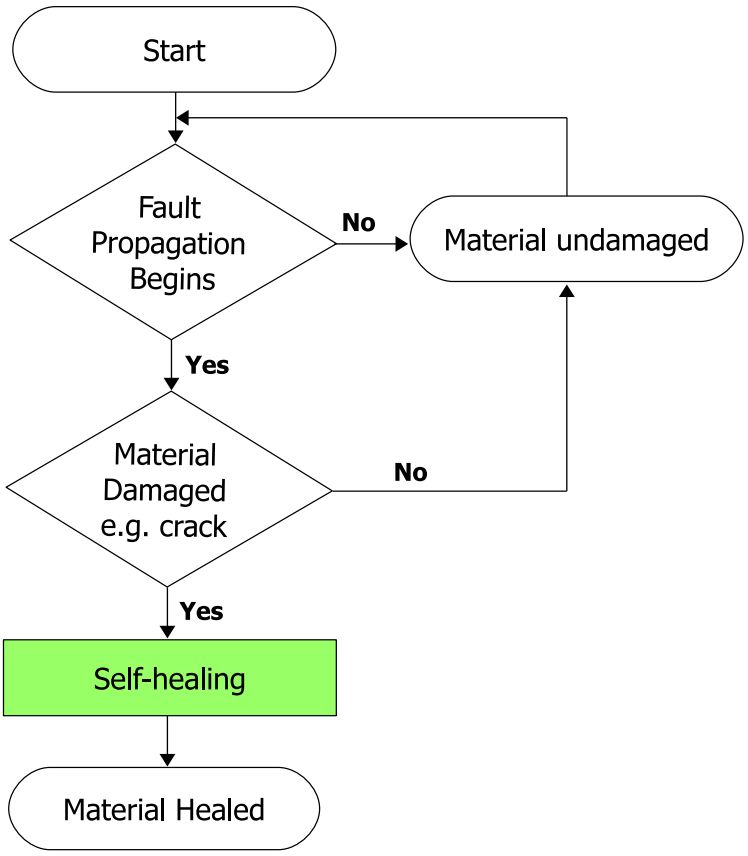

Figure 1.3: Typical self-healing process of a composite material.

4. There is no monitoring of the current healing state. For example, the healing state is unknown during the healing process and the only indication is when the healing agent has stopped flowing into the damaged zone (due to restriction in the flow healing agent).

The work presented in this thesis will address these inherent problems by focussing on the following research questions:

1. Can the rate of healing be controlled by using an active healing system?

2. Can a self-healing system be developed that can pre-empt failure and deliver healing such that the failure is prevented from onset?

The current self-healing approaches can certainly lead to further advances and target the problems outline. However, an alternative is the need to integrate sensing, actuation, computation and communication into materials (McEvoy

and Correll, 2015). This is a multidisciplinary approach to self-healing that will certainly enhance performance and help self-healing to progress to a level that is commercially useful.

The research questions will be addressed by extending an existing self-healing approach into an active healing and integrated sensing system as shown in Figure 1.4. This essentially allows the self-healing mechanism to be measured, modelled and controlled. By considering the self-healing mechanism as a system in a closed loop, the healing rate can be controlled to meet user or environmental demands, such as the damage rate. This arrangement is referred to in this thesis as active self-healing. Active control is a process through which external energy is applied to a process to achieve a desired response. Regulating the healing rate involves controlling factors that can affect the reaction kinetics of a healing process. Factors such as the speed of delivery/mass flow rate (Ye et al., 2014), release mechanism, temperature, catalyst, pressure, concentration and pH level of a self-healing system. For example, feedback control could be applied to a vascular network to control the pressure release and flow rate of healing agent from an external reservoir. The behaviour of the release and flow of healing agent in such a system has previously been modelled (Hall et al., 2015). In self-healing of a cementitious composite, the pH level has been determined to affect the release rate of healing agents enclosed in microcapsules (Dong et al., 2015) and can be controlled to give a desired response with respect to the effect of damage. The intrinsic self-healing based on piezoelectricity and electrolysis can be controlled with the aim of maintaining a sufficient chemical kinetic.

In addition, the active self-healing can benefit from additional components such as sensors for fault diagnosis. A fault diagnosis system helps to locate the damage and to define a desired response by taking advantage of sensor measurements to estimate a measure of the damage rate. Importantly, the feedback control can regulate the healing process to match the estimated measure of the damage rate. The advantages of this complete closed loop

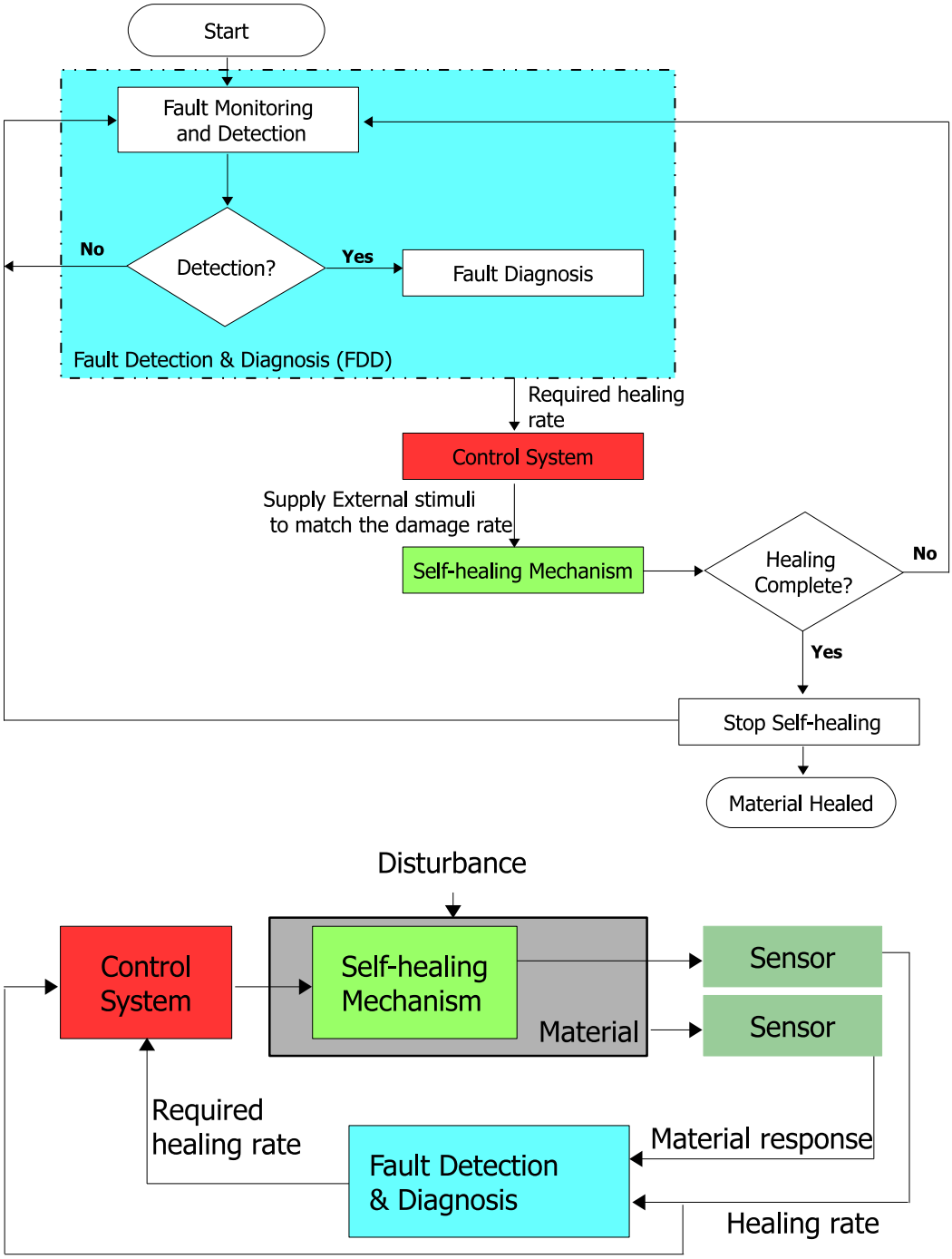

Figure 1.4: Proposed generic unified sensing, diagnosis and active self-healing System.

system are that it allows for pre-emptive healing, regulation of the healing process and a proper match between the damage and healing rate. This means that a desired response can then be achieved regardless of any disturbance or uncertainty that may affect the performance of the healing process. Active

self-healing addresses some of the shortfalls of a typical self-healing process, can guarantee a high degree of reliability and has the potential to improve the level of confidence in accepting self-healing materials for everyday use.

This research will draw on the above self-healing literature to select a self-healing mechanism. Subsequently, the self-healing mechanism will be modelled based on what is obtained in literature (Feenstra et al., 2008; Lee et al., 2014; Shen et al., 2011). The proposed active self-healing is addressed as a control problem and different control strategies such as proportional-integral (PI), adaptive inverse control and adaptive sliding mode control will be considered from literature (Recker et al., 1991; Wang et al., 2004). Analysis of a cracked beam will be detailed from literature to formulate a diagnosis technique (Dawari and Vesmawala, 2013; Loutridis et al., 2004; Vakil-Baghmisheh and Peimani, 2008). The beam represents typical engineering systems such as bridges, turbine blades,airliner wings, cranes, building elements, etc. Finally, the fault diagnosis will be integrated with the active self-healing to demonstrate the proposed unified sensing, diagnosis and active self-healing system from an application point of view. For readability of the thesis, the description and background research is developed and detailed in the appropriate chapters.

1.5 Novel Contribution

The work presented in this thesis is as follows:

- A mathematical model is developed to describe an experimented self-healing process, and shows through simulations how some of the drawbacks of passive self-healing lead to a poor match between the damage and healing rate.

- A closed loop self-healing system (referred as active self-healing) is designed and validated in simulation to regulate the healing rate to meet user or environmental demands, such as the need to match the damage rate. This work and the first contribution have been published in Journal

of Smart Materials and Structures (Kuponu et al., 2016) and presented in an International Conference of Smart and Multifunctional Materials, Structures and Systems (Kuponu et al., 2017a).

- A new fault diagnosis algorithm is developed to estimate the crack depth and location of two faulty beam types, that is, cantilever and fixed beam.

- A unified sensing, diagnosis and active self-healing system is developed and validated in simulation to effectively show that self healing can be more robust and potentially attractive to industrial applications. This work has been submitted for publication in the Journal of Intelligent Material Systems and Structures.

1.6 Publications

The work presented in this thesis has been published and submitted for publication in part in two journals and a conference paper.

- Kuponu, O.S., Kadirkamanathan, V., Bhattacharya, B. and Pope, S.A., 2016. Using feedback control to actively regulate the healing rate of a self-healing process subjected to low cycle dynamic stress. Smart Materials and Structures, 25(5), p.055028 (Kuponu et al., 2016).

  The journal paper incorporates elements from Chapter 2 and Chapter 3

- Kuponu, O.S., Kadirkamanathan, V., Bhattacharya, B. and Pope, S.A., 2017. Integrating self-healing, control and fault diagnosis. Journal of Intelligent Material Systems and Structures (Kuponu et al., 2017b). (Submitted)

  The journal paper incorporates elements from Chapter 2 to Chapter 5.

- Kuponu, O.S., Kadirkamanathan, V., Bhattacharya, B. and Pope, S.A., 2017. Integrated sensing, monitoring and healing of composite systems.

In Advances in Science and Technology (Vol. 101, pp. 62-68). Trans Tech Publications (Kuponu et al., 2017a).

This was presented at the 5th International Conference of Smart and Multifunctional Materials, Structures and Systems, CIMTEC 2016, Italy.

The Conference paper incorporates elements from Chapter 2 and Chapter 3.

1.7 Thesis overview

The remainder of this thesis is structured as follows:

In Chapter 2, a previously experimented self-healing process that is based on piezoelectricity and electrolysis will be described and a novel mathematical model will also be presented to describe the self-healing process. The model parameter will be estimated from the experimental set-up of the electrolysis of copper (II) sulphate. It will also be shown through simulations how the identified drawbacks in Chapter 1 limits the performance of a self-healing process.

In Chapter 3, a novel active self-healing system will be presented. The arrangement takes advantage of sensing and feedback control to regulate the healing rate to meet user or environmental demands, such as the need to match the damage rate. This will include mathematical formulations of adaptive sliding mode controller for two self-healing systems. Simulation results showing the effectiveness of the closed loop self-healing system to matching the damage rates will be demonstrated. More so, the effect of uncertainties and disturbances will be investigated to show the effectiveness of the novel active self-healing system. A comparison with the equivalent passive self-healing process will be shown.

In Chapter 4, a novel crack detection and diagnosis that can be applied to differ-

ent types of beams will be formulated. It will then be shown through simulations the effectiveness of the proposed diagnosis. Importantly, a sensitivity analysis will be investigated to show the effect of uncertainties on the proposed technique.

In Chapter 5, a novel unified sensing, diagnosis and active self-healing system framework will be presented. It will also be shown that faults can be predicted and healing can be monitored and maximized at the needed location. Simulation results will be provided to show the effectiveness of the proposed framework to regulating the healing process and matching the damage rate. A comparison with an equivalent passive self-healing process will be demonstrated.

Finally, Chapter 6 will present concluding remarks on the work in this thesis. Recommendations on future research directions will also be presented.

Chapter 2

Self-healing Model

2.1 Introduction

Most of the available self-healing works are experimental and lack mathematical models. As such, this chapter presents a novel mathematical model describing a self-healing mechanism. A mathematical model generally allows the underlying dynamics of a system to be understood and creates a platform to improve on existing applications. Based on the review from Chapter 1, the mathematical model represents a composite material whose self-healing mechanism is based on piezoelectricity and electrolysis; that is, a solid state electrolysis driven by stress induced current from piezoelectric element. This is selected because electromechanical polymers can inherently be used for sensing and actuating; also the scarcity of literature in electromechanical polymers for self-healing indicates an emerging technology (Zhong and Post, 2015).

A key attribute of the developed mathematical model in this chapter, as well as throughout the research, is to show some of the drawbacks of a typical self-healing material. The majority of self-healing materials are passive, unregulated and may not effectively counteract the onset of damage. Disturbances and uncertainties are also not accounted for during self-healing. This generally affects the performance of self-healing and the match between the damage and healing rate may not be guaranteed.

The aims of this chapter are:

- Develop a mathematical model representing a self-healing mechanism based of piezoelectricity and electrolysis.
- Highlight the drawbacks of a typical passive self-healing process using the modelled healing mechanism.
- Present simulation examples of a composite self-healing material whose healing mechanism is piezoelectricity and electrolysis.

In the following (Kuponu et al., 2016, 2017a,b), a theoretical framework of the self-healing mechanism is presented in Section 2.2. In Subsection 2.2.1, a mathematical model for a piezoelectric system and simulation example are presented. Subsection 2.2.2 introduces a mathematical model of the electrolysis process and highlights the inherent dead-zone non-linearity that can limit the performance of the healing process. A linear approximation of the piezo-electrolytic self-healing model is presented in Section 2.3. This is followed by an electrolysis experiment to estimate the model parameters in Section 2.4. Example simulations and a discussion of the self-healing mechanism are presented in Section 2.5. A summary is given in Section 2.6.

2.2 Self-healing Mechanism Model

Experiments have previously been carried out to show the potential of using an electromechanical material for self-healing (Sayayr et al., 2014; Soroushian et al., 2012). In an effort to benefit from the sensing and actuation capabilities of electromechanical materials, Sayayr et al. (2014) combined alternative layers of carbon fibre reinforcement and poly vinylidene fluoride-co-hexafluropropylene (PVDF-HFP) solid electrolyte to form composite laminates. The laminates were held together by bolts, which act as electrodes. The PVDF-HFP solid electrolyte material was prepared from a mixture of PVDF-HFP, zinc oxide and copper nanoparticles. Investigations were conducted to assess the ability of the

newly formed composite material to self-heal. The principle behind the healing process is depicted in Figure 2.1 and Figure 2.2. A sustained stress applied

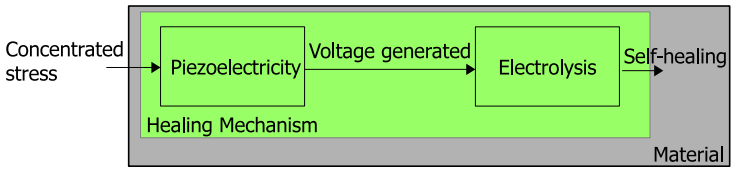

Figure 2.1: Open-loop representation of the healing mechanism of a self-healing material. The electrolytic process is driven by the voltage generated from the direct piezoelectric effect of the electromechanical material.

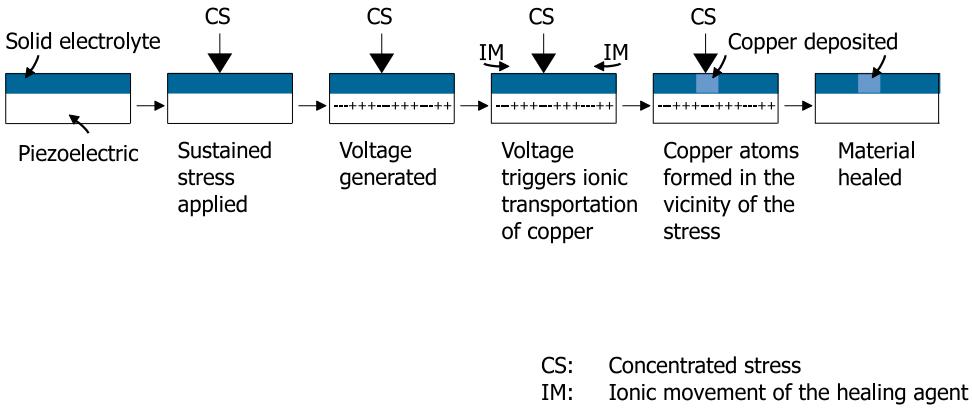

Figure 2.2: A diagram of the self-healing steps

on the electrode resulted in the deposition of copper nanoparticles around the electrodes. This is due to the direct piezoelectric effect phenomenon of the electromechanical material that converts mechanical energy into electrical energy. Voltage measurements around the vicinity of the electrode where the stress was applied validated the direct piezoelectric effect. The generated voltage is used to actuate the electrolysis process that deposits copper nanoparticles. The findings effectively demonstrate a self-healing process, with the deposited copper nanoparticles as the healing agent. Also confirmed was a negligible deposition of zinc in neighbouring areas. A similar experiment by Soroushian et al. (2012) demonstrated a self-healing process based on piezoelectricity and electrolysis. The stressed area of the carbon fibre PVDF-HFP solid electrolyte material effectively became the cathode and mass deposition of copper nanoparticles

was evident within the area. Like Sayayr et al., a mechanical test measuring the hardness of the material was carried out near and away from the deposition area. The result showed increased material strength in the area where copper nanoparticles was deposited. The self-healing process is however limited by the dependency on the sustained stress and piezo-induced voltage. Hence, mass deposition is only possible when the piezo-induced voltage is greater than the inherent over-potentials of electrolysis.

As this open loop self-healing process is directly driven by a voltage, it is particularly suitable to be developed into an active self-healing process that is regulated by some form of digital feedback control and additional actuation is not needed like the vascular system that is connected to an external pump. To begin, the principle of operation behind the self-healing process is modelled by two subsystems. The piezoelectric subsystem models the electromechanical property of the material in Subsection 2.2.1, and the deposition of healing agent is modelled through the electrolysis subsystem in Subsection 2.2.2.

2.2.1 Electromechanical Model of the Piezoelectric Subsystem

Piezoelectric materials can be used in two ways. The direct piezoelectric effect converts mechanical energy into electrical energy while the converse effect is the reverse of this. In this research, the direct piezoelectric effect is used. Figure 2.3 shows a piezoelectric stack consisting of z layers of piezoelectric patch material connected in parallel. The stack is used to enhance charge generation when compared to a bulk piezoelectric. The constitutive relations in the transverse direction of a piezoelectric stack are shown in Equations (2.1) - (2.2). These couple the mechanical and electrical response of a stacked piezoelectric material (Corr and Clark, 2002; Feenstra et al., 2008; Hou et al., 2012; Lee et al., 2014; Liu and O'Connor, 2014; Satkoski, 2011).

$$D_3(t) = d_{33}T_3(t) + \epsilon_{33}^T E_3(t) \tag{2.1}$$

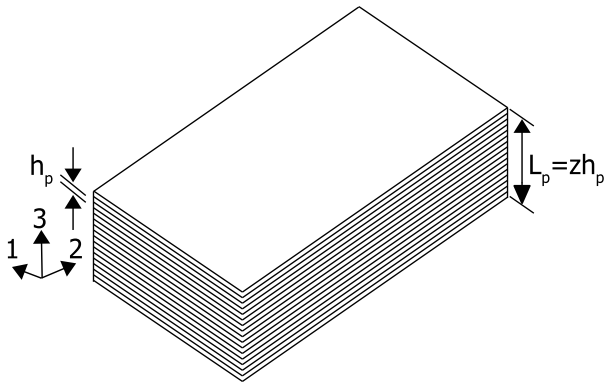

Figure 2.3: Stacked piezoelectric material consisting of z layers of piezoelectric patch.

$$S_3(t) = s_{33}^E T_3(t) + d_{33} E_3(t) \tag{2.2}$$

Mechanical energy applied to a piezoelectric material induces an electric field E_3 in the material. The direct piezoelectric effect defined in Equation (2.1) describes the resulting electrical characteristics and their relation to an applied mechanical stress. Similarly, Equation (2.2) is the piezoelectric converse effect which defines the mechanical characteristics and their relation to an applied electric field. S_3 and D_3 are the strain and electric displacement respectively, s_{33}^E and ϵ_{33}^T are the compliance constant and dielectric permittivity respectively, d_{33} represents the piezoelectric coupling coefficient, T_3 is the stress. The relationships between the voltage V_p across each piezoelectric layer, the total charge Q_p generated from electric displacement and other parameters are given in Equation (2.3) (Feenstra et al., 2008).

$$V_p = h_p E_3; \quad Q_p = z D_3 A_p; \quad S_3(t) = \frac{x(t)}{L_p}; \quad s_{33}^E = \frac{1}{E_p}; \quad T_3(t) = \frac{f}{A_p} \tag{2.3}$$

where f is the stack actuator force, E_p defines the Young's modulus, A_p is the cross-sectional area of the piezoelectric material, $x(t)$ represents the relative stack displacement, z is the number of piezoelectric layers, h_p is the thickness of a piezoelectric patch and L_p is the total height of the stack given as $L_p = z h_p$. Substituting Equation (2.3) into Equations (2.1) - (2.2) results

in Equations (2.4) - (2.5):

$$Q_p(t) = d_{33} z f_s(t) + \frac{z \epsilon_{33}^T A_p}{h_p} V_p(t) \tag{2.4}$$

$$x(t) = \frac{L_p}{E_p A_p} f(t) + d_{33} z V_p(t) \tag{2.5}$$

The total capacitance, stiffness and applied force of the piezoelectric stack are given as $C_p = \frac{z \epsilon_{33}^T A_p}{h_p}$, $k_p = \frac{E_p A_p}{L_p}$ and $f(t)$ respectively (Feenstra et al., 2008). Equations (2.4) - (2.5) are rewritten to emphasize the direct relationship between the applied force and charge by reversing their polarities in Equations (2.6) - (2.7).

$$-Q_p(t) = d_{33} z k_p x(t) + C_p V_p(t) \tag{2.6}$$

$$x(t) = -\frac{1}{k_p} f(t) + d_{33} z V_p(t) \tag{2.7}$$

On differentiation and substitution for $\dot{Q}_p(t) = \frac{V_p}{R_p}$ (where R_p is the total resistance of the stack), Equation (2.6) becomes Equation (2.8).

$$\dot{V}_p(t) = -\frac{1}{R_p C_p} V_p(t) - \frac{d_{33} z k_p}{C_p} \dot{x}(t) \tag{2.8}$$

Equation (2.7) represents the mechanical model coupled with electrical signal for a massless system. Taking into account the mass of the piezoelectric stack M_p which is not negligible, the sum of the forces acting on the piezoelectric stack is equal to the inertial force due to the mass. This assumes a simple lumped mass single degree of freedom (SDOF) model and Equation (2.7) becomes Equation (2.9), which leads to Equation (2.10) for the acceleration.

$$M_p \ddot{x}(t) = -k_p x(t) + d_{33} z k_p V_p(t) - f(t) \tag{2.9}$$

$$\ddot{x}(t) = -\frac{1}{M_p} \left(k_p x(t) - d_{33} z k_p V_p(t) + f(t) \right) \tag{2.10}$$

Equations (2.11) - (2.12) give the state-space representation of Equation (2.8) and Equation (2.10).

$$\begin{bmatrix} \ddot{x} \\ \dot{x} \\ \dot{V}_p \end{bmatrix} = \begin{bmatrix} 0 & -\frac{k_p}{M_p} & \frac{d_{33} z k_p}{M_p} \\ 1 & 0 & 0 \\ -\frac{d_{33} z k_p}{C_p} & 0 & -\frac{1}{R_p C_p} \end{bmatrix} \begin{bmatrix} \dot{x} \\ x \\ V_p \end{bmatrix} + \begin{bmatrix} -\frac{1}{M_p} \\ 0 \\ 0 \end{bmatrix} f(t) \tag{2.11}$$

$$y = \begin{bmatrix} 0 & 0 & 1 \end{bmatrix} \begin{bmatrix} \dot{x} \\ x \\ V_p \end{bmatrix} \tag{2.12}$$

Figure 2.4 shows the frequency response between force and voltage of a typical piezoelectric stack whose parameters are found in Table 2.1 (Feenstra et al., 2008). The frequency response curves give a measure of the input to output

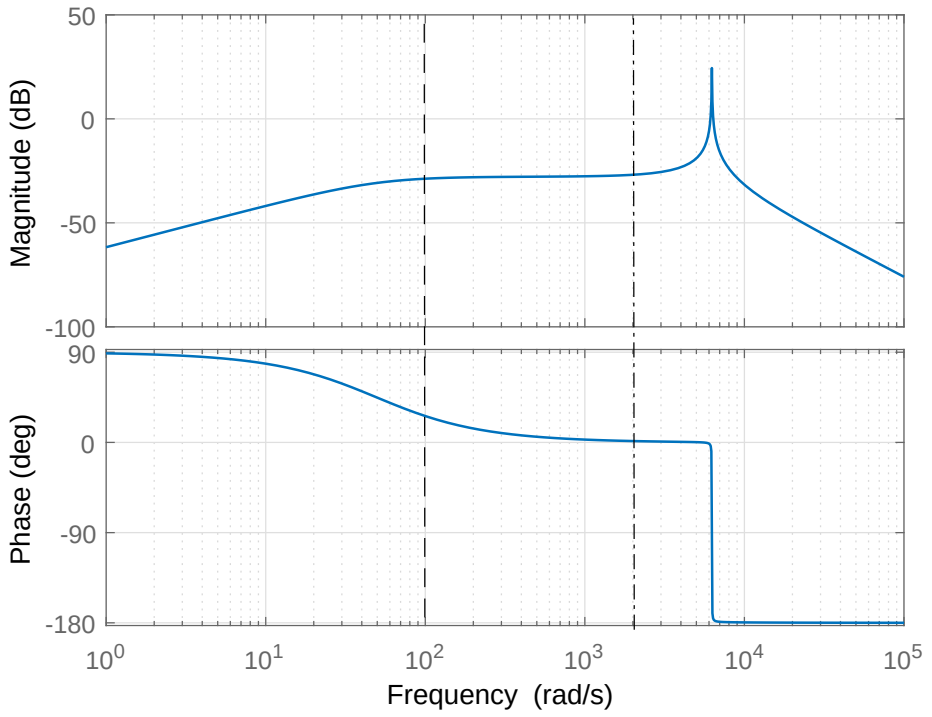

Figure 2.4: Frequency response between the applied force and the generated voltage.

relationship. This informs the operating frequency of any system application.

Table 2.1: Mechanical properties of a piezoelectric stack (Feenstra et al., 2008).

Parameters	Values
Cross sectional area A_p	25 mm^2
Number of layers z	130
Length L_p	16 mm
Mass M_p	2.3 g
Coupling coefficient d_{33}	650 pC/N
Dielectric permittivity ϵ_{33}^T	6200 pF/m
Capacitance C_p	1.59 μF
Resistance R_p	9.72 $K\Omega$
Young's Modulus E_p	44 GPa

For example, the flat regions of the spectrum are usually suitable for systems that require little or no change in magnitude over a frequency range. In this case, piezoelectric stack will be operating in a flat frequency range of $100 - 2000$ rad/sec, with a gain of 38.2 mV/N. This means that a sinusoidal load of amplitude 0.2 N applied to the piezoelectric stack at a frequency of 138 rad/sec would generate an output of amplitude 7.64 mV.

2.2.2 Model of Electrolysis Subsystem

A setup for electrolysis in Figure 2.5 requires electricity, electrodes (anode and cathode) and electrolyte. The electrolytic process is triggered by applying a direct current (DC) voltage to the circuit. This causes ionic movements of positive ions toward the negative electrode (cathode) and the negative ions toward the positive electrode (anode), to form atoms. Ionic movement is achieved when the voltage applied is at least equal to the barriers which are, the sum of the reversible potential E_{rev}, over-potential at cathode η_c and anode η_a and ohmic resistance η_{ohmic}. This is expressed in Equations (2.13) - (2.17) (García-Valverde et al., 2012; Manage and Sorensen, 2014; Shen et al., 2011):

$$V_{min} = E_{rev} + \eta_a + \eta_c + \eta_{ohmic} \tag{2.13}$$

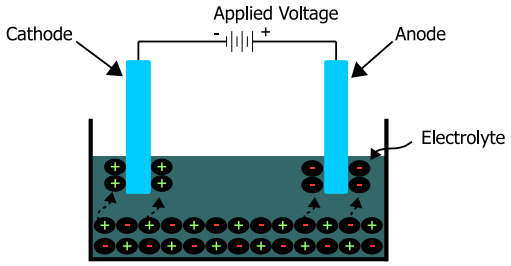

Figure 2.5: Movement of positive ions (green crosses) and negative ions (red dashes) towards the negative electrode (cathode) and positive electrode (anode) respectively, during an electrolytic process.

$$\eta_a = \frac{RT}{F} \ln\left(\frac{j}{j_{(j,a)}}\right) \tag{2.14}$$

$$\eta_c = \frac{RT}{F} \ln\left(\frac{j}{j_{(o,c)}}\right) \tag{2.15}$$

$$\eta_{ohmic} = iR_{ohmic} \tag{2.16}$$

$$R_{ohmic} = \frac{t_m}{\sigma_m} \tag{2.17}$$

with R representing the gas constant and T representing the absolute temperature. The term i is the current flow, j is the current density while F is the Faraday constant; $j_{(o,a)}$ and $j_{(o,c)}$ are the exchange current density at the electrodes respectively. R_{ohmic}, t_m, σ_m are the membrane resistance, thickness and conductivity respectively. The rate of deposition of ions at both electrodes during electrolysis can be expressed as Equation (2.18) (García-Valverde et al., 2012; Manage and Sorensen, 2014; Shen et al., 2011):

$$\dot{\eta}_{rate} = \frac{n_{cell} i}{n_e F} \eta_f \tag{2.18}$$

where n_{cell} and n_e are the number of cells and number of electron consumed at the electrodes to produce a mole of atom respectively. η_f is the Faraday efficiency assumed to be greater than 99% for a polymer electrolyte membrane (PEM) (García-Valverde et al., 2012; Ghribi et al., 2013).

In this model, emphasis is on the current flowing through an electrolytic process. This current is proportional to the deposition rate (Equation (2.18)) and can easily be measured during experiment. Applied voltage causes current to flow through the circuit in Figure 2.5, and also results in ionic transportation towards the electrodes. The relationship between the applied voltage and current flowing during electrolysis that was modelled by Shen et al. (2011) is adopted in this research. This has been selected because of its simplicity in understanding the voltage-current relationship and to capture the dead-zone non-linearity associated with electrolysis. If the ohmic resistance η_{ohmic}, over-potential at cathode η_c and anode η_a are coupled together to form ir, then Equation (2.13) is rewritten as Equation (2.19).

$$V_{min} = E_{rev} + ir \tag{2.19}$$

Given the applied voltage V, the power used during electrolysis becomes Equation (2.20) (Shen et al., 2011).

$$P \propto (V - E_{rev} - ir)^2 \tag{2.20}$$

$$P = K(V - E_{rev} - ir)^2 \tag{2.21}$$

Considering the power loss i^2r due to the internal resistance of the material, Equation (2.21) becomes Equation (2.22) (Shen et al., 2011).

$$iV - i^2r = K(V - E_{rev} - ir)^2 \tag{2.22}$$

$$i = \frac{V + 2Kr(V - E_{rev}) - \sqrt{V^2 + 4KrE_{rev}(V - E_{rev})}}{2r(1 + Kr)} \tag{2.23}$$

Equation (2.23) gives a mathematical representation of the relationship between the voltage applied and the actual current flowing during electrolysis. The red line in Figure 2.6 illustrates the voltage-current relationship for a small cell when $E_{rev} = 0.6\ V$, $K = 1.83\ \Omega^{-1}$ and $r = 0.95\ \Omega$ (Shen et al., 2004). A

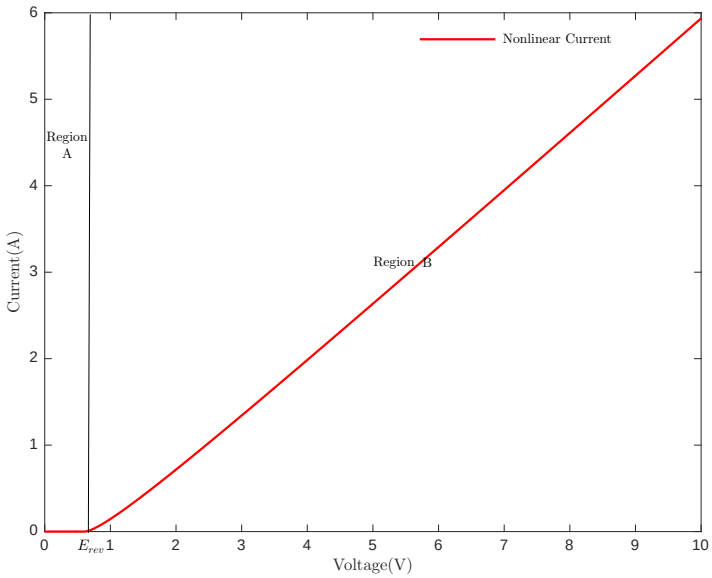

Figure 2.6: Relationship between applied voltage and current flowing through the electrolysis process. This mimics a dead-zone non-linearity behaviour when $V(t) \leq E_{rev}$.

voltage range of 0 to 10v is applied to drive the electrolytic circuit and it can be seen that current begins to flow only after 0.6 V. The voltage must be sufficient to generate enough current flow to initiate ionic transportation. This means that the electrolysis process is insensitive at voltages less than or equal to E_{rev}. As a result, the circuit's behaviour is that of a dead-zone non-linearity when the voltage applied is less than or equal to E_{rev}. Based on this behaviour, the process can operate at any time within the two regions defined in Figure 2.6, namely: region A: dead-zone region ($V(t) \leq E_{rev}$) and region B: current flow region ($V(t) > E_{rev}$).

2.3 First Order Linear Approximation and Model Parameter Estimation Using Least Squares Method

Using a first order linear approximation about two operating points, the current (Equation (2.23)) flowing through the electrolysis process becomes a piecewise function written as:

$$\hat{i}(t) = \begin{cases} mV(t) - m\hat{E}_{rev} & \text{for } V(t) > \hat{E}_{rev} \\ 0 & \text{for } V(t) \leq \hat{E}_{rev} \end{cases} \tag{2.24}$$

where $\hat{i}$ is the estimate of current i, m is a positive slope and $\hat{E}_{rev}$ is the estimate of E_{rev}. Figure 2.7a shows the comparison between the first order linear approximation (in blue line) and the actual model (in red line) of the relationship between the voltage applied and the current flow during electrolysis. The residuals (see blue line of Figure 2.7b) and the mean absolute error (MAE) of 0.12 indicate that the model in Equation (2.24) is a good approximation of the model in Equation (2.23) within the considered voltage range in Figure 2.7. The approximate model also mimics the dead-zone non-linearity behaviour of the actual model.

Experimental data can be fitted to the piecewise linear model by estimating the unknown parameters m and $\hat{E}_{rev}$ using the least square method. For N measurements and unknown coefficients n_o, Equation (2.24) can be rewritten in a matrix form as Equation (2.25):

$$\hat{i}(t) = \begin{bmatrix} V(t) & 1 \end{bmatrix} \begin{bmatrix} m \\ -m\hat{E}_{rev} \end{bmatrix} \tag{2.25}$$

$$I_o = \chi\vartheta \tag{2.26}$$

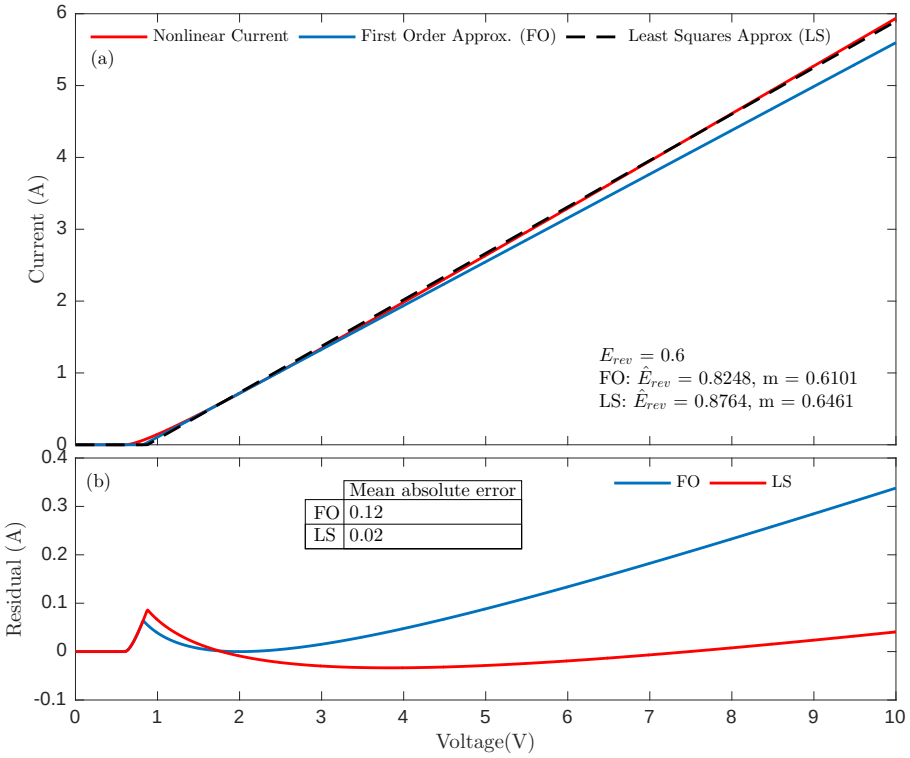

Figure 2.7: Approximate model of the non-linear relationship between applied voltage and current flowing through the electrolysis process. The approximate model also mimics the dead-zone non-linearity behaviour of the actual model.

where I_o contains N number of current samples generated from a monotonically increasing voltage (i.e. I_o has a dimension of $N \times 1$), χ is $N \times n_o$ and ϑ is $n_o \times 1$. The least squares is obtained by minimising the sum of the square of the model error ξ in Equation (2.27). As a result, the unknown parameters are estimated as Equation (2.28).

$$\begin{aligned} \xi =& \frac{1}{N}\Big(I_o - \chi\vartheta\Big)^T\Big(I_o - \chi\vartheta\Big) \\ =& \frac{1}{N}\Big(I_o^T I_o - I_o^T\chi\vartheta - \vartheta^T\chi^T I_o + \vartheta^T\chi^T\chi\vartheta\Big) \end{aligned} \tag{2.27}$$

$$\vartheta = (\chi^T\chi)^{-1}(\chi^T I_o) \tag{2.28}$$

Figure 2.7a also shows the relationship between the voltage applied and the current flow during electrolysis using the parameters estimated from the least

square method. The residuals (see red line of Figure 2.7b) and the mean absolute error (MAE) of 0.02 also confirm that model in Equation (2.24) is a good estimator of the model in Equation (2.23). Equation (2.24) can be expressed in the manner of Equation (2.29).

$$\hat{i}(t) = mV(t) + \Delta I(t) \tag{2.29}$$

$$\Delta I(t) = \begin{cases} -m\hat{E}_{rev} & \text{for } V(t) > \hat{E}_{rev} \\ -mV(t) & \text{for } V(t) \leq \hat{E}_{rev} \end{cases} \tag{2.30}$$

In self-healing mode, the piezo-induced voltage V_p generated causes ionic transportation of copper nanoparticles to the crack area. More so, this particular self-healing process suffers additional inherent problem. Ionic transportation only occurs when the generated piezo-induced voltage is sufficient to overcome inherent barriers in electrolysis. While the system is operating in the dead-zone region ($V_p(t) \leq \hat{E}_{rev}$), the self-healing process experiences a definite mismatch between the damage and healing rate. In practice, composite materials are subjected to varying stress levels and are often harmonic signals. Therefore, they may not generate sufficient voltage to consistently initiate the self-healing process. Insufficient piezo-induced voltage implies that the process becomes insensitive to the input and generates no current. This inevitably affects the self-healing performance. Since $\hat{i}(t) = \dot{Q}_a(t)$, the system is formulated in terms of $\dot{Q}_a(t)$ for the purpose of designing the controller in the next chapter. Also, the piezo-induced voltage is represented as V_p. Hence, Equation (2.29) is rewritten as Equation (2.31).

$$\dot{Q}_a(t) = mV_p(t) + \Delta I(t) \tag{2.31}$$

The piezo-induced voltage V_p generated by the applied force is periodic and does not effectively drive the electrolysis process because the process is more effective when driven by DC voltage. Therefore, it is essential to model the direct voltage requirement of the electrolysis process. A secondary circuit that

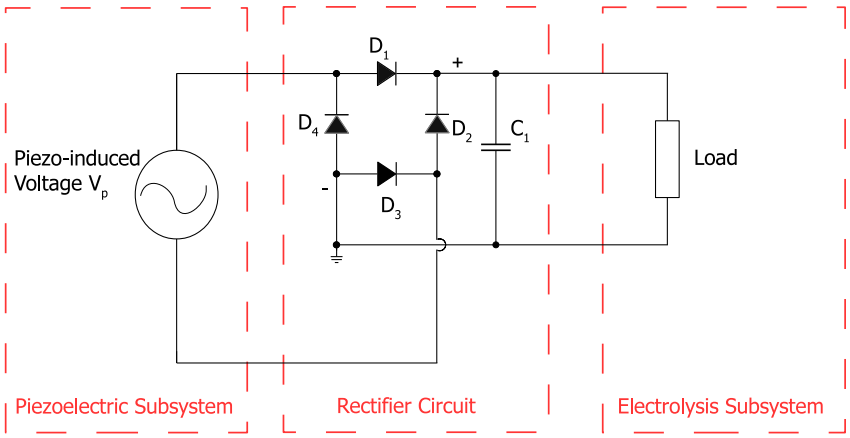

Figure 2.8: Equivalent circuit diagram of the healing mechanism of a self-healing material. This consist of the source representing the generated voltage from the applied force, rectifier circuit that converts the alternating current (AC) voltage to direct current (DC) voltage and the electrolysis process represented as load.

converts the periodic alternative current (AC) signal to a DC signal is added to the self-healing process and referred to as the rectifier circuit. In practice, this addition would not be possible since the piezoelectric and electrolyte are mixed in the polymer. However, the rectifier circuit has been included for completeness of the electrolysis demands. The equivalent circuit diagram of the self-healing mechanism for the chosen self-healing material is given in Figure 2.8. Figure 2.9 shows the effect of the rectifier circuit. The AC signal is converted into a pulsating DC signal (see blue line of Figure 2.9), that could potentially damage the load. A capacitor C_1 is added to smoothen the rectified pulsating signal, the output is the black line of Figure 2.9. Equation (2.31) is re-expressed as Equation (2.32) to account for the rectified piezo-induced voltage V_{p^r}.

$$\dot{Q}_a(t) = mV_{p^r} + \Delta I(t) \tag{2.32}$$

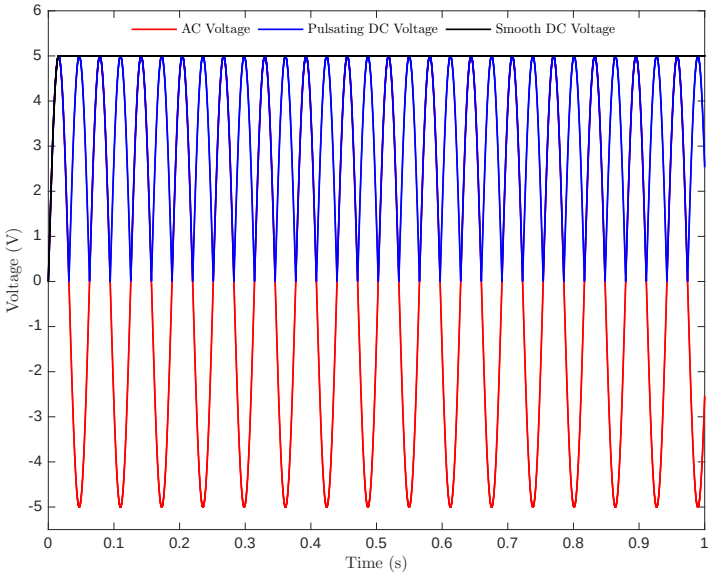

Figure 2.9: Conversion of AC voltage to DC voltage. The generated DC voltage shown as blue line is pulsating and could potentially damage the load. A capacitor is added to smoothing the pulsating DC voltage. This is shown as the black line.

2.4 Experimental Setup

The objective of the electrolysis experiment is to acquire data and use the data to estimate the model parameters of Equation (2.32) using the least squares method. The components used in the acquisition of data are as follows:

1. Personal computer
2. National Instrument data acquisition (NI-DAQ)
3. Power supply and voltage regulator
4. Current transducer
5. Amplifier
6. Electrolyser

Figure 2.10 shows the set-up of the components. A computer based Lab-VIEW application interacts with the NI-DAQ and facilitates the acquisition of data from the electrolysis process. The NI-DAQ consists of NI-9201 DAQ analog input voltage ($\pm 10\ V$) module and NI-9263 DAQ analog output voltage

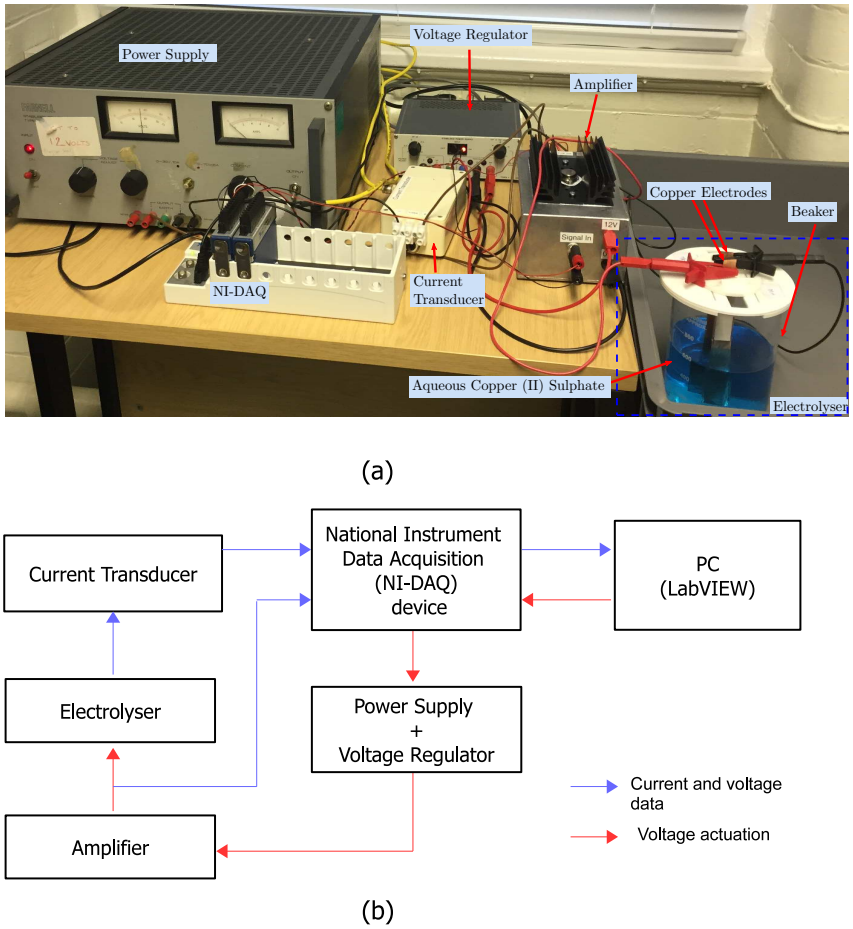

Figure 2.10: Data acquisition set-up for an electrolytic process. (a) The experimental set-up (b) A block diagram of the experimental process and data acquisition.

($\pm 10\ V$) module. A voltage command from the LabVIEW is sent through the NI-9201 DAQ to initiate a regulated DC power supply to the electrolyser. Since the NI-9201 DAQ analog input voltage is $\pm 10\ V$, an amplifier of gain equals 2 is used to increase voltage levels. The NI-9263 DAQ is used to acquire the current readings measured by the transducer during the electrolysis process. The electrolyser consists of a beaker, two copper electrodes of dimensions 15 mm by 165 mm placed 47 mm apart and a 600 ml solution containing 25 g of copper (II) sulphate. This solution has been chosen because the healing agent of interest is copper nanoparticles (same as the one used in the experiment by Sayayr et al. (2014) and Soroushian et al. (2012)). In this arrangement, the actuation command from the labVIEW was scaled down by a factor of 2

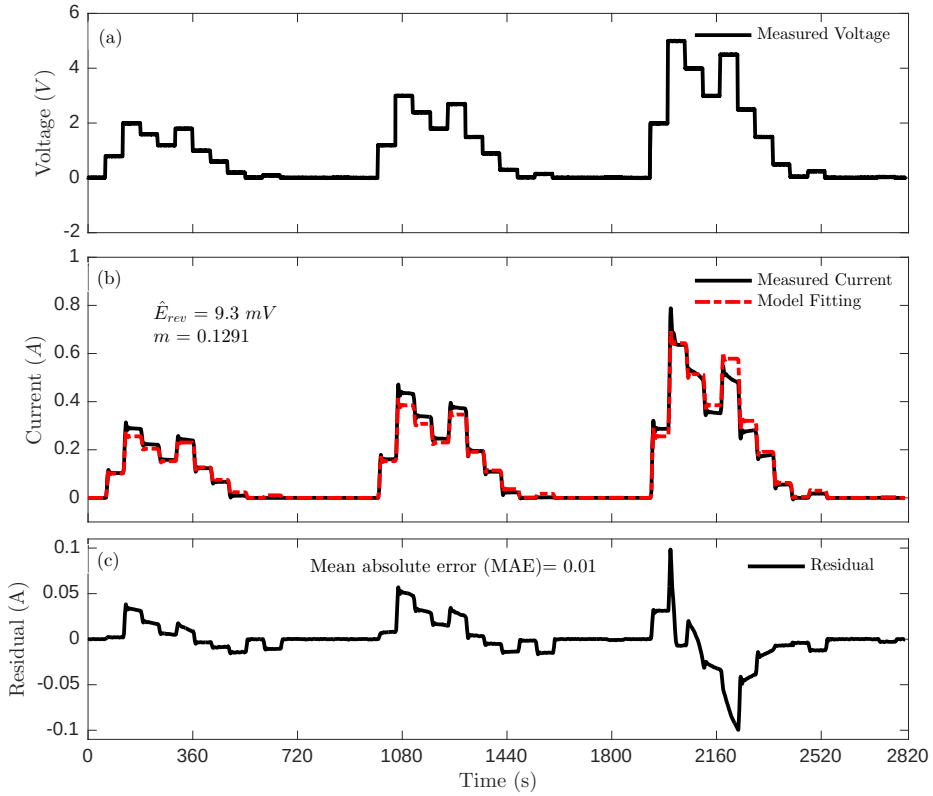

Figure 2.11: Model fitting of the acquired experimental data. (a) The voltage used to drive the electrolysis of aqueous copper (II) sulphate. (b) The current flowing during electrolysis and the model fitting using least squares method (c) The residual between the experimental data and the theoretical model

such that voltage flowing through the electrolysis is as desired (i.e. the voltage is doubled due to the amplification). Experimental data were acquired for about 47 minutes as shown in Figure 2.11. The measured actuation voltage in Figure 2.11a results in a current flow shown as black line in Figure 2.11b. The outcome of the data fitting using least squares to estimate the unknown parameters of Equation (2.32) is shown in red dashed line of Figure 2.11b. The unknown parameters were estimated as $\hat{E}_{rev} = 0.1291\ mV$ and $m = 0.1291$. The performance of the model fitting can be evaluated using the residual (see Figure 2.11c) between the experimental data and the theoretical model and the mean absolute error of 0.01. These values indicate that the physical model can be approximated by the theoretical model (Equation (2.32)).

2.5 Open Loop Example Simulations

The example simulations demonstrate a composite material with the modelled healing mechanism and copper nanoparticles as the healing agent. This is the same healing agent used by Soroushian et al. (2012) and Sayayr et al. (2014) during their experiments. The model parameters $m = 0.1291$ and $\hat{E}_{rev} = 9.3\ mV$ used in these simulations were estimated from the experiment carried out in Section 2.4.

Consider a composite material subjected to a concentrated stress level equivalent to 0.2 N at a frequency of 138 rad/sec. This is simulated as a sinusoidal input force to illustrate materials subjected to constant conditions. A piezo-induced voltage of 7.34 mV is generated by the direct piezoelectric effect and rectified to give smooth DC piezo-induced voltage V_{pr} shown in Figure 2.12a. However, the 7.64 mV generated by the applied 0.2 N is not sufficient to cause

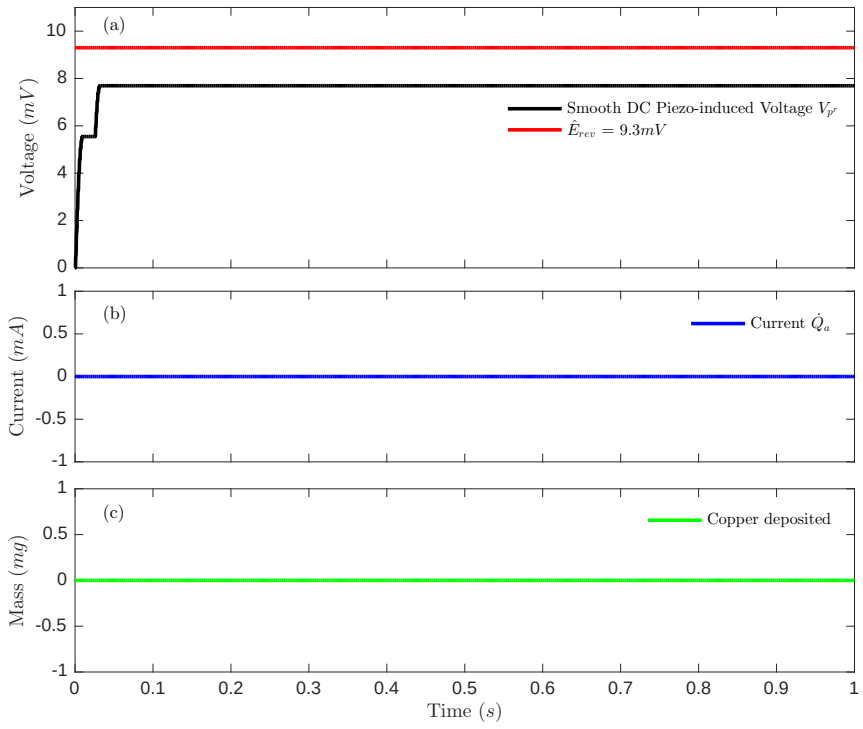

Figure 2.12: The applied 0.2 N **force generates a voltage less than** $\hat{E}_{rev}$**.** Insufficient piezo-induced voltage implies that the process becomes insensitive to the input and generates no current. The self-healing system operates in the dead-zone region and no healing is achieved.

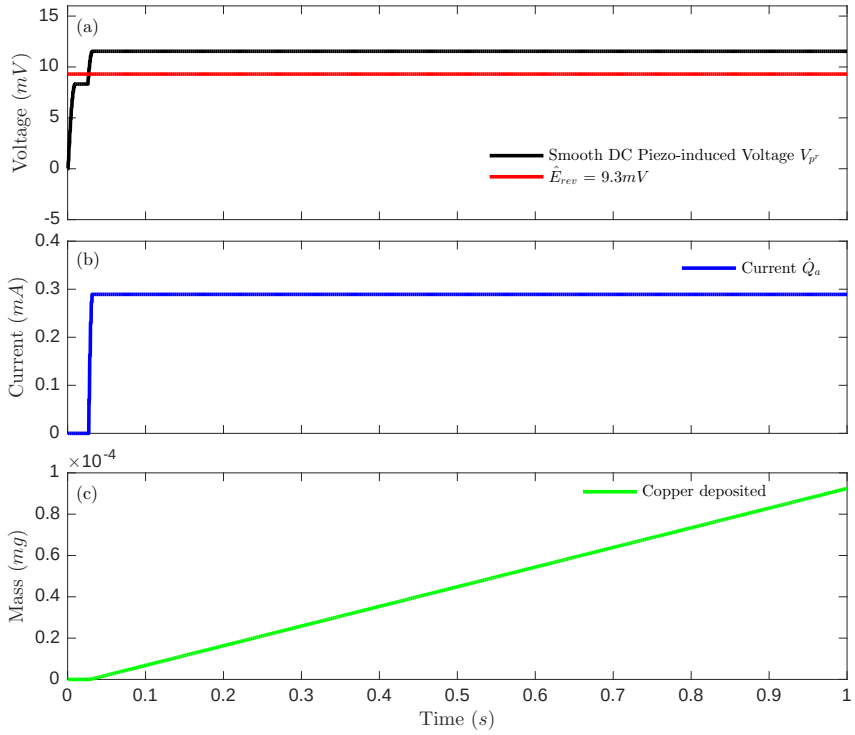

Figure 2.13: The applied 0.3 N **force generates a voltage greater than** $\hat{E}_{rev}$**.** The self-healing process now operates in the current flow region. As a result, ionic movement is triggered by the current flow leading to a mass deposition of copper nanoparticles. The process demonstrates a composite material exposed to constant environmental condition.

a self-healing process. The smooth DC piezo-induced voltage $V_{pr} = 7.34\ mV$ shown as black line in Figure 2.12a is less than the estimated reversible potential $\hat{E}_{rev} = 9.3\ mV$ shown in red line of Figure 2.12a. Insufficient piezo-induced voltage implies that the process becomes insensitive to the input and generates no current(Figure 2.12b) to establish the chemical kinetic needed to deposit the healing agent (Figure 2.12c). The process operates in the dead-zone region and inevitably affects the self-healing performance. This highlights the inherent dead-zone drawback of the healing mechanism. A piezo-induced voltage of 11.46 mV is generated when a concentrated stress level equivalent to 0.3 N is applied. This voltage is sufficient to trigger the self-healing process since $V_{pr} > \hat{E}_{rev}$ (see Figure 2.13a). The self-healing process now operates in the current flow region. As a result, ionic movement is triggered by the current flow shown in Figure 2.13b and this leads to the deposition of copper nanoparticles

(see Figure 2.13c). The result suggests that the stress level applied must be sufficient to initiate the self-healing process. An alternative arrangement is the amplification of the piezo-induced voltage to drive the electrolysis process. The piezoelectric and electrolytic components of the self-healing material are considered as separate elements, while the addition of amplification leads the system to operate more in an open-loop as opposed to a passive self-healing mode. For example, the piezo-induced voltage generated by a concentrated stress level equivalent to 0.2 N is amplified by a gain of 1.5 to generate the same effect as that of a concentrated stress level equivalent to 0.3 N. The same ionic transportation is achieved as shown in Figure 2.14 but amplification does not necessarily guarantee a desired response. The fundamental issue with

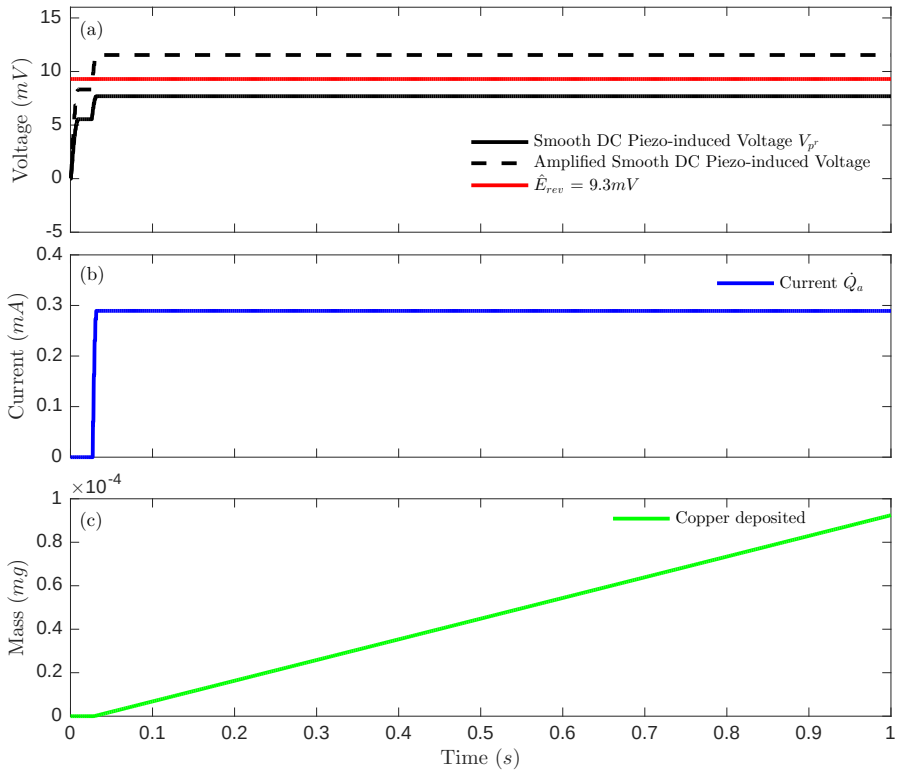

Figure 2.14: For less severe conditions, the piezo-induced voltage can be amplified to establishes the chemical kinetic needed to deposit copper nanoparticles. For example, a stress level equivalent to 0.2 N produces the same effect as a stress level equivalent to 0.3 N. Amplification leads the system to operate more in an open-loop as opposed to a passive self-healing mode.

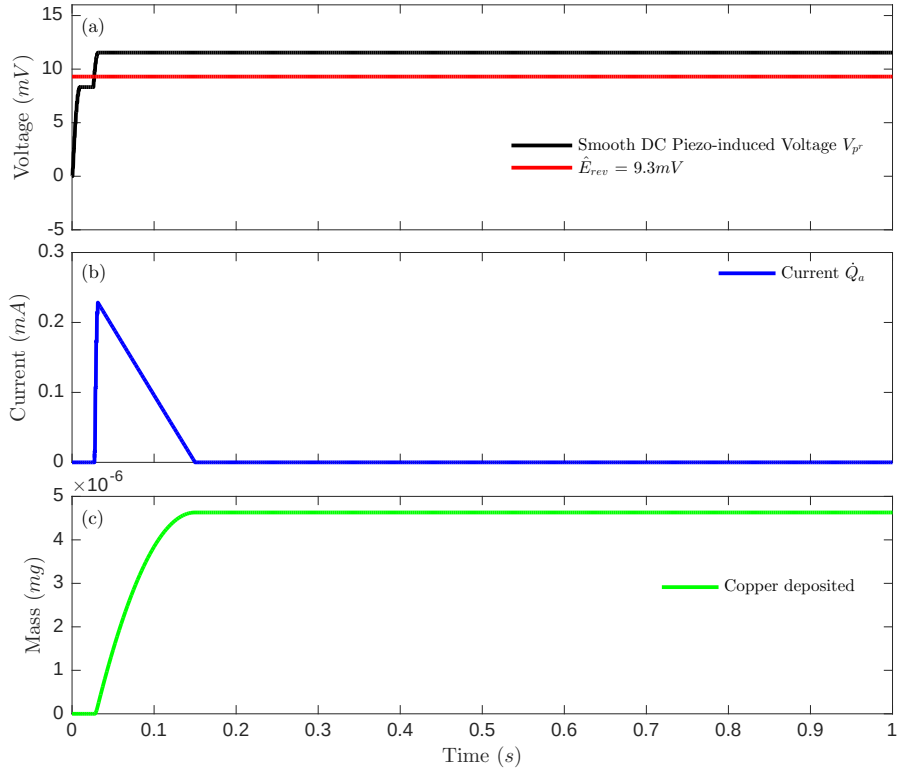

Figure 2.15: The effect of uncertainties in constant environmental conditions. The piezo-induced voltage is greater than $\hat{E}_{rev}$ but the healing process operates in the dead-zone region from about 0.15 s. As a result, there is a drop in mass of copper nanoparticles deposited.

this arrangement is that the piezoelectric and electrolyte are mixed in the self-healing material and can not be considered as separate elements. Nonetheless, this analysis shows the effect of amplification from a conceptual point of view.

To illustrate the effect of uncertainty or disturbance, the term $A_n sin\ (t)$ defines unknown disturbances, uncertainties or unmodeled dynamics of a self-healing process (where A_n represents the amplitude of the disturbance). The term has been chosen primarily for analysis and in accordance with what is found in literature (Jasim, 2013; Wang et al., 2004). A mathematical model for this self-healing process is expressed in Equation (2.33).

$$\dot{Q}_a(t) = m\Big(V_{p^r} - A_n sin\ (t)\Big) + \Delta I(t) \tag{2.33}$$

The term A_n is chosen as 10 mV to capture a system influenced by high disturbance. The simulation result for a stress level equivalent to 0.3 N is shown in Figure 2.15. The smooth DC piezo-induced voltage is greater than $\hat{E}_{rev}$ but the healing process operates in the dead-zone region between 0.15 and 1 *second* and results in no self-healing. The performance of the self-healing process is poor when compared with the results achieved in Figures 2.13 and 2.14. This is the effect of uncertainties, disturbances or unmodeled dynamics of a self-healing process. Importantly, a typical self-healing process and its equivalent open loop arrangement are unreliable and poor in handling disturbances or uncertainties since there are no feedback mechanism to ensure a desired healing response.

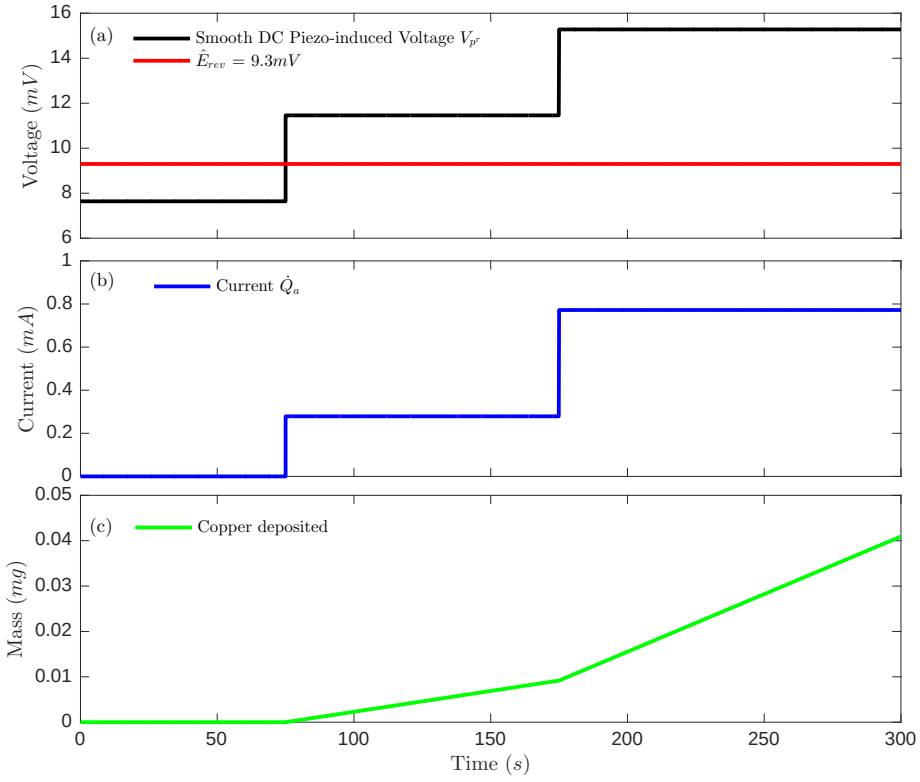

Figure 2.16: In varying environmental conditions, different piezo-induced voltages are generated at different time instants. This could result in a dead-zone region at any time; e.g. between 0 to 75 seconds, the piezo-induced voltage is less than $\hat{E}_{rev}$. During this period, there is no current flow and mass deposition of copper nanoparticles. At other times, the self-healing process operates in the current flow region.

More often than not, materials are exposed to varying environmental conditions. For example, in-flight aircraft experience turbulence, civil constructions experience shock in form of vibration, etc. An example simulation is the stress levels applied at different time instants at 138 rad/sec. The stresses are equivalent to forces of 0.2 N, 0.3 N and 0.4 N. These generate smooth DC piezo-induced voltages of 7.64 mV, 11.46 mV and 15.28 mV respectively shown in black line of Figure 2.16a. Figure 2.16b shows the corresponding current flow during self-healing. The simulation does not consider the effect of uncertainties or disturbances. Between 0 and 75 seconds, no current flow was recorded; this is a pointer to the insufficient voltage. Beyond 75 second, there is enough current flow to cause the chemical kinetics needed to deposit the healing agent. The copper nanoparticles deposited during this time is shown in Figure 2.16c. Similarly, the effect of uncertainties or disturbances is shown in Figure 2.17. This causes a fluctuation in the current flow and results in a deposition drop of 73.43%, when compared with the disturbance free self-healing process in Figure 2.16.

In general, the performance of the self-healing process is poor because the composite material does not generate sufficient voltage to consistently initiate the self-healing process. More so, the examples simulated in Figures 2.12 - 2.17 show that a typical self-healing process is an unregulated process. This is because the healing process does not guarantee that the onset of damage is stopped. The process is unable to achieve the desired healing response over a period of time and handling of uncertainty/disturbance is also poor. Given the time frame of this research, experimental validation of the simulations was not carried out because the material needs to be prepared by specialist in material science.

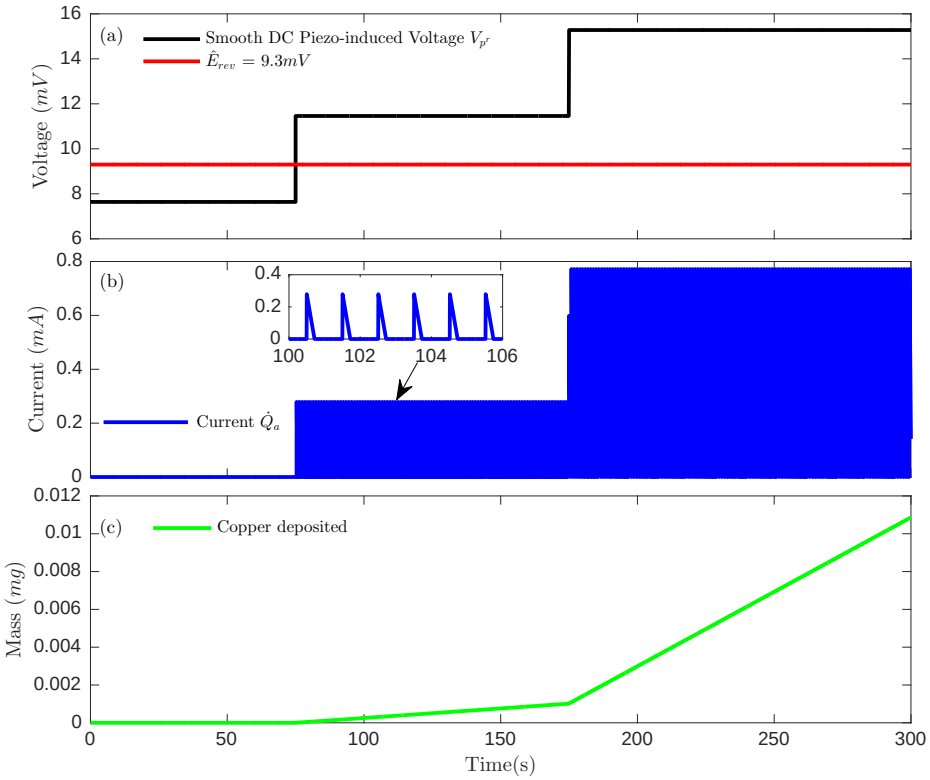

Figure 2.17: The effect of uncertainties in varying environmental conditions. (a) The piezo-induced voltages are generated at different time instants. (b) In addition to the dead-zone effect between 0 to 75 seconds, the effect of uncertainties results in fluctuation in current flow. (c) This causes a drop in the mass of copper nanoparticles deposited.

2.6 Summary

The chapter provides the first (to my knowledge) mathematical description of a self-healing mechanism of an electromechanical composite material. The model parameters were estimated from the experimental set-up of the electrolysis of copper (II) sulphate. Example simulations are provided to show some of the drawbacks of passive self-healing and an open loop self-healing system. A typical self-healing process is an unregulated passive system that may not effectively counteract the onset of damage and does not account for uncertainty or disturbance or non-linearities in a system. As a result, the match between the damage and healing rate may not be guaranteed. This generally affects the performance of self-healing. Also, in an open loop arrangement, amplification

does not necessarily guarantee a desired response. As this is a feed-forward with gain, the arrangement is unreliable and does not benefit from feedback mechanism to ensure the match between the damage and healing rate. More so, this set-up is only possible when the piezoelectric and electrolytic process are considered as separate element and not mixed within the self-healing material. Lastly, preparation of the self-healing material requires expertise in material science and as a result, experiments were not performed.

In the next chapter the passive self-healing will be extended to a closed loop self-healing system to regulate and establish a match between user or environmental demands, such as the damage rate.

Chapter 3

Active Self-healing

3.1 Introduction

In the previous chapter, a mathematical model description of a self-healing mechanism was formulated. This demonstrated some of the drawbacks of passive self-healing. A typical passive self-healing process is unregulated and does not take into account uncertainties and disturbances. In addition, the designed self-healing model in this research is associated with a non-linear dead-zone that makes the self-healing process insensitive to actuation when the voltage is less than the potential barrier E_{rev}. This could adversely affect the performance of the healing process. More so, as the match between the damage and healing rate is not guaranteed.

In this chapter, a novel closed loop self-healing system- referred in this research as "active self-healing" is presented. The arrangement takes advantage of sensing and feedback control to regulate the healing rate to meet user or environmental demands, such as the need to match the damage rate. The majority of the control related works on electrolysis are incorporated into one form of power generation management scheme or the other (Pérez-Herranz et al., 2010; Valenciaga and Evangelista, 2010; Zhou and Francois, 2009). The control objective is to convert excess power generated from renewable sources such as wind energy, solar panel, etc. into hydrogen through the electrolysis

of water and maintain the flow rate of hydrogen from the electrolyser to the hydrogen storage tank. The energy management set-up assumes sufficient power supply either from an energy source or an external battery to drive the electrolysis process and maintain the production of hydrogen. In cases of scarce energy supply or low battery state, the electrolyser shuts down until there is sufficient energy supply (Kauranen et al., 1993; Valenciaga and Evangelista, 2010). The set-up is such that the control strategy does not account for the inherent dead-zone non-linearity of an electrolytic process.

In the context of control, the inherent non-linear dead-zone identified in section 2.2.2 undermines the performance of this self-healing mechanism. For these kinds of non-linear systems, conventional feedback control will not produce close to optimal performance (Isermann et al., 1992; Slotine and Li, 1991). As the conventional feedback controller will be designed with fixed gains, it is unlikely to achieve the desired performance when faced with a change in dynamics resulting from the dead-zone, thus making it unsuitable for this application. A robust control design can be implemented but outside the designed bounds, unaccounted variation can affect the performance of the system. However, adaptive control has been implemented for this class of system and results have shown that a desired response can be achieved (Harris and Billings, 1985; Isermann et al., 1992; Krstic et al., 1995; Slotine and Li, 1991). An adaptive controller evolves by generating new control gains over time so as to drive the mismatch between a desired response and the actual system response to zero. As such, adaptive control is suitable for the active self-healing system. The contributions of this chapter are:

- Develop an active self-healing system to regulate the healing process to meet user or environmental demands such as the damage rate.
- Demonstrate through simulation the effectiveness of the active self-healing system.

In the following (Kuponu et al., 2016, 2017a,b), the design architecture of adaptive control is presented in Section 3.2. Mathematical sliding mode

control formulations and integration with two passive self-healing models in a closed loop arrangement are presented in Section 3.3. The section also includes example simulations and a discussion of the closed loop self-healing systems. A sensitivity analysis of the proposed active self-healing system is detailed in Section 3.4. This is followed by a summary in Section 3.5.

3.2 Adaptive Control Architectures

Generally, there are two architectures of adaptive control implementation, namely: model reference adaptive control (MRAC) and model identification adaptive control (MIAC) (Harris and Billings, 1985; Isermann et al., 1992; Krstic et al., 1995; Slotine and Li, 1991).

3.2.1 Model Reference Adaptive Control (MRAC)

The setup of MRAC in Figure 3.1 consists of a reference model, controller, system and adaptation law. The reference model represents an ideal system

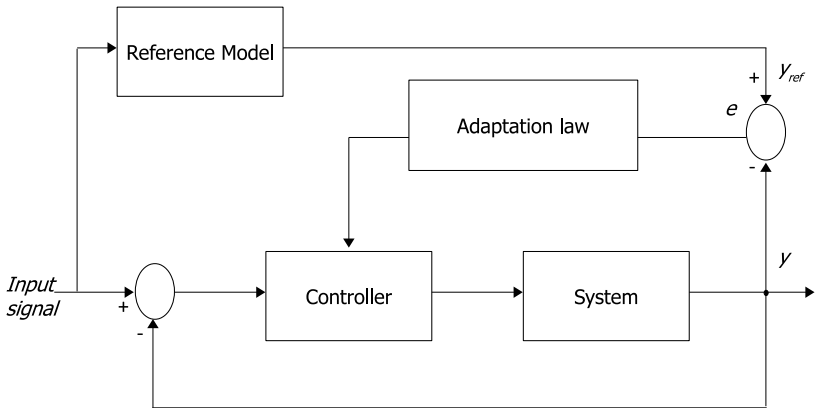

Figure 3.1: Architecture of a model reference adaptive control (MRAC).

that meets requirements of a desirable system performance and/or stability. The system in this context is a mathematical model that represents an actual physical process that is being controlled. The optimal goal of the controller is to match the actual system output y with the reference model y_{ref}; that is, to drive

the error signal ($e = y_{ref} - y$) to zero. It is achieved by solving an optimisation problem that evaluates new gains for the controller, particularly for a time varying input signal. The new gains become the output of the adaptation law. Unlike conventional feedback controllers, the adaptive controller continually changes the gains but it is essential to keep the system stable while doing so. This is a challenge but techniques such as Lyapunov theory, passivity theory, hyperstability, etc. are used to ensure that the system remains stable.

3.2.2 Model Identification Adaptive Control (MIAC)

MIAC is also known as the self-tuning controller and eliminates the need for a reference model. Its architecture in Figure 3.2 consists of a controller, a system and a system identification tool. The principle behind its operation centres on

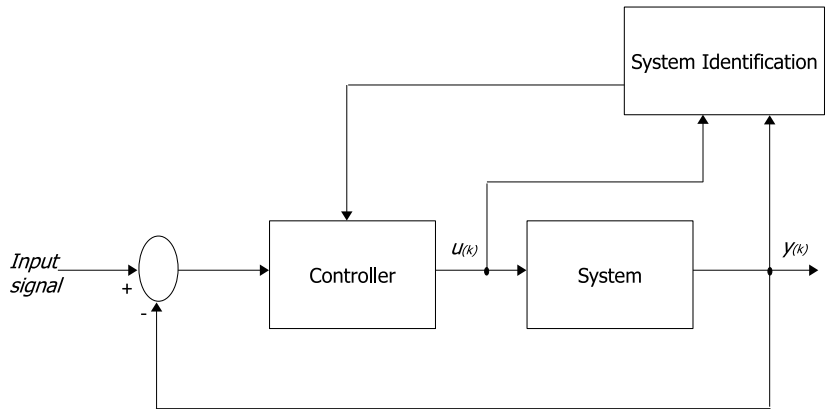

Figure 3.2: Architecture of a model identification adaptive control (MIAC).

acquiring the current state of the system through system identification. System identification techniques such as recursive least square, Kalman filter, etc. can be used to estimate the states of the system and based on the estimate, new controller parameters can be evaluated by an adaptive estimator and applied to the controller to achieve the desired system response.

3.3 Adaptive Sliding Mode Control (SMC)

A typical passive self-healing process is unregulated and does not take into account uncertainties and disturbances. In addition, the designed self-healing model in this research is associated with a non-linear dead-zone that makes the self-healing process insensitive to actuation when the voltage is less than the potential barrier E_{rev}. This could adversely affect the performance of the healing process in matching the healing rate and the damage rate. Like engineering systems, controlling such systems with non-linearities and their associated uncertainties can be challenging. Particularly as model linearisation about an operating point does not capture all the dynamics of a real system. These generally affect the overall performance of the control system to optimally achieve a desired response. Conventional feedback controllers such as proportional-integral-derivative (PID), proportional-integral (PI), etc. can be designed with a level of robustness to accommodate the system non-linerities, uncertainties or disturbances and known system variations. As the conventional feedback controller is designed with fixed gains, it is unlikely to achieve a desired performance in applications with a high degree to uncertainties. For illustration, consider a case where the proposed self-healing scheme is used in airliner wings. Airliner wings are subjected to turbulence and varying environments as a result of unpredictable weather conditions. The performance of a feedback controller implemented with the proposed self-healing will vary and may not achieve a desired healing response because the controller is designed with fixed gains. A successful implementation of self-healing on a wide variety of systems that are deployed to different conditions means that self-healing must achieve a desired healing performance when there are non-linearities or unknown variations in the operating conditions. For these systems, adaptive controllers such as adaptive inverse controller, sliding mode controller, etc. are most suitable because the gains change over time to ensure a control action that would result in a desired response (Recker et al., 1991; Wang et al., 2004). More so, adaptive controllers can handle system non-linearities such as dead-zone,

backlash, hysteresis, etc. uncertainties or disturbances. The adaptive inverse controller is implemented by constructs an inverse non-linearity to cancel the effect of the system's nonlinearity (Recker et al., 1991). This scheme has been applied on systems that exhibit non-linearities like hydraulic actuators, electric servomotors, piezoelectric translators, etc. (Cho and Bai, 1998; Recker et al., 1991; Tao and Kokotovic, 1995a,b; Zhou et al., 2006).

Initial accounts of SMC were recorded in the old Soviet Union and has over the decades evolved in many applications (Draženović, 1969; Korovin and Utkin, 1974; Utkin, 1977). This includes flight control (González et al., 2014; Spurgeon and Davies, 1993; Tasaltin and Jafarov, 2000), robotic control (Cui et al., 2017; Feng et al., 2002; Man Zhihong et al., 1994; Nekoukar and Erfanian, 2011), electric drives (Barambones and Alkorta, 2011; Utkin, 1993; Zhang Yan and Utkin, 2002; Zheng et al., 2015), etc. In particular, SMC has been implemented to ensure tracking position of robotic manipulator system with dead-zone (Corradini and Orlando, 2003; Han and Lee, 2013; Jasim and Plapper, 2013). Similarly, dead-zone non-linearity has been compensated with SMC in servo system to ensure an optimal performance (Bessa et al., 2010; Chen et al., 2016; Liu et al., 2013b; Zhonghua et al., 2006). In addition to the advantages of adaptive control, this research uses the adaptive sliding mode control because of its fast response and good transient performance.

An adaptive sliding mode control can be designed to achieve a desired system response by following these two steps (Bartolini et al., 2003; Pisano and Usai, 2011; Spurgeon, 2008; Young et al., 1996):

1. Define a switching manifold known as sliding surface.

2. Design a discontinuous control action such that the system trajectory lies within the sliding surface. with the adaptive gains evaluated using Lyapunov stability theory.

3. Evaluate the controller gains using Lyapunov stability theory. This step introduces the adaptive feature of SMC.

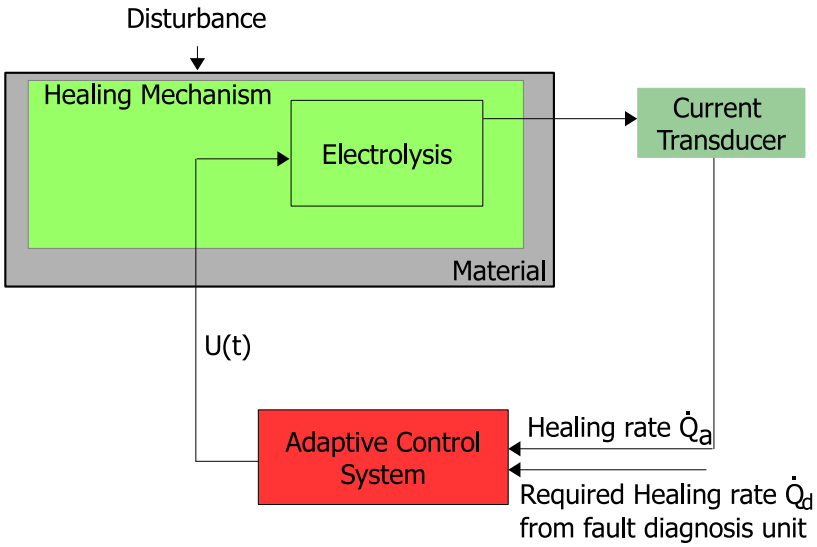

Figure 3.3: An isolated electrolytic process used to demonstrate how a non-linear self-healing process can be regulated by adaptive feedback control.

3.3.1 Design I: Adaptive SMC Design Implementation for Electrolytic Self-healing Process

Consider an isolated electrolytic self-healing process (see Figure 3.3) given as Equation (3.1) with a non-linear function defined in Equation (3.2) and described in Subsection 2.3. The terms $\dot{Q}_a$, U, m, E_{rev} and t define the actual current flow during electrolysis, control input, material parameter, reversible potential barrier and time respectively.

$$\dot{Q}_a(t) = mU(t) + \Delta I(t) \tag{3.1}$$

$$\Delta I(t) = \begin{cases} -mE_{rev} & \text{for } U(t) > E_{rev} \\ -mU(t) & \text{for } U(t) \leq E_{rev} \end{cases} \tag{3.2}$$

This represents a composite material whose healing mechanism is based on electrolysis, that is, mass is deposited to provide healing. An adaptive sliding mode controller is implemented based on steps (1 - 2) in Section 3.3 above.

This is based on a previous mathematical formulation (Jasim, 2013; Slotine and Li, 1991; Su and Stepanenko, 2000; Wang et al., 2004) and follows the MRAC architecture described in Subsection 3.2.1, since the damage rate of a composite material can be used as the reference model to give an insight on the expected healing rate. The essence of implementing an adaptive sliding mode controller is to handle the inherent dead-zone non-linearity identified as a drawback to this self-healing mechanism in Chapter 2. The control objective is for the actual current ($\dot{Q}_a$) during electrolysis to track a desired current $\dot{Q}_d$ for the self-healing process. The desired current $\dot{Q}_d$ is in effect a function of the desired healing rate of the process. As such, the following assumptions hold during the design of the adaptive SMC:

Assumption 3.1. The material parameter m is unknown but bounded by $m \in [m_{min} \quad m_{max}]$.

Assumption 3.2. The reversible potential barrier E_{rev} is unknown but bounded by $E_{rev} \in [E_{revmin} \quad E_{revmax}]$.

Assumption 3.3. The term $\Delta I(t)$ is unknown but bounded. That is, $|\Delta I(t)| \leq \rho_c$ and $\rho_c = m_{max} E_{revmax}$.

Assumption 3.4. The reference model $\dot{Q}_d$ is known.

Step 1: Surface Design

The sliding surface ($s = 0$) is usually a linear combination of the tracking error and its derivatives. In the design stage, a sliding surface is selected in place of the tracking error. This is because the tracking error is automatically driven to zero once the surface is zero. By ensuring that the system trajectories slide and remain on the surface ($s = 0$) as shown in Figure 3.4, the tracking error between the desired and actual response is zero. To begin, Equation (3.3) defines a surface $s = 0$.

$$s(t) = \lambda_c \tilde{Q}(t) \tag{3.3}$$

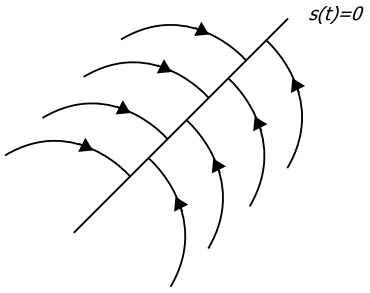

Figure 3.4: The Sliding surface $s = 0$**.** The system trajectory slides on the surface as the controller ensures a match between the reference and actual model.

The term λ_c is a strictly positive constant, $\tilde{Q}(t) = Q_a(t) - Q_d(t)$ and the derivative of $\tilde{Q}(t)$ is the tracking error. This suggests that the surface ($s = 0$) has a unique solution $\tilde{Q}(t) = 0$.

Step 2: Control Design

The control objective is for the actual current ($\dot{Q}_a$) during electrolysis to track a desired current ($\dot{Q}_d$) during the self-healing process. This is achieved by designing a control input $U(t)$ such that the system trajectory slides to the surface ($s = 0$) defined in Equation (3.3). That is, the control input $U(t)$ must satisfy the condition in Equation (3.4), where η is a positive constant. This is referred to as the reaching condition and implies that for all system trajectories, the squared distance to the surface is non-increasing.

$$\frac{1}{2}\frac{d}{dt}s^2 \leq -\eta|s| \tag{3.4}$$

Given that the system trajectory begins at an arbitrary position $s(0)$, the trajectory reaches the surface $s(t_{reach})$ at a finite time t_{reach} in Equations (3.5) - (3.6).

$$\begin{aligned} s(t_{reach}) - s(0) &\leq -\eta(t_{reach} - 0) \\ 0 - s(0) &\leq -\eta t_{reach} \end{aligned} \tag{3.5}$$

$$t_{reach} \leq \frac{|s(0)|}{\eta} \tag{3.6}$$

To keep $\dot{s} = 0$, Equation (3.7) suggests an approximate control input $\hat{U}$ in Equation (3.8).

$$\begin{aligned} \dot{s}(t) =& \lambda_c \dot{\tilde{Q}}(t) \\ =& \lambda_c \Big[\dot{Q}_a(t) - \dot{Q}_d(t) \Big] \\ =& \lambda_c \Big[mU(t) + \Delta I(t) - \dot{Q}_d(t) \Big] \end{aligned} \tag{3.7}$$

$$\hat{U} = \frac{1}{m} \Big[- \Delta I(t) + \dot{Q}_d(t) \Big] \tag{3.8}$$

Since the sliding mode controller is a variable structure controller, Equation (3.8) is rewritten in a discontinuous form, such that the controller switches while ensuring that the system trajectories slide to the surface. The control input becomes Equation (3.9) and satisfies the condition expressed in Equation (3.4).

$$U(t) = \hat{U} - K_d s(t) - \eta sgn(s(t)) \tag{3.9}$$

In Equation (3.9), the terms $1/m$ and $\Delta I(t)$ are unknown but bounded as stated in the design assumptions above. Let $\hat{\phi}$ be the estimate of $\phi \triangleq [1/m]$ such that $\tilde{\phi} = \hat{\phi} - \phi$ and the term K_d be a positive constant.

In practice, a discontinuous control designed in Equation (3.9) can be damaging. As the controller switches between both sides of the surface $s = 0$, a phenomenon called chattering occurs (Utkin and Hoon Lee, 2006). This occurs when unmodelled high frequency dynamics are excited, leading to undesirable oscillation shown in Figure 3.5. Thus, a limit on the performance of the control action to drive the actual current ($\dot{Q}_a$) during electrolysis to a desired current ($\dot{Q}_d$) in self-healing mode. To eliminate this phenomenon, a boundary is created around the surface. One of the ways to achieve this is by replacing the sign function with a saturation or hyperbolic tangent function (Slotine and Li, 1991; Song and Smith, 2000). This ensures a continuous control action to drive a

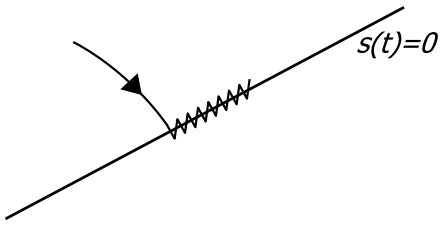

Figure 3.5: Chattering resulting from unmodelled dynamics of the system. This could potentially limit the performance of the sliding mode controller and have adverse effect on the self-healing process.

desirable performance. As a result, a tuning error s_ϵ in Equation (3.10) replaces the surface $s(t)$ in Equation (3.3).

$$s_\epsilon = s - \epsilon sat\left(\frac{s}{\epsilon}\right) \tag{3.10}$$

$$sat(z) = \begin{cases} 1 & \text{for } z \leq 1 \\ z & \text{for } -1 < z < 1 \\ -1 & \text{for } z \leq -1 \end{cases} \tag{3.11}$$

The control law $U(t)$ becomes Equation (3.12).

$$U(t) = -K_d s(t) + \hat{\phi}\dot{Q}_d(t) - k^* sat\left(\frac{s}{\epsilon}\right) \tag{3.12}$$

The term $k^* sat(s/\epsilon)$ in Equation (3.12) introduces robustness to compensate for the unknown $\Delta I(t)$ and $k^* \geq \rho_c/m_{min}$.

Step 3: Adaptive Gain Evaluation

The attractive feature of adaptive control is the ability to use the adaptive mechanism to re-evaluate its gain when there is variation in system dynamics or conditions. It is essential that the re-evaluated gain does not cause the controller to drive the system to instability at all times. Approaches such as Lyapunov stability theory, hyperstability, passive theory, etc. can be used to re-evaluate a stable update gain (Slotine and Li, 1991). Lyapunov stability

theory is selected to evaluate the adaptive gain as it is the most commonly used. The stability is established by Theorem 3.1.

Theorem 3.1. *Consider the non-linear self-healing system, the surface $s(t)$, the tuning error s_ϵ and the control law $U(t)$ expressed in Equations (3.1), (3.3), (3.10) and (3.12) respectively. If the adaptive law $\dot{\hat{\phi}}$ is selected as Equation (3.13), then the control design guarantees that the system trajectory will converge to the sliding mode. This means that the the tracking error converges to zero over time.*

$$\dot{\hat{\phi}} = -\gamma\lambda_c\dot{Q}_d(t)s_\epsilon \tag{3.13}$$

Proof. Consider the Lyapunov function Equation (3.14).

$$W(t) = \frac{1}{2}\left(\frac{1}{m}s_\epsilon^2 + \frac{1}{\gamma}\tilde{\phi}^2\right) \tag{3.14}$$

The derivative of W over time is given by Equation (3.15).

$$\dot{W}(t) = \frac{1}{m}s_\epsilon\dot{s} + \frac{1}{\gamma}\tilde{\phi}\dot{\hat{\phi}} \tag{3.15}$$

Equation (3.7), Equation (3.12) and $\tilde{\phi} = \hat{\phi} - \phi$ are substituted into Equation (3.15) to give Equation (3.16).

$$\begin{aligned}\dot{W}(t) = &-\lambda_c K_d s_\epsilon s + \lambda_c s_\epsilon\left(\hat{\phi}\dot{Q}_d(t) - k^* sat\left(\frac{s}{\epsilon}\right)\right)\\ &+ \lambda_c s_\epsilon\left(\frac{\Delta I(t)}{m} - \phi\dot{Q}_d(t)\right) + \frac{1}{\gamma}\left(\hat{\phi} - \phi\right)\dot{\hat{\phi}}\end{aligned} \tag{3.16}$$

To eliminate the terms with ϕ and $\hat{\phi}$ in Equation (3.16), the adaptive law $\dot{\hat{\phi}}$ is selected as Equation (3.17). This is substituted into Equation (3.16) to give the expressions in Equations (3.18) - (3.19).

$$\dot{\hat{\phi}} = -\gamma\lambda_c\dot{Q}_d(t)s_\epsilon \tag{3.17}$$

$$\begin{aligned}\dot{W}(t) = &- \lambda_c K_d s_\epsilon s + \lambda_c s_\epsilon \left(\hat{\phi}\dot{Q}_d(t) - k^* sat\left(\frac{s}{\epsilon}\right)\right) \\ &+ \lambda_c s_\epsilon \left(\frac{\Delta I(t)}{m} - \phi \dot{Q}_d(t)\right) \\ &+ \frac{1}{\gamma}\left(\hat{\phi} - \phi\right)(-\gamma \lambda_c \dot{Q}_d(t) s_\epsilon)\end{aligned} \tag{3.18}$$

$$\dot{W}(t) = -\lambda_c K_d s_\epsilon s - \lambda_c k^* s_\epsilon sat\left(\frac{s}{\epsilon}\right) + \frac{\Delta I(t)}{m}\lambda_c s_\epsilon \tag{3.19}$$

Equation (3.10) is substituted into Equation (3.19) to give Equation (3.20).

$$\begin{aligned}\dot{W}(t) = &- \lambda_c K_d s_\epsilon \left(s_\epsilon + \epsilon sat\left(\frac{s}{\epsilon}\right)\right) - \lambda_c k^* s_\epsilon sat\left(\frac{s}{\epsilon}\right) \\ &+ \frac{\Delta I(t)}{m}\lambda_c s_\epsilon\end{aligned} \tag{3.20}$$

When $|s| \leq \epsilon$, $|s_\epsilon| = 0$ and Equation (3.20) becomes zero (Equation (3.21)).

$$\dot{W}(t) = 0 \qquad \forall |s| \leq \epsilon \tag{3.21}$$

When $|s| > \epsilon$, $|s_\epsilon| = s_\epsilon sat(s/\epsilon)$. By also taking into account $k^* \geq \rho_c / m_{min}$, Equation (3.20) is expressed to give Equations (3.22) - (3.24).

$$\dot{W}(t) = -\lambda_c K_d s_\epsilon^2 - (K_d \epsilon + k^*)\lambda_c |s_\epsilon| + \frac{\Delta I(t)}{m}\lambda_c s_\epsilon \tag{3.22}$$

$$\dot{W}(t) \leq -\lambda_c K_d s_\epsilon^2 - K_d \epsilon \lambda_c |s_\epsilon| - \left(k^* - \frac{\Delta I(t)}{m}\right)\lambda_c |s_\epsilon| \tag{3.23}$$

$$\dot{W}(t) \leq -\lambda_c K_d s_\epsilon^2 \qquad \forall |s| > \epsilon \tag{3.24}$$

Remark. Equation (3.21) and Equation (3.24) indicate that the surface $s(t)$, tuning error s_ϵ and adaptive law $\tilde{\phi}$ are globally bounded and the tracking error converges to zero over time.

3.3.2 Active Self-healing Example Simulation I

In this section, the effectiveness of active self-healing is illustrated by simulation. The model parameters are the same with the ones used in Section 2.5. The control parameters can be found in Table 3.1. These parameters are primarily chosen with the aim of verifying the concept of active self-healing.

Table 3.1: Control parameters of the Active Self-healing System. (Kuponu et al., 2016)

Parameter	Value
K^*	2.5
λ_c	5
K_d	50
γ	0.5
m_{min}	0.01
ϵ	0.01
η	0.06
Sample rate	0.005

In order to match the healing rate with the user or environmental demands (e.g. damage rate), a reference model that the adaptive controller will effectively track is needed. A varying reference model is selected to capture the damage rate. This is because the damage rate of a composite material varies over time. The varying reference is assumed to have a direct proportionality to the damage rate; thus, representing the extent of the damage rate. For an actual system, this is obtained through appropriate fault diagnosis and identification techniques; this is addressed in Chapter 5. An isolated electrolytic process that represents a self-healing composite material whose healing mechanism is based on electrolysis is simulated to show the concept of active self-healing. The adaptive SMC is tasked with ensuring that the current flowing during healing tracks a reference model. This action may lead to the chattering phenomenon described in Subsection 3.3.1. An example is shown in Figure 3.6. As a result, the actual current flow (see blue dashed line of Figure 3.6a) does not track the reference model shown in red line of Figure 3.6a. Also, the performance

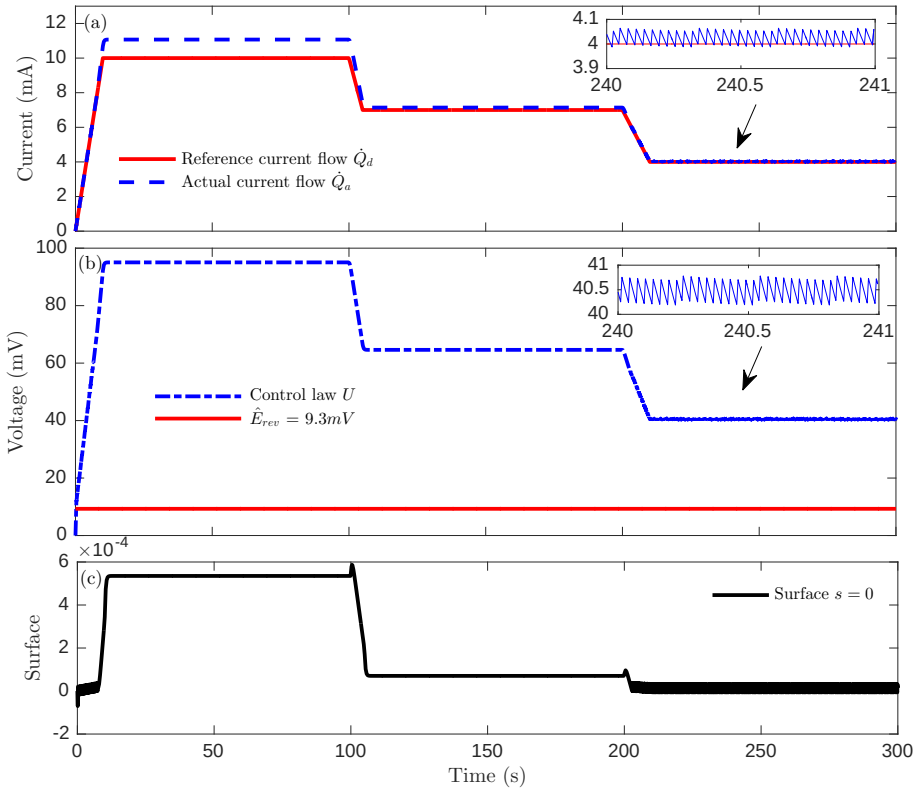

Figure 3.6: The chattering phenomenon is evident as the adaptive SMC poorly matches the reference and actual current. The defined reference and actual current represent the damage rate and healing rate respectively.

of the controller as it switches between the surface (Figure 3.6c) leads to an undesirable oscillation between $200s$ and $300s$ in Figure 3.6.

To avoid the chattering effect, a tuning error was used in place of the surface. The adaptive sliding mode controller produces a voltage greater than E_{rev} (see blue dashed line and red line of Figure 3.7a), that is, the system does not operate in the dead-zone region. This control action ensures that the actual current flow during healing (shown in blue dashed line of Figure 3.7b) tracks the changing reference model (red line of Figure 3.7b). Also, as the reference model changes, the adaptive law adjusts in order to achieve the primary tracking objective and avoids the chattering phenomenon. In terms of the self-healing process, achieving a desired current flow means that sufficient mass deposition of the healing agent is guaranteed and the healing rate is regulated to match the damage rate. The match ensures that the mass of copper nanoparticles

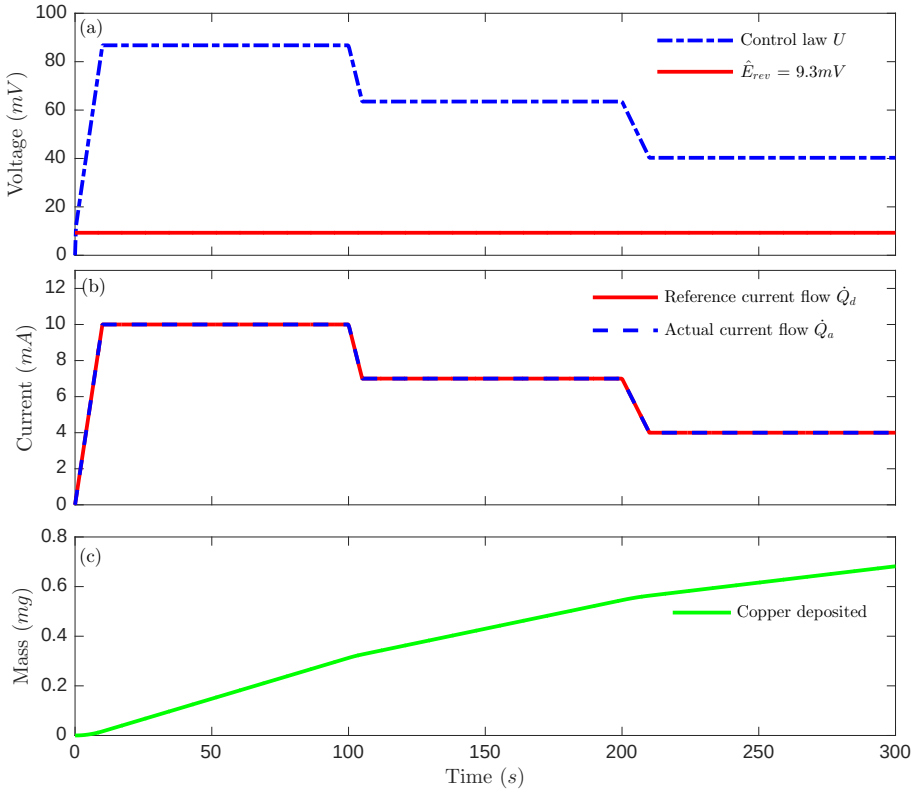

Figure 3.7: Adaptive SMC applied to a case where a disturbance free electrolytic self-healing process is regulated by a feedback control law. (a) The control effort of the adaptive SMC. (b) The actual current flow during electrolysis matches a defined reference current flow. The reference and actual current represent the damage rate and healing rate respectively. (c) The equivalent mass deposited over time for the closed loop active self-healing process.

deposited is controlled to effectively take up the void in the damage area. In this case, the controlled mass deposited is shown in Figure 3.7c. The blue line of Figure 3.8a shows the tracking performance of the adaptive SMC. The controller ensures fast convergence and a good tracking performance. The corresponding tuning error is shown in Figure 3.8b and compared with the surface in Figure 3.8c. Unlike the surface, the magnitude of the tuning error as the adaptive controller switches is restricted to a region $\leq |2.71 \times 10^{-20}|$, that is, the tuning error is more or less zero. Thus, preventing poor control performance and undesirable oscillations.

In practice, the performance of a self-healing process is affected by uncertainties, disturbances or unaccounted dynamics. The effectiveness of the

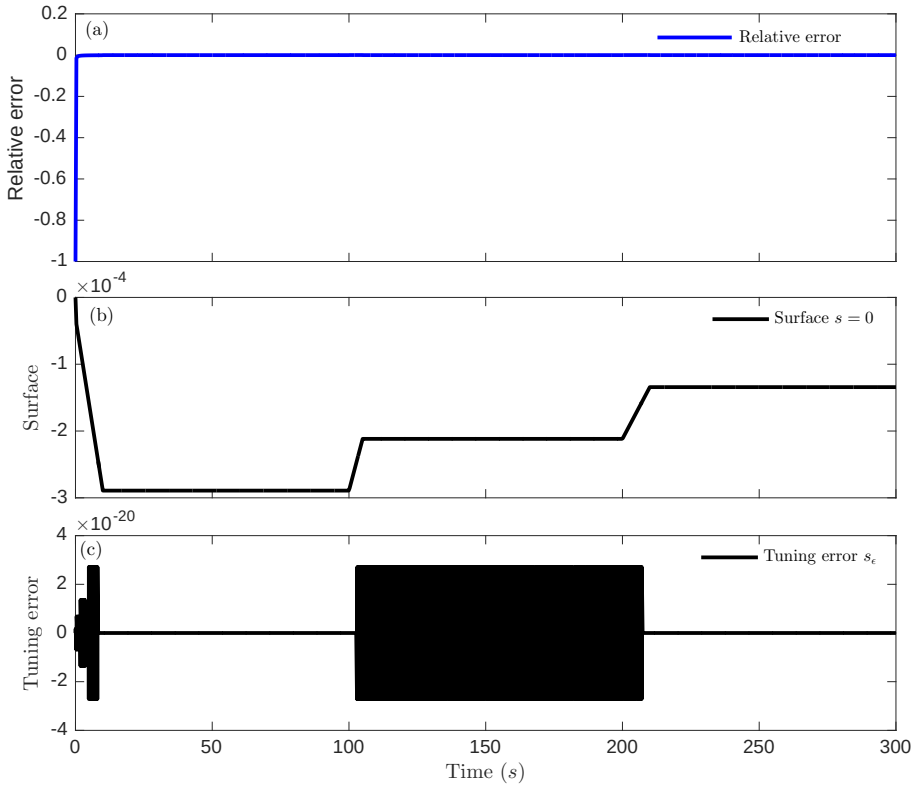

Figure 3.8: The control performance of the active self-healing process (a) Relative error defined as the difference between the actual and reference current divided by the reference current. (b-c) The sliding surface and the tuning error of the adaptive SMC.

adaptive SMC is investigated in the presence of these deterring factors. The self-healing model is defined as Equation (2.33) in Section 2.5. Since the uncertainties, disturbances or unaccounted dynamics are unknown, the additional term $A_n sin\ t$ in Equation (2.33) was excluded in the control design. Figure 3.9 shows the performance of the adaptive SMC. The control action in Figure 3.9a ensures that the actual current flow during healing (shown in blue dashed line of Figure 3.9b) tracks the reference model (red line of Figure 3.9b). The tracking performance of the controller is shown in Figure 3.9c and the corresponding sliding surface and tuning error can be found in Figure B.1 of Appendix B. The mass of copper nanoparticles deposited in Figure 3.9d is the same with the disturbance free self-healing process in Figure 3.7c. The results indicate that the active self-healing process can perform optimally with or without uncertainties.

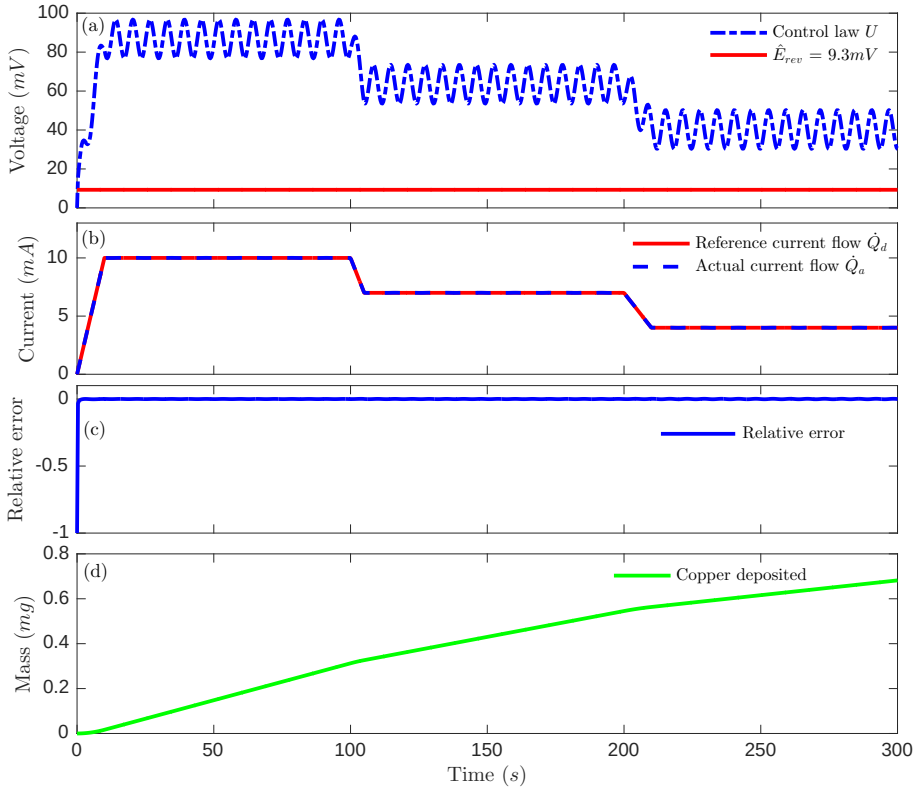

Figure 3.9: Adaptive SMC applied to a case where an isolated electrolytic self-healing process with uncertainties is regulated by a feedback control law. (a) The control effort of the adaptive SMC. (b) The actual current flow during electrolysis matches a defined reference current flow. The reference and actual current represent the damage rate and healing rate respectively. (c) Relative error defined as the difference between the actual and reference current divided by the reference current. (d) The equivalent mass deposited over time for the closed loop active self-healing process.

3.3.3 Design II: Adaptive SMC Design Implementation for Piezo-electrolytic Self-healing Process

Consider a composite material system whose self-healing is driven by a piezo-electrolytic process described in Chapter 2. The performance of self-healing is limited by the inherent dead-zone non-linearity of the system and the insufficient piezo-induced voltage $V_{p^r}(t)$ that drives the healing agent. An adaptive feedback controller in Figure 3.10 is designed to regulate the self-healing process, to overcome the inherent dead-zone and to ensure a proper match between damage and healing rate. In practice, the control system can be implemented using

either dSpace or National Instrument rapid control prototyping (RCP) hardware. The voltage demands of the control system is added by a power supply unit while a current transducer is attached to the electrodes to measure the current during electrolysis. A full description of the practical realisation is detailed in Section 5.2 of Chapter 5. The system model expressed in Equation (2.31) is

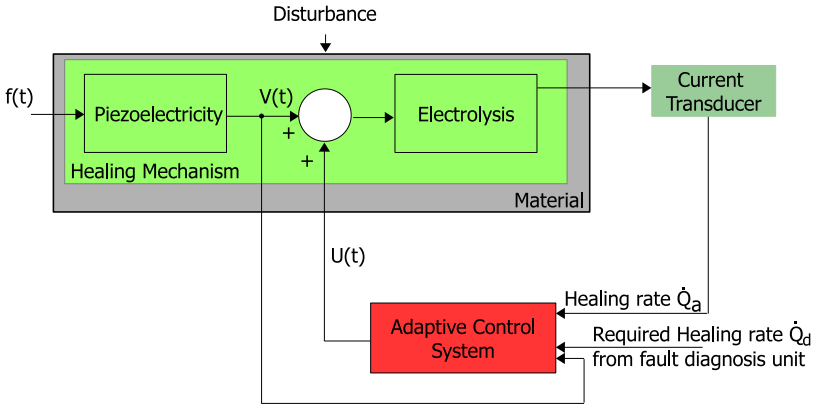

Figure 3.10: A piezo-electrolytic process to show how adaptive feedback control can regulate a non-linear self-healing process that is exposed to constant and varying stress input.

modified by adding a feedback control law $U(t)$ to give Equation (3.25).

$$\dot{Q}_a(t) = m(V_{p^r}(t) + U(t)) + \Delta I(t) \tag{3.25}$$

Following the design from Section 3.3.1, the derivative of the surface $\dot{s}(t)$ and the control law $U(t)$ are expressed as Equations (3.26) and (3.27) respectively.

$$\dot{s}(t) = \lambda_c m(V_{p^r}(t) + U(t)) + \lambda_c \Delta I(t) - \lambda_c \dot{Q}_d(t) \tag{3.26}$$

$$U(t) = -K_d s(t) - \hat{V}_{p^r} + \hat{\phi}\dot{Q}_d(t) - k^* sat\left(\frac{s}{\epsilon}\right) \tag{3.27}$$

$V_{p^r}(t)$ and ϕ are unknown during the control design but are estimated as $\hat{V}_{p^r}$ and $\hat{\phi}$ respectively using the Lyapunov stability theory, such that, $\tilde{V}_{p^r} = \hat{V}_{p^r} - V_{p^r}$ and $\tilde{\phi} = \hat{\phi} - \phi$. The stability is established by Theorem 3.2 and a detailed proof of this formulation can be found in Appendix A.

Theorem 3.2. *Consider the non-linear self-healing system, the surface $s(t)$, the tuning error s_ϵ and the control law $U(t)$ expressed in Equations (3.25), (3.3), (3.10) and (3.27) respectively. If the adaptive laws $\dot{\hat{\phi}}$, $\hat{V}_{p^r}$ are selected as Equations (3.28) - (3.29) respectively, then the control design guarantees that the system trajectory will converge to the sliding mode. The surface $s(t)$, tuning error s_ϵ and adaptive law $\tilde{\phi}$, $\tilde{V}_{p^r}$ are globally bounded and the tracking error converges to zero over time.*

$$\dot{\hat{\phi}} = -\gamma \lambda_c \dot{Q}_d(t) s_\epsilon \tag{3.28}$$

$$\dot{\hat{V}}_{p^r} = \lambda_c \Gamma s_\epsilon \tag{3.29}$$

3.3.4 Active Self-healing Example Simulation II

Composite materials whose piezo-electrolytic self-healing mechanism are subject to constant and varying conditions. The conditions are simulated as sinusoidal input forces with constant and changing amplitudes respectively to represent operating characteristics of structures, e.g. input from rotating machinery, wind gust on turbine, turbulence on an aircraft, waves on a ship, footfall on a bridge, etc. The effectiveness of the controller is investigated in the presence of uncertainties, disturbances or unaccounted dynamics. These uncertainties have not been considered in the control design. First, a material subject to constant conditions is simulated as concentrated constant stress level equivalent to 0.2 N at a frequency of 138 rad/sec. This generates a smooth DC piezo-induced voltage of 7.64 mV that is less than $\hat{E}_{rev} = 9.3\ mV$ as seen in the red lines of Figure 3.11a. As a result, the system operates in the dead-zone region and no healing or mass deposition is achieved. An adaptive SMC is implemented and tasked with overcoming the dead-zone non-linearity as well as generating sufficient voltage required to produce the desired mass transportation in the presence of uncertainties. The controller adapts to both the piezo-induced voltage and the varying reference, and accounts for the effect of uncertainties to

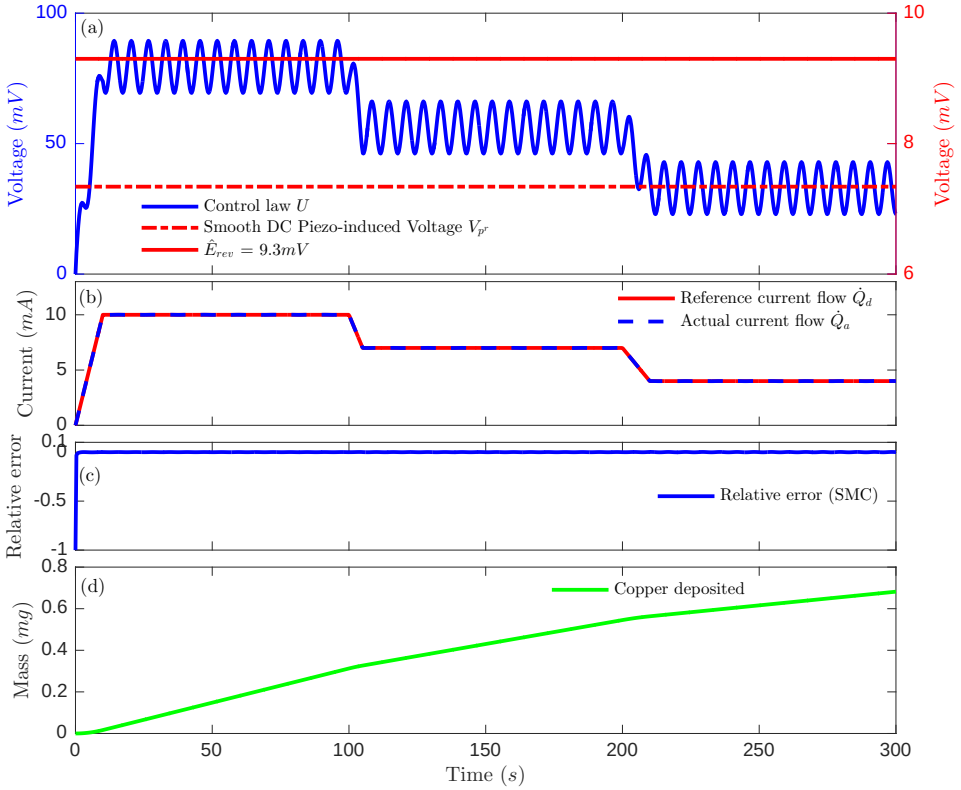

Figure 3.11: Adaptive SMC applied to a case where the composite material is subjected to constant load input in the presence of uncertainties. This depicts a material exposed to constant environmental conditions. (a) The piezo-induced voltage is insufficient to drive the healing process since $V_{pr} < \hat{E}_{rev}$. The feedback adaptive controller contribute an external input that ensures that the current flow during electrolysis tracks the desired performance. (b) The actual current flow during electrolysis matches a defined reference current flow. The reference and actual current represent the damage rate and healing rate respectively. (c) Relative error of the adaptive SMC defined as the difference between the actual and reference current divided by the reference current. (d) The equivalent mass deposited over time for the closed loop active self-healing process.

ensure that the actual current (see blue dashed line of Figure 3.11b) tracks the reference model (see red line of Figure 3.11b). It was observed that there was a drop in the control effort (see blue line of Figure 3.11a) when compared with the control effort of isolated electrolytic process in Figure 3.9a. This indicates that the controller takes into account the effect of the generated piezoelectric voltage. The performance of the adaptive SMC implementation can be seen in Figures 3.11c. In terms of the self-healing process, achieving a desired current

flow means that sufficient mass deposition of the healing agent is guaranteed and the healing rate is regulated to ensure a match with the damage rate. The match ensures that the mass of copper nanoparticles deposited is controlled to effectively take up the void in the damage area. The controlled mass deposited is shown in Figures 3.11d. In this sense, the piezoelectric acts as both a sensor to measure the effect of fault and an energy harvesting device.

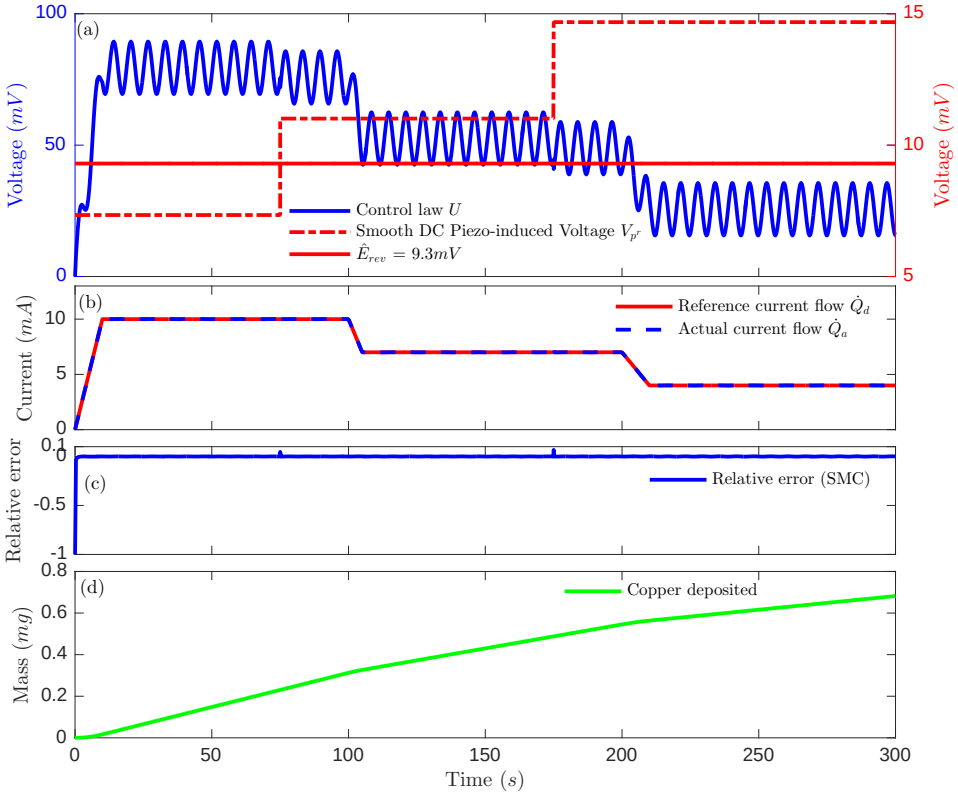

Figure 3.12: Adaptive SMC applied to a case where the composite material is subjected to different load inputs at different time instants and in the present of uncertainties. This depicts a material exposed to varying environmental conditions. (a) The piezo-induced voltage is insufficient to drive the healing process during the first 75 seconds since $V_{p^r} < \hat{E}_{rev}$. The feedback adaptive controller contributes an input and ensures that the current flow during electrolysis tracks the desired performance. (b) The actual current flow during electrolysis matches a defined reference current flow. The reference and actual current represent the damage rate and healing rate respectively. (c) Relative error of the adaptive SMC defined as the difference between the actual and reference current divided by the reference current. (d) The equivalent mass deposited over time for the closed loop active self-healing process.

Time varying conditions are demonstrated by applying stress levels equivalent to forces of 0.2 N, 0.3 N and 0.4 N at different time instants. The frequency is fixed at 138 rad/sec. These generate smooth DC piezo-induced voltages of 7.64 mV, 11.46 mV and 15.28 mV respectively as shown in red dashed line of Figure 3.12a. In passive mode, the current flow and mass deposited are shown in Figure 2.17b and Figure 2.17c of Section 2.5 respectively. It was observed that the system suffers from dead-zone non-linearity between 0 and 75 seconds; hence, no current flow or mass deposition during that time. Fluctuations in the current flow and a drop in the mass deposited (when compared with the disturbance free healing process in Figure 2.16) showed that the healing process is affected by uncertainties. As a result, the performance of the healing process is poor. The adaptive SMC is implemented and tasked with overcoming the dead-zone non-linearity and adapting to changes in both the piezo-induced voltage and the reference in the presence of uncertainties. As seen in Figure 3.12a, the controller adapts by dropping its effort while ensuring a proper tracking of the reference in Figure 3.12b. The sudden changes in the piezo-induced voltage produces transient spikes in the actual current flow, which eventually fades away as the controller adapts. This can be seen in the tracking error in Figure 3.12c. The corresponding sliding surface and tuning error can be seen in Figure B.3 of Appendix B. The controlled mass of copper nanoparticles deposited in Figure 3.12d can be compared with the corresponding open loop mass of copper nanoparticles deposited in Figure 2.17c. An increase of about 6170% was recorded in 5 minutes for the controlled system. Similar plots for a disturbance free active self-healing process can be found in Figures B.4 - B.7 of Appendix B. The simulations effectively show how important the concept of active self-healing can be to ensuring an optimal performance. In addition, the control implementation shows that an active self-healing process can handle uncertainties and the healing rate can be regulated to match the damage rate in different operating conditions.

3.4 Sensitivity Analysis of Active Self-healing

This section further investigates the effect of uncertainties on the active self-healing system. This is aimed at relating the proposed active self-healing to the real world where the degree of uncertainties due to disturbances, sensor noise, unmodelled dynamics, etc., are unknown, by investigating the performance of the adaptive SMC in the presence of uncertainties. A self-healing system coupled with uncertainties has been defined by Equation (2.33). The term $A_n = 10\,mV$ in Equation (2.33) is maintained and the proposed active self-healing was put to test by increasing the magnitude of the coupled uncertainties. Figures 3.13 - 3.14 show the outcome of the controller's effort at different magnitude of the defined uncertainties. Without any knowledge of the uncertainties, the

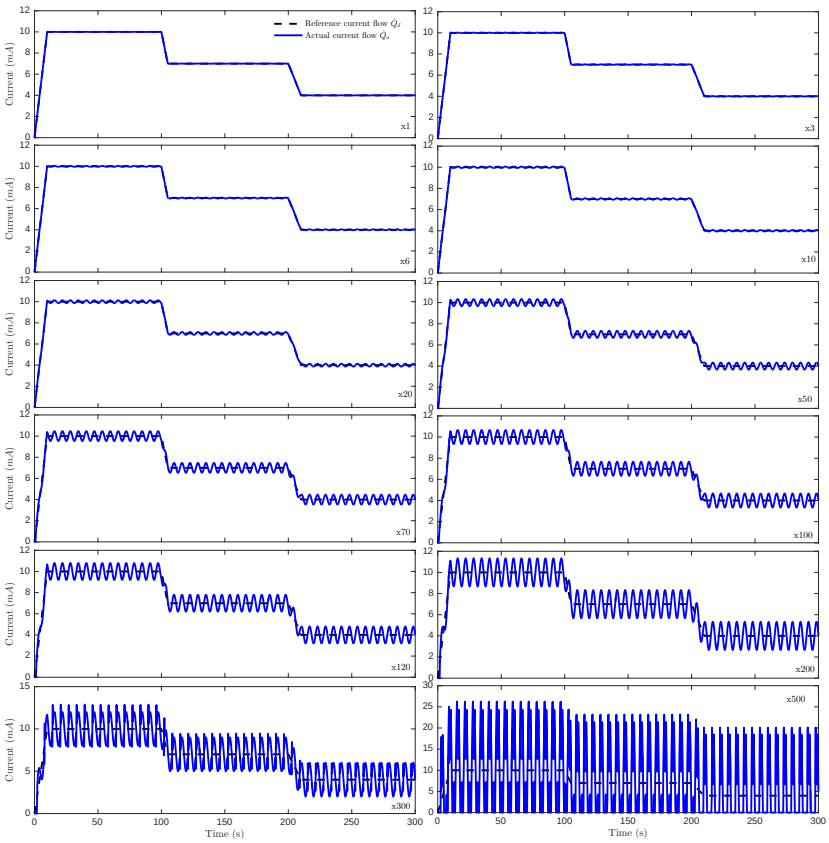

Figure 3.13: The effect of different magnitude of the defined uncertainties on the actual current flow during electrolysis.

controller adapts to guide the actual current flow on the reference profile. As the

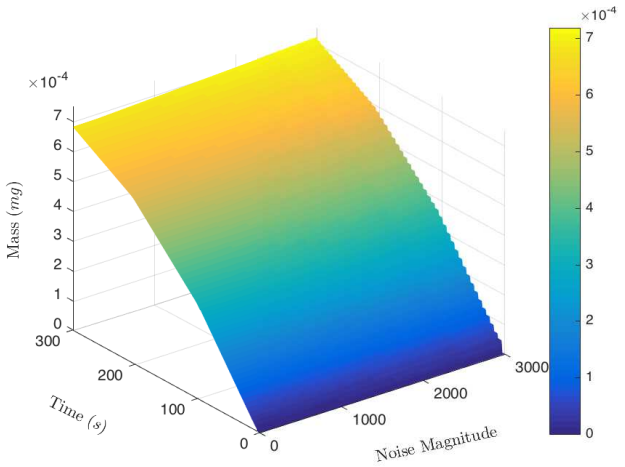

Figure 3.14: The equivalent mass deposition when exposed to different magnitude of the defined uncertainties.

magnitude of the defined uncertainties increases, the controller works hard to constrain the actual current flow $\dot{Q}_a$ to track the reference profile $\dot{Q}_d$. However, the influence of uncertainties on the healing system becomes pronounce as the magnitude increases and the controller's attempt to guide the current flow on the reference profile leads to oscillations as shown in Figure 3.13. This oscillation becomes undesirable as the magnitude of the uncertainty increases and could potentially lead the self-healing system to instability. Figure 3.14 shows the mass deposited over a range of uncertainties; beyond a magnitude of about 1000, a negligible increase in the mass deposited was recorded. While this shows the robustness of the proposed active active self-healing system, pronounce oscillation at a magnitude of 500 is undesirable.

Similarly, the effect of increasing the frequency of the sinusoidal noise was investigated as shown in Figures 3.15-3.16. The test evaluates the performance of the active self-healing system, particularly at higher frequencies. The result of the adaptive controller in Figure 3.15 shows that the actual current flow $\dot{Q}_a$ to track the reference profile $\dot{Q}_d$, but begins to oscillate as the frequency increases. The implication of this oscillation on the healing system as the frequency increases is an undesirable performance and instability. Nonetheless, the results show in adverse conditions resulting from increased noise frequency,

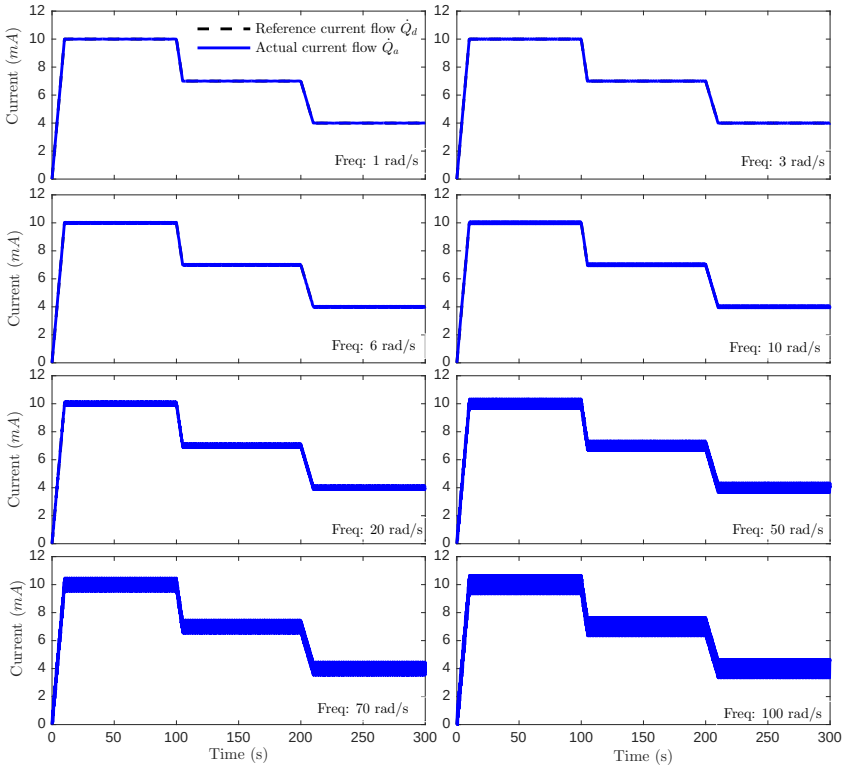

Figure 3.15: The effect of increasing the frequency of the defined uncertainties on the actual current flow during electrolysis.

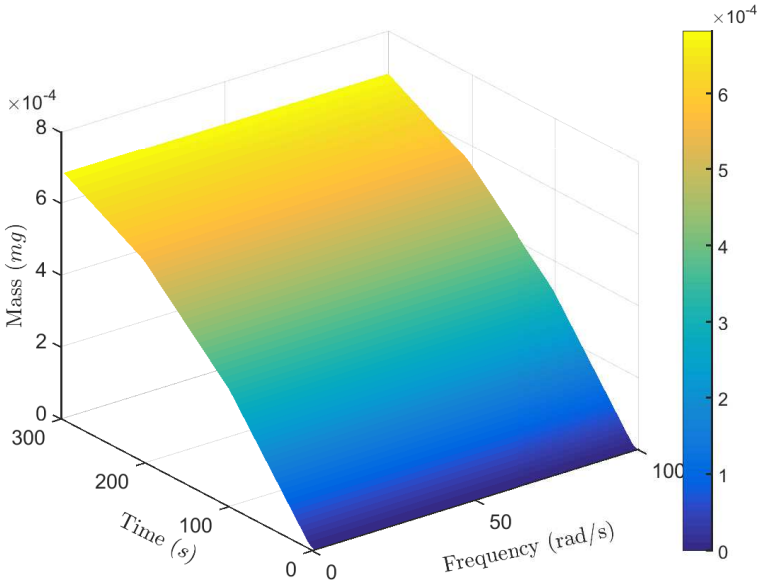

Figure 3.16: The equivalent mass deposition when exposed to different frequencies of the defined uncertainties.

the proposed active self-healing ensures a close to optimal performance of the healing process. In Figure 3.16, a negligible increase in the mass deposited was recorded beyond 20 rad/s.

Further investigation on the sensitivity of the active self-healing to uncertainties was performed. The proposed active self-healing was corrupted with random sensor noise. This uses a passive self-healing mechanism defined in Equation (3.30). The sensor noise $w(t)$ represents a white Gaussian noise that is drawn from a normal distribution with zero mean and variance σ^2, that is, $(w(t) \sim \mathcal{N}(0, \sigma^2))$.

$$\dot{Q}_a(t) = m\Big(V_{p^r} + w(t)\Big) + \Delta I(t) \tag{3.30}$$

Also, a measure of the noise is defined in terms of the signal to noise ratio (SNR) within a 99.7% confidence level. This is expressed in Equation (3.31); and the terms $\overline{V}_{p^r}$ and σ are the mean value of the piezo-induced voltage V_{p^r} and the standard deviation of the additive noise.

$$SNR = 20 \log_{10} \frac{\overline{V}_{p^r}}{6\sigma} \tag{3.31}$$

The results of different additive sensor noise are shown in Figures 3.17 - 3.18. A decrease in SNR means an increase in the effect of sensor noise on the self-healing system; which is potentially undesirable. However, the controller adapts to each of different sensor noise and ensures a tracking of the reference profile. The effect of noise was minimise by the controller, and as the SNR decreases below 6dB, a negligible increase in the mass deposited was recorded in Figure 3.18. Importantly, the results suggest that the active self-healing is robust to these uncertainties.

3.5 Summary

The chapter presents a novel closed loop self-healing system- referred to as active self-healing system. The system integrates the self-healing mechanism modelled

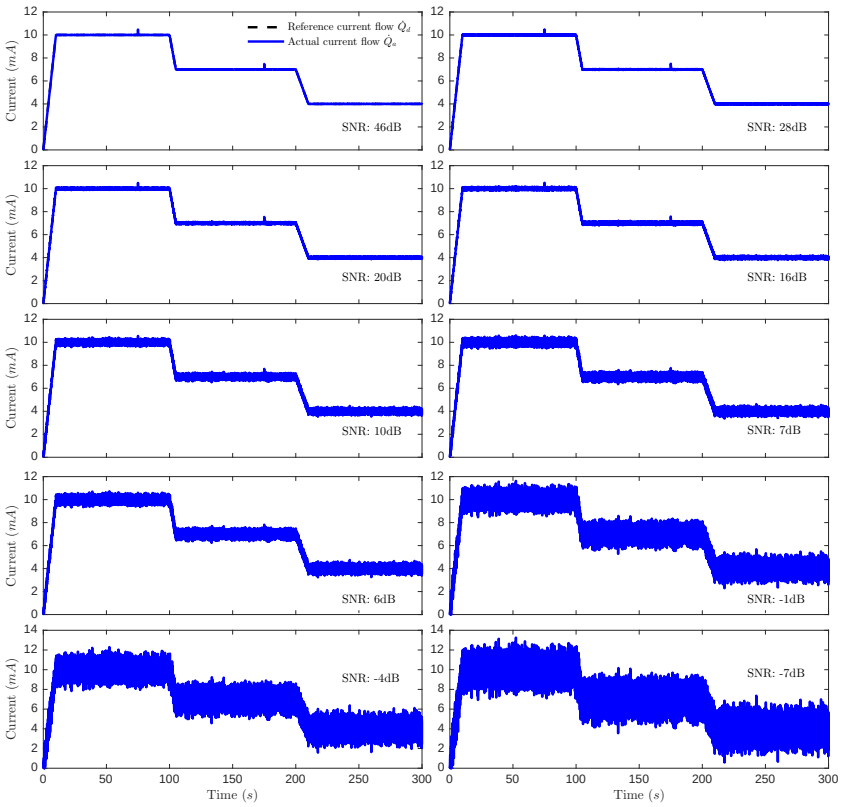

Figure 3.17: The effect of different magnitude of signal to noise ratio (SNR) during electrolysis.

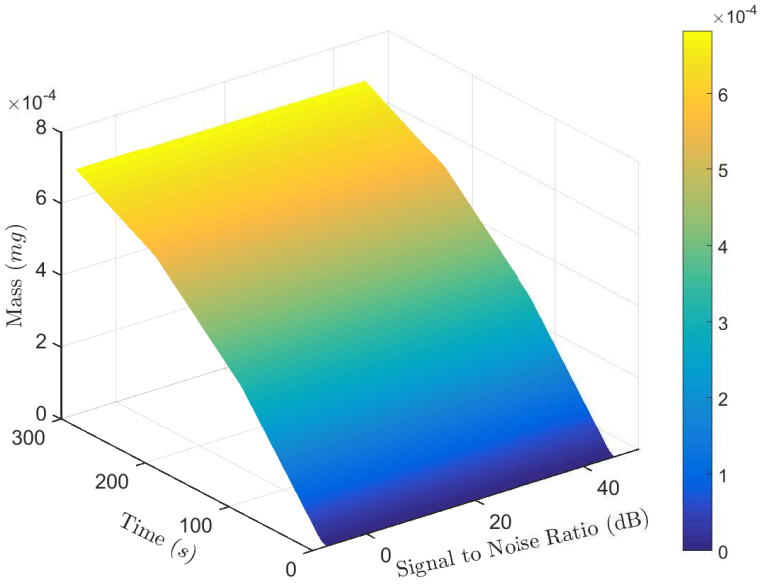

Figure 3.18: The equivalent mass deposition when exposed to different magnitude of signal to noise ratio (SNR).

in Chapter 2 with feedback control. In contrast with the passive and open-loop self-healing system in Chapter 2, the concept of active self-healing ensures that a match between user or environmental demands like the damage rate, and the healing rate is achieved. Adaptive sliding mode feedback control frameworks were designed and implemented on an electrolytic self-healing process and a piezo-electrolytic self-healing process, while taking into account the inherent dead-zone non-linearity of this self-healing mechanism. Example simulations are provided to investigate the effectiveness of active self-healing in different operating conditions. These conditions are simulated as sinusoidal inputs with constant and changing amplitudes and are representatives of operating characteristics of structures, e.g. input from rotating machinery, wind gust on a turbine, turbulence on an aircraft, waves on a ship, footfall on a bridge etc. The control simulations effectively showed that the healing rate can be regulated to match the damage rate. In practice, the performance of a typical self-healing process is affected by uncertainties. Importantly, investigations show that active self-healing process can handle some uncertainties or disturbance. A comparison with results obtained in Chapter 2 indicates that active self-healing can be effective in tackling some of the drawbacks of passive self-healing. The implemented active self-healing can benefit from an additional secondary component, that is, the inclusion of a fault diagnosis system. This is because environmental demands like damage rate are best described using a fault diagnosis system. It gives an accurate account of the damage rate and improves the reliability of the active self-healing system. Hence, the next chapter will focus on developing a fault diagnosis technique that can be used to estimate the damage rate.

Chapter 4

Crack Detection and Diagnosis

4.1 Introduction

The mathematical model formulated in Chapter 2 showed how a typical passive self-healing process is unregulated and does not guarantee a match with the damage rate during healing. In Chapter 3, an active self-healing system was formulated and simulated to demonstrate the effectiveness to matching the healing and user or environmental demands like damage rate. More so, the demonstration shows that regardless of the uncertainties and disturbances surrounding the healing process, a desired self-healing response can be achieved. While a match was achieved between damage and healing rate, the damage rate cannot be assumed. This is because damage rate is dynamic and is a function of several operational system parameters such as the atmospheric and environmental conditions. Hence, a need for a fault diagnosis technique to estimate the damage rate.

In this chapter, a novel fault diagnosis algorithm is proposed and applied to a modelled beam to estimate the crack depth and location. This takes advantage of sensor measurements to detect and quantify faults. A beam is selected to demonstrate the application of self-healing because it represents a wide range of structures such as bridges, turbine blades, airliner wings, cranes, building elements, etc. The introduction of crack causes changes in the vibration

response of the beam due to a drop in beam stiffness and increased damping. This results in changes in natural frequencies, mode shapes and curvatures. These indicators have been researched extensively along with experimental validation (Amezquita-Sanchez and Adeli, 2016; Doebling et al., 1998; Fan and Qiao, 2011; Goyal and Pabla, 2016; Hossain et al., 2016). However, changes in natural frequency may prove insufficient in detecting the actual crack depth since the changes are sensitive to environmental factors and may not be unique to a particular crack depth or location (Fan and Qiao, 2011). On the other hand, mode shape and beam curvature are less affected by the environment but the beam curvature has been observed to be more sensitive than the mode shape to damage (Dawari and Vesmawala, 2013; Fan and Qiao, 2011; Pandey et al., 1991; Wahab and De Roeck, 1999). These vibration signals have been processed with one or more of the change indicators using neural network (Hossain et al., 2016), wavelet analysis (Hou et al., 2000; Jiang et al., 2012; Loutridis et al., 2004; Robertson et al., 2003; Wang and Deng, 1999; Yan and Yam, 2002), optimization (Hoseini Vaez and Fallah, 2017; Jena and Parhi, 2015; Krawczuk, 2002; Vakil-Baghmisheh and Peimani, 2008), fuzzy logic (Nanda et al., 2015),etc., to locate and quantify the damage. Depending on the application, these techniques may come with some limitations. For example, optimisation is limited by the need for computational time and resources, neural network may suffer from over-fitting and wavelet analysis requires expertise in signal processing. Nonetheless, these techniques have successfully been implemented and investigation has shown that wavelet analysis can detect a small crack depth (Yan and Yam, 2002). This makes wavelet analysis suitable for this analysis as the crack depth decreases during healing.

The fault diagnosis algorithm in this research combines the beam curvature, proportional orthogonal decomposition, Hölder exponent and supervised regression (Kuponu et al., 2017b). The beam curvature is selected in this research because of its sensitivity to damage. Proportional orthogonal decomposition is a feature extraction technique used to separate the components of the vibration

signal that do not change from those that do and also to optimally reduce the dimension of the signal (Buljak, 2011; Chen et al., 2013). This is applied to the intact and damaged signals of the beam. The Hölder exponent is used to examine changes in the extracted features by operating on the wavelet modulus maxima of the extracted features. Finally, the crack depth is estimated using supervised regression.

The aims of this chapter are:

- To present a new crack diagnosis technique to estimate the depth and location of a crack.
- To demonstrate through simulation the effectiveness of the developed crack diagnosis technique to different beam types.

In the following, various intact and damaged beams are modelled in Section 4.2 and the diagnosis technique is presented in Section 4.3. Section 4.4 provides example simulations and discussion of the diagnosis technique while a sensitivity analysis is presented in Section 4.5. The chapter concludes with a summary in Section 4.6.

4.2 Beam Model

Beams are defined by their support, for example:

1. Fixed beam: Both ends of the beam are clamped with no form of rotation allowed as shown in Figure 4.1a.
2. Cantilever beam: Only one end of the beam is fixed as shown in Figure 4.1b.
3. Simply supported beam: Figure 4.1c shows a simply supported beam where both ends are supported with freedom to rotate.

The beams in Figure 4.1 of length L, width w and depth h can be modelled using Euler-Bernoulli beam theory (Meirovitch, 2001). From the mathematical

(a) A fixed beam.

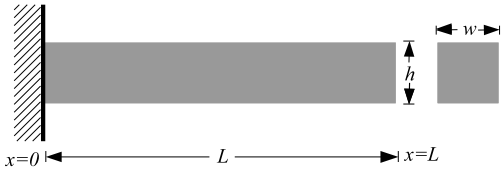

(b) A cantilever beam.

(c) A simply supported beam.

Figure 4.1: Some types of beam representing a wide range of structures.

preliminaries in Appendix C, the differential equation that governs free vibration of a beam is expressed in Equation (4.1) as (Meirovitch, 2001):

$$EI\frac{\partial^4 y(x,t)}{\partial x^4} + \rho A\frac{\partial^2 y(x,t)}{\partial t^2} = 0 \tag{4.1}$$

where $y(x,t) = \sum_{n=1}^{\infty} Y_n(x) sin\ (\omega_n t)$ is the displacement at location x, A is the cross sectional area, I is the second moment of inertia, ρ is the density and E is the Young's modulus. Y_n and ω_n are the mode shape and natural frequency in rad/seconds of the n_{th} mode respectively. From Equation (4.1), the general equation of the intact beam's modal deflection Y_n (neglecting structural damping) is given by Equation (4.2), where $\lambda_n = \sqrt[4]{\omega_n^2 \rho A L^4/EI}$ (Meirovitch, 2001).

$$Y_n(x) = \eta_1 cosh\left(\lambda_n \frac{x}{L}\right) + \eta_2 sinh\left(\lambda_n \frac{x}{L}\right) + \eta_3 cos\left(\lambda_n \frac{x}{L}\right) + \eta_4 sin\left(\lambda_n \frac{x}{L}\right) \tag{4.2}$$

4.2.1 Boundary Conditions

The boundary conditions define the type of beam structure and can be applied to evaluate the unknown constants η_{1-4} of Equation (4.2) along $x = 0$ to $x = L$ of the beam. Table 4.1 shows the boundary conditions of some beam types. In

Table 4.1: Boundary conditions of different beam types (Petyt, 2010).

Beam type	Boundary conditions	
Fixed	$Y_n(0) = Y_n^{'}(0) = 0$	$Y_n(L) = Y_n^{'}(L) = 0$
Simply supported	$Y_n(0) = Y_n^{''}(0) = 0$	$Y_n(L) = Y_n^{''}(L) = 0$
Cantilever	$Y_n(0) = Y_n^{'}(0) = 0$	$Y_n^{''}(L) = Y_n^{'''}(L) = 0$

general, a beam has no displacement ($Y_n = 0$) and rotation ($Y_n' = 0$) at the fixed end while a free end has no moment ($Y_n'' = 0$) and shear force ($Y_n''' = 0$). A simply supported beam has no displacement ($Y_n = 0$) and moment ($Y_n'' = 0$). Other beam types are a combination of any these boundary conditions.

The boundary conditions of the cantilever and the fixed beam in Table 4.1 results in Equation (4.3) - (4.4), respectively (Meirovitch, 2001; Petyt, 2010; Vakil-Baghmisheh and Peimani, 2008).

$$\begin{bmatrix} 1 & 0 & 1 & 0 \\ 0 & 1 & 0 & 1 \\ cosh(\lambda_n) & sinh(\lambda_n) & -cos(\lambda_n) & -sin(\lambda_n) \\ sinh(\lambda_n) & cosh(\lambda_n) & sin(\lambda_n) & -cos(\lambda_n) \end{bmatrix} \begin{bmatrix} \eta_1 \\ \eta_2 \\ \eta_3 \\ \eta_4 \end{bmatrix} = 0 \tag{4.3}$$

$$\begin{bmatrix} 1 & 0 & 1 & 0 \\ 0 & 1 & 0 & 1 \\ cosh(\lambda_n) & sinh(\lambda_n) & cos(\lambda_n) & sin(\lambda_n) \\ sinh(\lambda_n) & cosh(\lambda_n) & -sin(\lambda_n) & cos(\lambda_n) \end{bmatrix} \begin{bmatrix} \eta_1 \\ \eta_2 \\ \eta_3 \\ \eta_4 \end{bmatrix} = 0 \tag{4.4}$$

4.2.2 Cracked Beam

Assuming a crack of depth a in Figure 4.2 divides the beam into two sections at l_1, the modal deflection on both sides of the crack can be defined as Y_r and Y_l (right and left respectively).

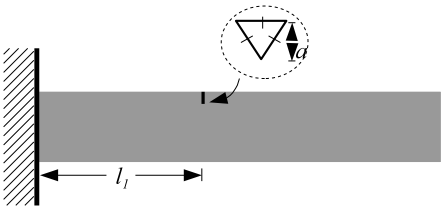

Figure 4.2: A cracked cantilever beam.

The general equations for both sections divided by the crack are represented by Equations (4.5) - (4.6):

$$\begin{aligned} Y_{r_n}(x) = \; & \alpha_1 cosh\left(\lambda_{d_n}\tfrac{x}{L}\right) + \alpha_2 sinh\left(\lambda_{d_n}\tfrac{x}{L}\right) \\ & + \alpha_3 cos\left(\lambda_{d_n}\tfrac{x}{L}\right) + \alpha_4 sin\left(\lambda_{d_n}\tfrac{x}{L}\right) \end{aligned} \tag{4.5}$$

$$\begin{aligned} Y_{l_n}(x) = \; & \beta_1 cosh\left(\lambda_{d_n}\tfrac{x}{L}\right) + \beta_2 sinh\left(\lambda_{d_n}\tfrac{x}{L}\right) \\ & + \beta_3 cos\left(\lambda_{d_n}\tfrac{x}{L}\right) + \beta_4 sin\left(\lambda_{d_n}\tfrac{x}{L}\right) \end{aligned} \tag{4.6}$$

where $\lambda_{d_n} = \sqrt[4]{\omega_{d_n}^2 \rho A L^4 / EI}$ and ω_{d_n} is the modal frequency of the damaged beam.

The crack depth a is modelled as a local stiffness Θ given by Equation (4.7) (Vakil-Baghmisheh and Peimani, 2008):

$$\Theta = \frac{EI}{6(1-v^2)h} \times \frac{1}{J(a,h)} \tag{4.7}$$

where

$$\begin{aligned} J(a,h) = \; & 1.8224\left(\frac{a}{h}\right)^2 - 3.95\left(\frac{a}{h}\right)^3 + 16.375\left(\frac{a}{h}\right)^4 \\ & - 37.226\left(\frac{a}{h}\right)^5 + 76.81\left(\frac{a}{h}\right)^6 - 126.9\left(\frac{a}{h}\right)^7 \\ & + 172\left(\frac{a}{h}\right)^8 - 143\left(\frac{a}{h}\right)^9 + 66.56\left(\frac{a}{h}\right)^{10} \end{aligned} \tag{4.8}$$

The term v is the Poisson's ratio. The crack introduces additional boundary conditions into the model at l_1 and are expressed in Equation (4.9) (Dong et al., 2004; Vakil-Baghmisheh and Peimani, 2008):

$$\begin{aligned} Y_{l_n}(l_1) &= Y_{r_n}(l_1) \\ Y''_{l_n}(l_1) &= Y''_{r_n}(l_1) \\ Y'''_{l_n}(l_1) &= Y'''_{r_n}(l_1) \\ \frac{EI}{\Theta} Y''_{l_n}(l_1) + Y'_{l_n}(l_1) &= Y'_{r_n}(l_1) \end{aligned} \tag{4.9}$$

Similarly, the unknowns α_{1-4} and β_{1-4} can be solved by applying the boundary conditions stated in Equation (4.9) and Table 4.1 to Equations (4.5) - (4.6). This results in Equations (4.10) - (4.11) for a cantilever and a fixed beam respectively.

$$\begin{bmatrix} AA & BB \\ CC & DD \\ BB & B_c \end{bmatrix} \begin{bmatrix} \alpha_c \\ \\ \beta_c \end{bmatrix} = 0 \tag{4.10}$$

$$\begin{bmatrix} AA & BB \\ CC & DD \\ BB & B_f \end{bmatrix} \begin{bmatrix} \alpha_c \\ \\ \beta_c \end{bmatrix} = 0 \tag{4.11}$$

where

$$AA = \begin{bmatrix} 1 & 0 & 1 & 0 \\ \\ 0 & 1 & 0 & 1 \end{bmatrix} \qquad BB = \begin{bmatrix} 0 & 0 & 0 & 0 \\ \\ 0 & 0 & 0 & 0 \end{bmatrix} \tag{4.12}$$

$$CC = \begin{bmatrix} z_4 & z_3 & z_2 & z_1 \\ z_4 & z_3 & -z_2 & -z_1 \\ z_3 & z_4 & z_1 & -z_2 \\ \frac{\Theta L}{EI\lambda} z_3 + z_4 & \frac{\Theta L}{EI\lambda} z_4 + z_3 & -\frac{\Theta L}{EI\lambda} z_1 - z_2 & \frac{\Theta L}{EI\lambda} z_2 - z_1 \end{bmatrix} \tag{4.13}$$

$$DD = \begin{bmatrix} -z_4 & -z_3 & -z_2 & -z_1 \\ -z_4 & -z_3 & z_2 & z_1 \\ -z_3 & -z_4 & -z_1 & z_2 \\ -\frac{\Theta L}{EI\lambda_{d_n}} z_3 & -\frac{\Theta L}{EI\lambda_{d_n}} z_4 & \frac{\Theta L}{EI\lambda_{d_n}} z_1 & -\frac{\Theta L}{EI\lambda_{d_n}} z_2 \end{bmatrix} \tag{4.14}$$

$$B_c = \begin{bmatrix} z_5 & z_6 & -z_7 & -z_8 \\ z_6 & z_5 & z_8 & -z_7 \end{bmatrix} \quad B_f = \begin{bmatrix} z_5 & z_6 & z_7 & z_8 \\ z_6 & z_5 & -z_8 & z_7 \end{bmatrix} \tag{4.15}$$

$$\alpha_c = \begin{bmatrix} \alpha_1 \\ \alpha_2 \\ \alpha_3 \\ \alpha_4 \end{bmatrix} \quad \beta_c = \begin{bmatrix} \beta_1 \\ \beta_2 \\ \beta_3 \\ \beta_4 \end{bmatrix} \tag{4.16}$$

where $z_1 = sin\left(\lambda_{d_n} \frac{l_1}{L}\right)$, $z_2 = cos\left(\lambda_{d_n} \frac{l_1}{L}\right)$, $z_3 = sinh\left(\lambda_{d_n} \frac{l_1}{L}\right)$, $z_4 = cosh\left(\lambda_{d_n} \frac{l_1}{L}\right)$, $z_5 = cosh(\lambda_{d_n})$, $z_6 = sinh(\lambda_{d_n})$, $z_7 = cos(\lambda_{d_n})$, $z_8 = sin(\lambda_{d_n})$.

4.3 Detection and Diagnosis System

The practical illustration of the proposed fault diagnosis involves data acquisition from sensors placed in strategic places on the beam. These sensor measurements go through a data analysis process of the diagnosis system as shown in Figure 4.3.

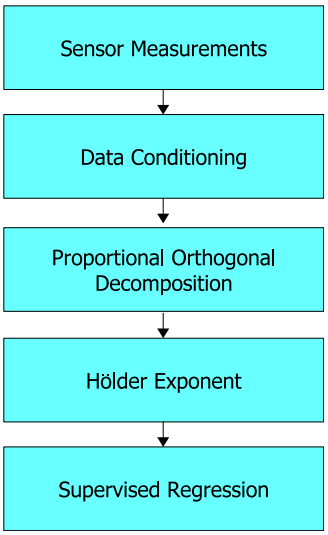

Figure 4.3: Data analysis process of the proposed diagnosis system

For example, sensor measurements from accelerometers capture the acceleration of the beam. The data conditioning is a two stage process that involves integrating the data twice to extract the beam deflection and converting the deflections into curvatures. The beam curvature captures information that is sensitive to damage and a full description is detailed in Subsection 4.3.1. Further analysis of the curvature is carried out using the proportional orthogonal decomposition to separate components of the signal that do not change from those that do. The components of the signal that change are particularly useful for detection and diagnosis. A baseline of the extracted changing component of a healthy beam is compared with that of a faulty beam. The result of the comparison provides information on location of the crack and is further analysed by the Hölder exponent. The Hölder exponent provides a measure to quantify the extent of the crack depth my operating on the wavelet transformed

of the resulting comparison stated above. The final stage of the data analysis involves a supervised regression to estimate the actual crack depth based on the Hölder exponent. A full description on the data analysis process is detailed in Subsection 4.3.1 - Subsection 4.3.4.

4.3.1 Radius of Curvature

As stated earlier, the radius of curvature is more sensitive than its mode shape to damage. The curvature κ is expressed in Equation (4.17) (Dawari and Vesmawala, 2013; Fan and Qiao, 2011; Pandey et al., 1991; Wahab and De Roeck, 1999):

$$\kappa(x) = \frac{M(x)}{EI} \tag{4.17}$$

with $M(x)$ and the product of E and I representing the bending moment and flexural stiffness of the beam respectively. A reduced flexural stiffness introduced by damage at location x results in an increased curvature, which is used as an indicator of abnormality. To transform the deflection into the radius of curvature, Equation (4.17) can be approximated using the central difference in Equation (4.18) at the i_{th} node of q number of elements, with an element length l (Dawari and Vesmawala, 2013; Fan and Qiao, 2011; Pandey et al., 1991; Wahab and De Roeck, 1999):

$$\kappa(x_i) \approx Y_i'' = \frac{Y_{i+1} - 2Y_i + Y_{i-1}}{l^2} \tag{4.18}$$

For a particular mode shape, the approximate radius of curvature is Equation (4.19):

$$Y_n^{rad} = \begin{bmatrix} Y_{n_2}'' & Y_{n_3}'' & \dots & \dots & Y_{n_{q-1}}'' \end{bmatrix} \tag{4.19}$$

The curvature of r number of mode shapes is combined to form a matrix Y_{rad} in Equation (4.20)):

$$Y_{rad} = \begin{bmatrix} Y_1^{rad} \\ \vdots \\ Y_r^{rad} \end{bmatrix}_{r\times(q-2)} \tag{4.20}$$

4.3.2 Proportional Orthogonal Decomposition (POD)

Unique features that are particularly important for detection and diagnosis can then be extracted from Equation (4.20) using a proper orthogonal decomposition (POD). This is employed to separate components of the signal Y_{rad} that do not change from those that do. For the purpose of diagnosis, this research is interested in the components of the signal Y_{rad} that change. A POD can be used to optimally reduce and approximate a signal and is defined as the sum of linear weightings expressed in Equation (4.21) (Buljak, 2011; Chen et al., 2013):

$$Y_{rad} \approx \sum_{k=1}^{r} c_k \varphi_k \tag{4.21}$$

The term φ is the POD mode (spatial basis function) that does not change, while the unknown amplitude c_k represents the varying components of the signal used for detection and diagnosis. To solve for c_k, the basis functions φ_k must be orthonormal (Equation (4.22)) and satisfy Equation (4.23):

$$\int \varphi_i \varphi_j dx == \begin{cases} 1 & \text{for } i = j \\ 0 & \text{for } i \neq j \end{cases} \tag{4.22}$$

$$\min \left(||Y_{rad} - \sum_{k=1}^{r} c_k \varphi_k||^2 \right) \tag{4.23}$$

The algorithm to determine the POD is:

1. Compute the correlation matrix of signal Y_{rad} given as $C = Y_{rad} Y_{rad}^T$.

2. Solve the eigenvalue problem $C\varphi_k = \lambda_k \varphi_k$ to find the eigenvectors, which correspond to the spatial basic functions.

3. Solve for the unknown amplitudes $c_k = \varphi_k^T Y_{rad}$.

The algorithm is applied to evaluate the unknown amplitudes for both undamaged (c^u) and damaged (c^d) systems, based on the undamaged signal (Y_{rad}^u) and damaged signal (Y_{rad}^d). The undamaged amplitude c^u remains fixed, while the damaged amplitude c^d changes as the fault progresses. The algorithm is applied in real time in this research and a monitoring index indicating the current state of the system is evaluated using Equations (4.24) - (4.25), where δ is the margin within which the beam remains healthy and is selected by investigation:

$$\tau(t) = \left| ||c^u|| - ||c^d(t)|| \right| \tag{4.24}$$

$$index(t) = \begin{cases} 0, & \text{if } \tau \leq \delta \quad \text{(no fault)} \\ 1, & \text{otherwise (fault detected)} \end{cases} \tag{4.25}$$

The error $E(x,t)$, defined in Equation (4.26), can be used to determine the location l_{est} and crack depth a_{est} at every time instant.

$$E(x,t) = |c^u(x) - c^d(x,t)| \tag{4.26}$$

4.3.3 Hölder Exponent

By transforming the error signal further using wavelet transform, the Hölder exponent can be evaluated. The Hölder exponent examines changes in signal by operating on the modulus maxima of the wavelet transform (Angrisani et al., 1999; Douka et al., 2003; Loutridis et al., 2004; Robertson and Farrar, 2003). The wavelet transform defined by Equation (4.27) is used to transform the error signal $E(x,t)$ into its equivalent wavelet function W_f using a mother wavelet Ψ over a scaling parameter s_w and translational parameter b (Isermann, 2006; Polikar, 1996).

$$W_f(s_w, b) = \frac{1}{\sqrt{s_w}} \int_{-\infty}^{+\infty} E(x) \Psi^* \left(\frac{x-b}{s_w} \right) dx \tag{4.27}$$

The scaling and translational parameters indicate the scale of the crack and the point of interest on the beam. Examples of mother wavelets are Morlet, Haar, Mexican hat, Daubechie, Symlets etc. (Rao, 1998). In this research, the Morlet wavelet is used because it has similar components with faulty vibration signals, thus, producing a better correlation with the vibration signals and a larger wavelet coefficient (Rao, 1998; Zheng et al., 2002). This is given as Equation (4.28) and shown in Figure 4.4.

$$\psi(x) = \pi^{-1/4} e^{\frac{-x^2}{2}} cos(5x) \tag{4.28}$$

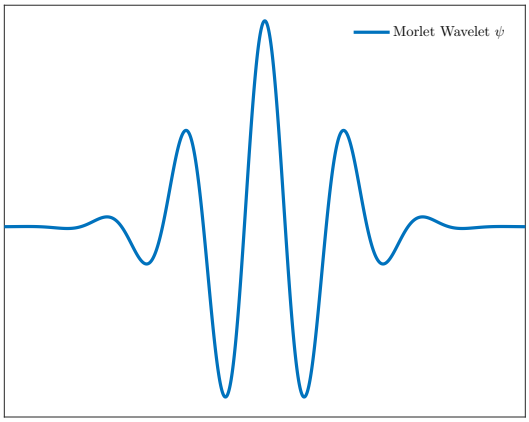

Figure 4.4: A Morlet mother wavelet used to transform a signal into its equivalent wavelet function.

The Hölder exponent defines a signal $f(x)$ approximated by a polynomial $Z(x)$ at a local point x_0, such that the coefficient N and Hölder exponent α exist (Equation (4.29)). This is written in terms of the modulus maxima of the wavelet transform in Equation (4.30) (Angrisani et al., 1999; Douka et al., 2003; Loutridis et al., 2004; Robertson and Farrar, 2003).

$$|f(x) - Z(x)| \leq N|x - x_0|^{\alpha} \tag{4.29}$$

$$|W_f(s_w, b)| \leq N s_w^{\alpha} \tag{4.30}$$

The coefficient N and α can be evaluated from the plot of the logarithm of Equation (4.30). Different crack depths at the same location result in the same Hölder exponent α but different coefficients N. The coefficient N therefore represents the measure of crack depth at a particular location. This is extended in this research to capture the normalised measure of the crack depth at different locations by introducing the crack location, $\frac{N}{l_{est}^{p}}$; where p is a positive term.

4.3.4 Supervised Regression

While the formulation in Subsection 4.3.3 gives the measure of the crack depth at different locations, the actual crack depth remains unknown. To estimate the crack depth, a supervised regression algorithm is implemented (Equation (4.31)) with weights ζ obtained from prior knowledge of crack depths at different locations.

$$\frac{a_{est}}{l_{est}^{p}} = [X_c][\zeta]^T \tag{4.31}$$

$$X_c = \begin{bmatrix} x_c & x_c^2 & \dots & \dots & x_c^r \end{bmatrix}_{1\times rj} \tag{4.32}$$

$$x_c = \begin{bmatrix} \left(\frac{N}{l_{est}^{p}}\right)_{normalised} & l_{est} & \Delta f \end{bmatrix}_{1\times j} \tag{4.33}$$

$$\Delta f = \begin{bmatrix} f_{u_1} - f_{d_1} \\ \vdots \\ f_{u_n} - f_{d_n} \end{bmatrix}_{1\times n}^{T} \tag{4.34}$$

$$\zeta = \begin{bmatrix} \zeta_1 & \zeta_2 & \dots & \dots & \zeta_{rj} \end{bmatrix}_{1\times rj} \tag{4.35}$$

The order r of the polynomial used to estimate the crack depth is selected using k-fold cross validation (Pereira et al., 2009). x_c^r defines the r number of times an element wise multiplication of x_c is performed. Equation (4.36) is combined with changes in modal frequencies Δf of all modes and the crack location to give the term x_c in Equation (4.33).

$$\left(\frac{N}{l_{est}^{p}}\right)_{normalised} = \frac{\frac{N}{l_{est}^{p}} - min\left(\frac{N}{l_{est}^{p}}\right)}{max\left(\frac{N}{l_{est}^{p}}\right) - min\left(\frac{N}{l_{est}^{p}}\right)} \tag{4.36}$$

The frequency of the intact beam is represented by f_{u_i} for any i_{th} mode while f_{d_i} represents the frequency of a cracked beam at the i_{th} mode. n is the total number of modes and $j = 2 + n$. The minimum and maximum values of $\frac{N}{l_{est}^{p}}$ are defined in this research over all possible values between the crack depth of 1 mm and 3 mm.

4.4 Numerical Results and Discussion

In this section, the effectiveness of the proposed diagnosis technique is illustrated by simulation in Matlab. An aluminium cantilever beam of dimensions 820 mm by 20 mm by 10 mm is modelled using a finite element model with 24 elements. The beam's mechanical properties include Young's modulus of 70 GPA, density of 2700 kg/m^3 and Poisson ratio of 0.3 (Vakil-Baghmisheh and Peimani, 2008). The parameters are selected for comparison with a genetic algorithm for crack diagnosis proposed by Vakil-Baghmisheh and Peimani (2008).

The deflections of four modes of the intact and cracked beam with cracks of 1 mm, 2 mm and 3 mm at location 196.8 mm are shown in Figure 4.5a-d. The results do not indicate the presence of cracks. Unlike the deflections, the radius of curvatures in Figure 4.5e-h give a significant distinction between the intact and cracked beam. This justifies the selection of radius of curvature for this analysis. Other mode shapes and curvatures at different crack locations can be found in Figures D.1 - D.6 of Appendix D. The cracked cantilever beam also results in changes in modal frequencies as shown by the red lines of Figure 4.6. Other modal frequency changes at different crack locations and depths are also shown in Figure 4.6. The figure indicates a decremental trend in modal frequencies as the crack depth increases. Figure 4.7 shows that the maximum peaks of the error between the unique features extracted from the

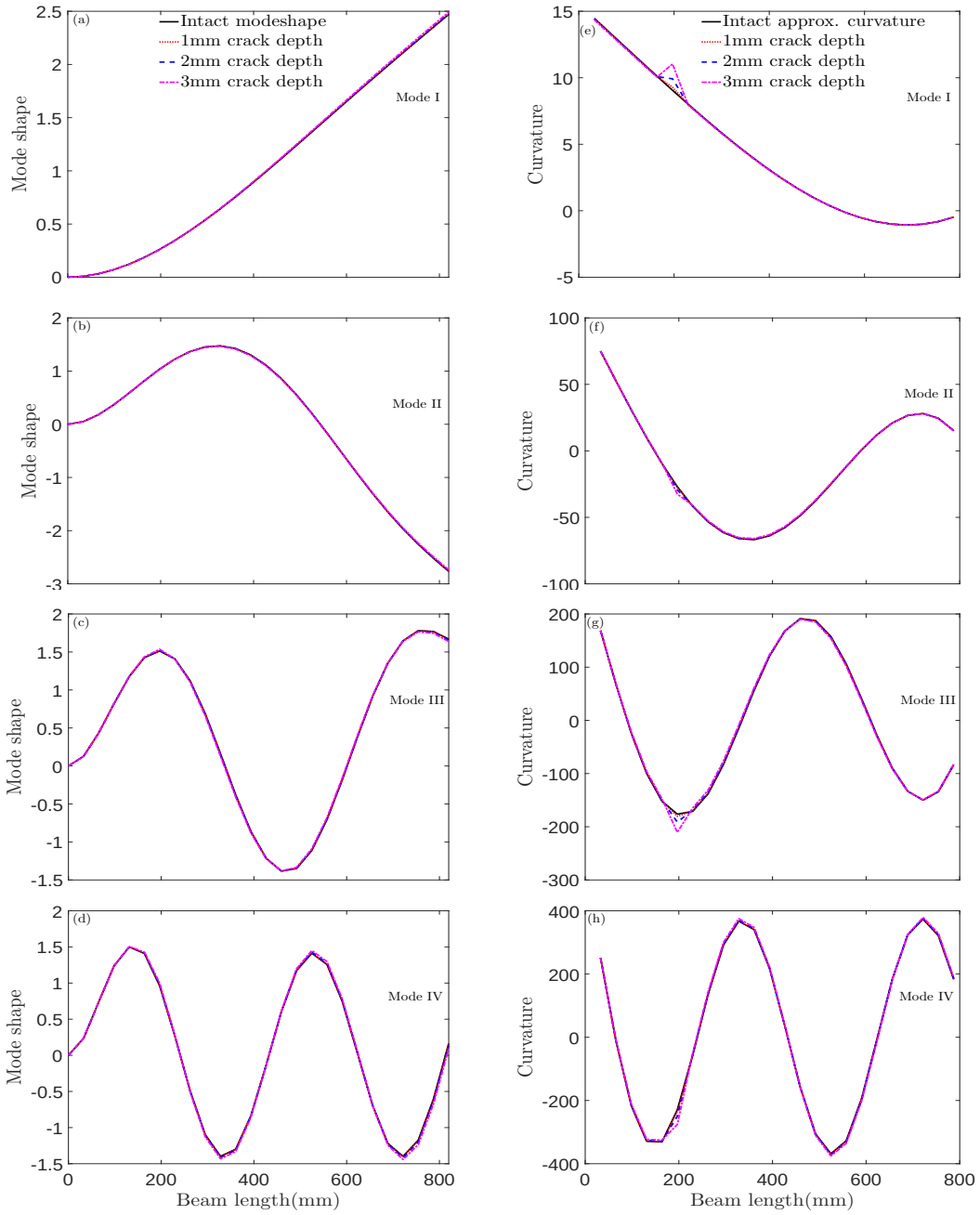

Figure 4.5: Mode shapes (a-d) and curvatures (e-h) of the first four modes of an intact and damaged cantilever beam of different crack depths located at 196.8mm.

intact and cracked radius of curvatures by the POD algorithm indicate the crack locations. The error is transformed into wavelets and used to determine the Hölder exponent α and coefficient N by taking the logarithm plot of Equation (4.30); this is captured in Figure 4.8. At each crack location, the

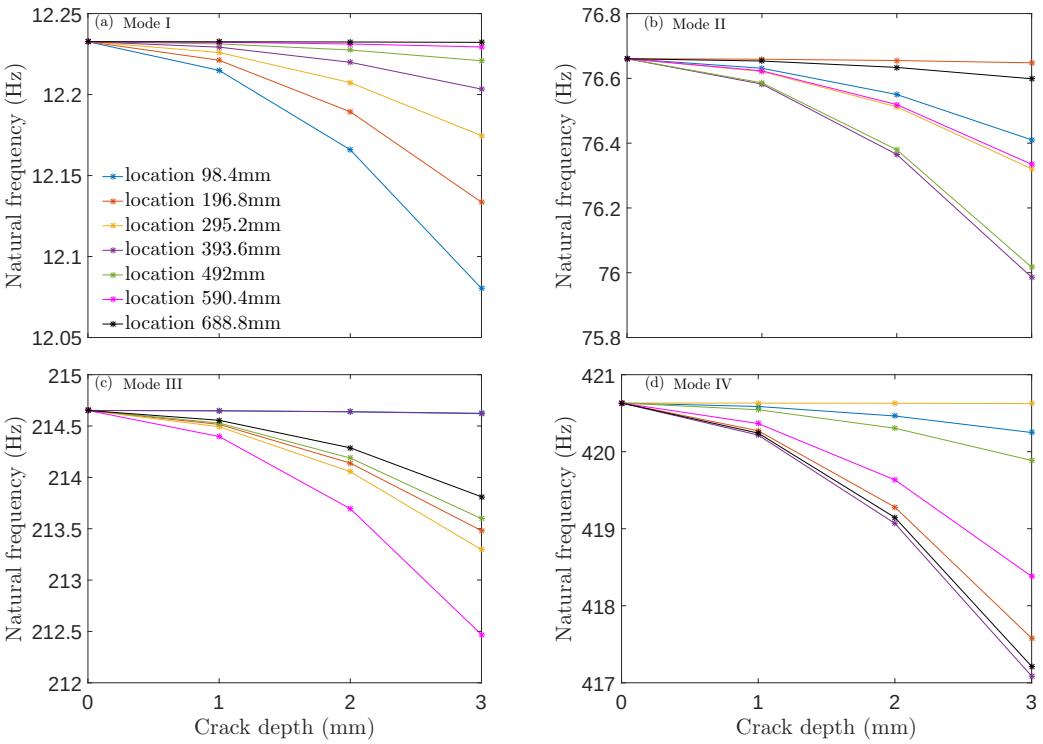

Figure 4.6: Natural frequency of the first four modes of an intact and a damaged cantilever beam of different crack depths at different crack locations.

logarithm plots of Equation (4.30) for all crack depths between $1-3\ mm$ are parallel but have different vertical axis intercepts. Parallel plots are indicative of the same gradient and suggest that the different cracks occur at the same location; the gradient is referred to as the Hölder exponent α. Similarly, each value of the vertical axis intercepts represents the coefficient N for the different crack depths at a particular crack location. Thus, the use of $\frac{N}{l_{est}^{p}}$ for regression captures a global coefficient at different crack location.

To avoid under and over fitting of the crack depth estimation, a cross-validation was carried out to select the appropriate order for the polynomial of Equation (4.31). Figure 4.9 shows the normalised root mean square error (NRMSE) of the training and testing set to different orders of polynomials. An order between 8 and 12 can be selected but this research uses the order with the minimum NRMSE of the testing set as the preferred order for estimation, that is, $r = 12$ and the corresponding weightings are found in Parameter (D.1)

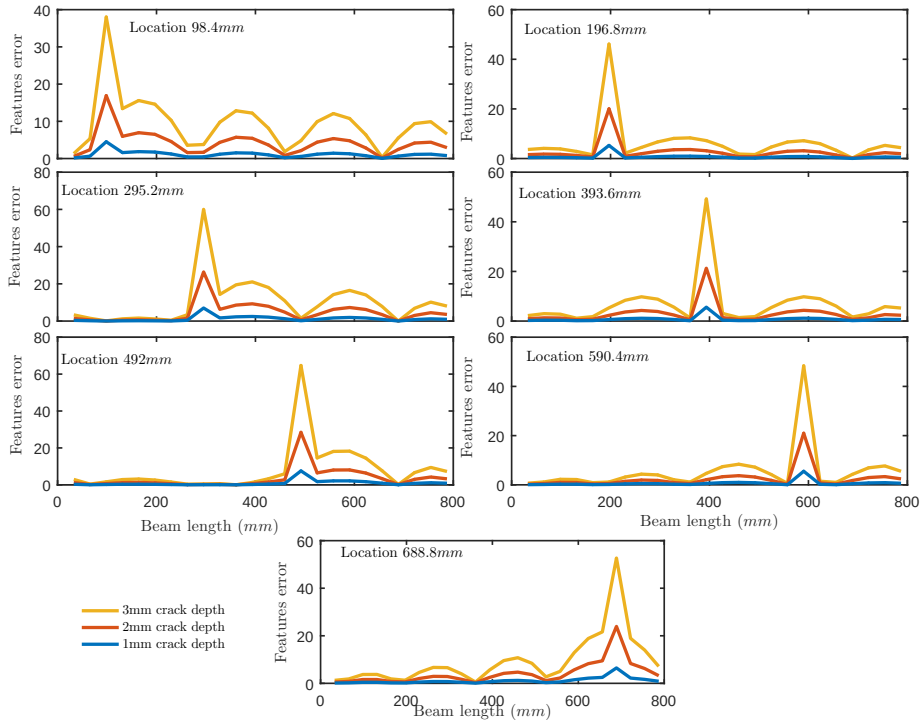

Figure 4.7: Difference between the unique features extracted by POD from an intact and the cracked beam curvatures of all crack depths at different locations.

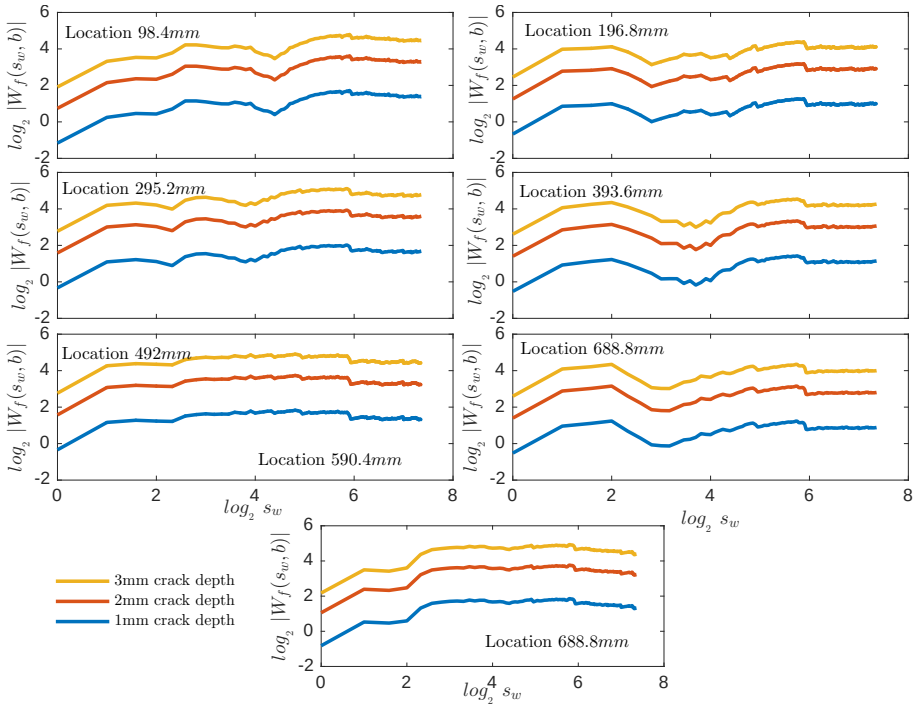

Figure 4.8: Logarithm plot of the scale and Wavelet maxima of different crack depths at the same location.

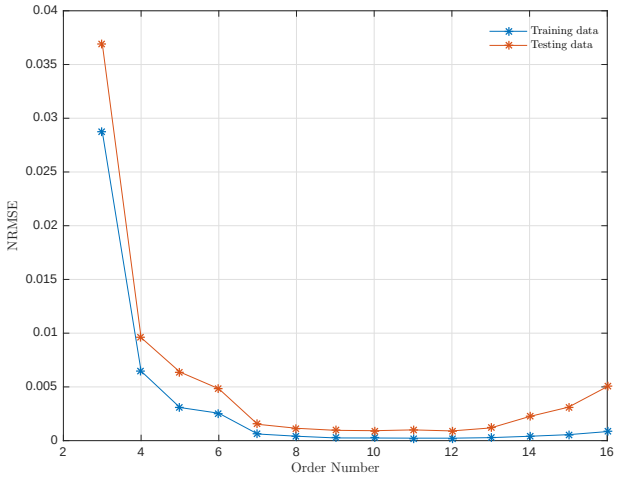

Figure 4.9: Cross-validation: The normalised root mean square (NRMSE) of different polynomial order used to select the order number. This step avoids under and over fitting.

of Appendix D. The choice of order is in accordance with the cross validation method in literature (Pereira et al., 2009). Other regression parameters used are also in Parameter (D.2) of Appendix D. The results of estimated crack depths and locations are shown in Figure 4.10a and Table 4.2. The algorithm detects the crack location and gives a maximum deviation of -1.83% from the actual crack depth. Further, Table 4.2 also shows a comparison of the proposed crack diagnosis with a genetic algorithm used by Vakil-Baghmisheh and Peimani (2008); the proposed crack diagnosis in this research resulted in a better estimation of the crack depths and locations. The proposed crack diagnosis was also applied to a fixed beam using the same beam parameters. A maximum deviation of 2.18% from the actual crack depth was recorded as shown in Table 4.3 and Figure 4.10b. Full analysis and results are shown in Appendix D.

4.5 Sensitivity Analysis

Measurements are sometimes corrupted by sensor noise or disturbances and could potentially reduce the reliability of fault diagnosis. Hence, the sensitivity

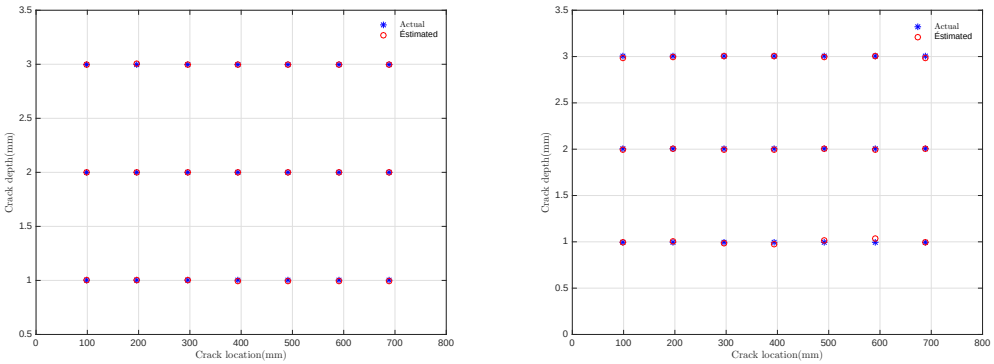

(a) **(b)**

Figure 4.10: (a) Outcome of the fault detection and diagnosis for crack depths at different locations of the: (a) Cantilever beam (b) Fixed beam

Table 4.2: Proposed crack diagnosis applied (highlighted in green) and compared with genetic algorithm (GE) results obtained in Table 5 (Vakil-Baghmisheh and Peimani, 2008) using the same cantilever beam parameters.

Crack location (mm)					Crack depth (mm)				
Actual	Estimated	Error(%)	Estimated (GE)	Error(%) (GE)	Actual	Estimated	Error(%)	Estimated (GE)	Error(%) (GE)
98.40	98.40	0.00	99.12	0.73	1.00	1.00	-0.07	0.98	-2.00
98.40	98.40	0.00	97.74	-0.67	2.00	2.00	-0.05	2.01	0.45
98.40	98.40	0.00	99.93	1.55	3.00	3.00	0.01	2.97	-0.93
196.80	196.80	0.00	193.80	-1.53	1.00	1.00	-0.27	0.97	-2.60
196.80	196.80	0.00	194.75	-1.04	2.00	2.00	-0.02	1.99	-0.55
196.80	196.80	0.00	198.52	0.88	3.00	3.00	-0.14	3.02	0.70
295.20	295.20	0.00	298.56	1.14	1.00	1.00	0.03	1.02	2.10
295.20	295.20	0.00	289.79	-1.83	2.00	2.00	0.00	1.98	-1.25
295.20	295.20	0.00	294.13	-0.36	3.00	3.00	0.01	2.98	-0.77
393.60	393.60	0.00	400.74	1.81	1.00	1.00	0.34	0.99	-1.20
393.60	393.60	0.00	394.99	0.35	2.00	2.00	0.01	1.99	-0.45
393.60	393.60	0.00	395.08	0.38	3.00	3.00	0.00	2.99	-0.50
492.00	492.00	0.00	489.62	-0.48	1.00	1.00	0.22	0.99	-0.70
492.00	492.00	0.00	492.16	0.03	2.00	2.00	-0.06	1.97	-1.55
492.00	492.00	0.00	492.41	0.08	3.00	3.00	-0.02	2.98	-0.53
590.40	590.40	0.00	589.42	-0.17	1.00	0.99	0.74	0.99	-1.00
590.40	590.40	0.00	590.48	0.01	2.00	2.00	0.00	2.00	0.10
590.40	590.40	0.00	588.10	-0.39	3.00	3.00	0.00	3.02	0.80
688.80	688.80	0.00	681.99	-0.99	1.00	1.00	0.42	0.98	-1.90
688.80	688.80	0.00	692.98	0.61	2.00	2.00	0.02	2.04	2.00
688.80	688.80	0.00	686.83	-0.29	3.00	3.00	-0.01	2.96	-1.27

of the proposed fault diagnosis to uncertainties is analysed. This is achieved by corrupting the beam deflections Y_n with sensor noise such that Y_n^* is the corrupted modal deflection and w is a white Gaussian noise drawn from a normal distribution with zero mean and variance, that is, σ^2 ($w(t) \sim \mathcal{N}(0, \sigma^2)$).

Table 4.3: Crack depth outcome of the FDD at different locations and the corresponding modal frequencies of a fixed beam

Crack location (mm)		Crack depth (mm)			Frequency (Hz)		
Actual	*Estimated*	*Actual*	*Estimated*	*%Error*	f_1	f_2	f_3
98.40	98.40	1.00	1.00	0.20	77.81	214.56	420.59
98.40	98.40	2.00	2.00	0.15	77.72	214.56	420.47
98.40	98.40	3.00	2.99	0.35	77.57	214.54	420.25
196.80	196.80	1.00	1.00	-0.48	77.84	214.43	420.28
196.80	196.80	2.00	2.00	-0.17	77.84	214.05	419.29
196.80	196.80	3.00	3.00	0.05	77.83	213.38	417.59
295.20	295.20	1.00	0.99	1.34	77.81	214.40	420.64
295.20	295.20	2.00	1.99	0.34	77.72	213.96	420.63
295.20	295.20	3.00	3.02	-0.01	77.57	213.18	420.63
393.60	393.60	1.00	0.98	2.18	77.78	214.56	420.22
393.60	393.60	2.00	2.00	0.04	77.62	214.55	419.06
393.60	393.60	3.00	3.00	-0.02	77.33	214.52	417.06
492.00	492.00	1.00	1.02	-1.75	77.80	214.46	420.54
492.00	492.00	2.00	2.01	-0.44	77.67	214.18	420.28
492.00	492.00	3.00	3.00	0.06	77.46	213.68	419.83
590.40	590.40	1.00	1.04	-3.73	77.83	214.38	420.41
590.40	590.40	2.00	2.00	0.06	77.81	213.87	419.80
590.40	590.40	3.00	3.00	-0.01	77.78	212.98	418.74
688.80	688.80	1.00	0.99	1.01	77.83	214.55	420.42
688.80	688.80	2.00	2.01	-0.38	77.80	214.51	419.82
688.80	688.80	3.00	2.98	0.51	77.74	214.44	418.77

This is expressed in Equation (4.37):

$$Y_n^* = Y_n + w(0, \sigma^2) \tag{4.37}$$

Analyses of the proposed fault diagnosis to corrupt modal deflections are shown Figure 4.11 and Table 4.4. The noisy measurements are defined by their deviations from the uncorrupted measurements. Figures 4.11a-c highlight the estimated cracks of a cantilever beam at location 196.8 mm. The actual crack depths are shown in green lines of Figures 4.11a-c, while the upper and lower bound are represented by red lines (in Figures 4.11a-c) depicting a 10% error bound. Result shows that at higher crack depths, the estimated crack depths fall within the 10% error bound, while the 1 mm crack depth is more sensitive as the deviation is increased. Within the considered deviation, the estimated crack location is 196.8 mm. Further investigation at different crack locations was carried out and the results are shown in Table 4.4. Within a standard deviation of [0.0001 0.002], the result confirms that the proposed

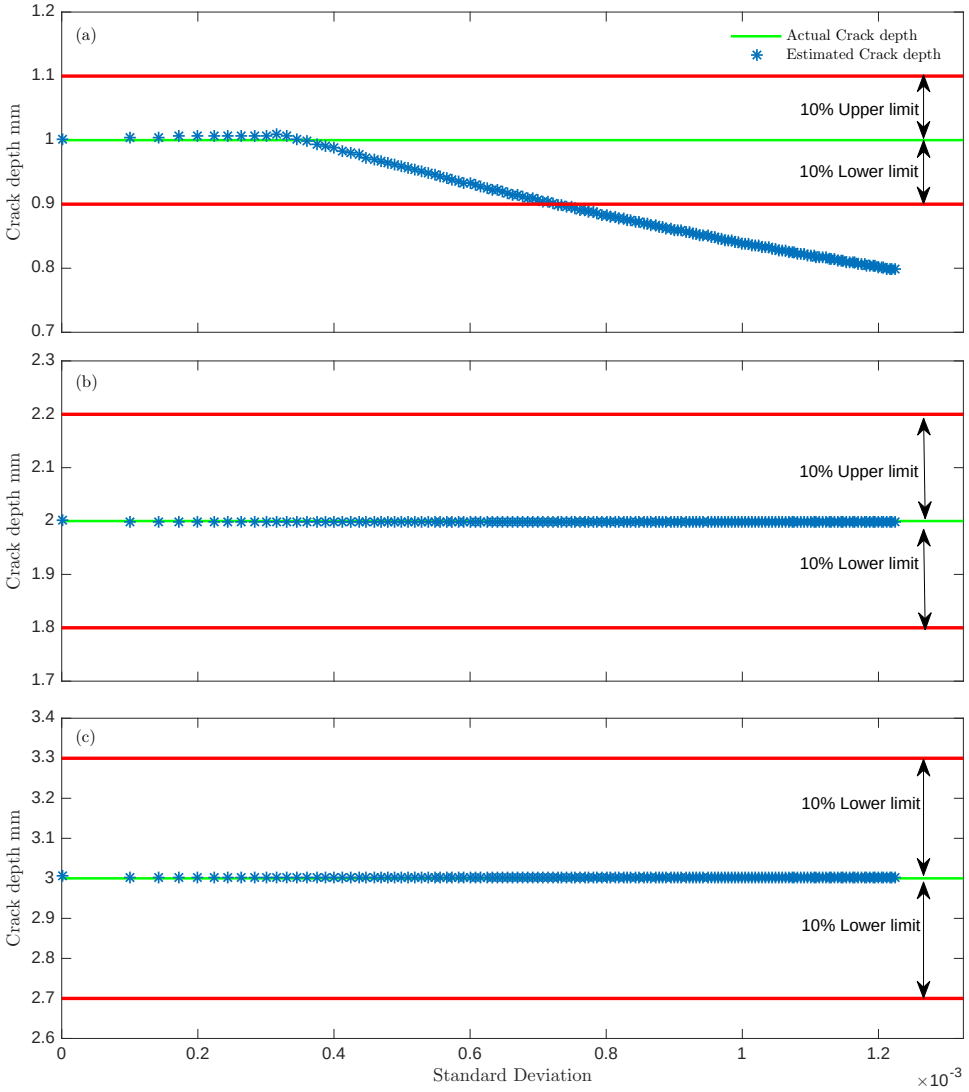

Figure 4.11: Sensitivity analysis of the proposed diagnosis techniques to uncertainties at a crack location 196.8 mm**.** (a) Analysis at a crack depth of 1 mm. SD represents the standard deviation of the corrupt signal. (b) Analysis at a crack depth of 2 mm. (c) Analysis at a crack depth of 3 mm.

fault diagnosis is not sensitive to corrupt sensor measurements at higher crack depths but the effect of sensor noise and uncertainties at lower crack depth (that is, 1 mm) is pronounce. Beyond a standard deviation of 0.0002, estimates of a 1 mm crack depth falls outside the 10% error bound.

Table 4.4: Crack depth outcome of the FDD at different locations and the corresponding modal frequencies of a fixed beam

Actual location (mm)	Actual depth (mm)	Estimation depth error %						
		$SD = 0.0001$	$SD = 0.0002$	$SD = 0.0004$	$SD = 0.0007$	$SD = 0.0009$	$SD = 0.001$	$SD = 0.002$
98.40	1.00	5.43	9.83	17.86	28.01	33.61	36.07	50.44
98.40	2.00	-0.15	-0.40	-0.79	-1.55	-2.15	-2.47	-6.44
98.40	3.00	-0.26	-0.53	-1.80	-2.78	-3.45	-3.78	-7.11
196.80	1.00	-0.44	-0.62	1.31	9.34	13.96	16.05	29.74
196.80	2.00	0.00	0.02	0.05	0.09	0.11	0.12	-2.67
196.80	3.00	-0.13	-0.12	-0.10	-0.08	-0.07	-0.06	-0.07
295.20	1.00	-0.04	-0.06	-0.09	1.56	1.91	0.82	12.29
295.20	2.00	0.01	0.02	0.05	0.10	-0.10	-0.25	1.06
295.20	3.00	0.01	0.02	0.03	0.07	0.10	0.11	0.07
393.60	1.00	0.88	-1.42	-3.94	-9.97	-14.36	-16.63	14.00
393.60	2.00	-0.24	-0.51	-0.13	0.79	1.01	1.12	2.97
393.60	3.00	-0.18	-0.37	-0.74	-0.61	-0.11	0.14	1.54
492.00	1.00	-0.82	-1.89	-9.18	-17.22	-17.28	-17.07	16.77
492.00	2.00	0.11	0.28	0.61	1.12	1.45	1.59	8.09
492.00	3.00	0.09	0.19	0.40	0.70	0.90	1.00	2.01
590.40	1.00	1.93	3.07	8.07	14.13	16.66	17.62	24.72
590.40	2.00	-0.16	-0.32	-0.64	-1.37	-1.72	-1.90	-6.88
590.40	3.00	-0.11	-0.22	-0.45	-0.91	-1.34	-1.55	-3.43
688.80	1.00	1.32	2.66	5.41	9.26	11.66	12.81	30.02
688.80	2.00	-0.05	-0.11	-0.25	-0.56	-0.80	-0.92	-2.19
688.80	3.00	-0.08	-0.15	-0.29	-0.49	-0.62	0.69	-1.63

SD: Standard deviation

4.6 Summary

This chapter detailed a novel crack diagnosis algorithm for a beam structure. The diagnosis algorithm combines the beam curvature, proportional orthogonal decomposition (POD), Hölder exponent and supervised regression. The intact and damaged state of two beam types namely: cantilever and fixed beam, were modelled and passed through the proposed diagnostic technique to locate and quantify the extent of the crack. First, the mode shapes of the beam were transformed into curvatures using the central difference. The beam curvature of different modes were combined and passed through the POD for features extraction. Changes between the intact and damaged beam features were examined using the Hölder exponent. The Hölder exponent operates on the equivalent wavelet modulus maxima of the changes. Finally, the crack depth was estimated using a supervised regression. Simulation results presented for crack depths between 1 mm and 3 mm at different locations showed that the proposed crack diagnosis is effective at locating and quantifying the extent of crack. The algorithm accurately detected the crack locations while the mean and standard deviation of all the deviations from the actual crack depths of the

cantilever beam are 0.06 and 0.22 respectively. For the fixed beam, the mean and standard deviation of all the deviations from the actual crack depths are -0.03 and 1.13 respectively. Further, a comparison with a genetic algorithm used by Vakil-Baghmisheh and Peimani (2008) indicated that the proposed crack diagnosis in this research performed better at estimating the crack depth and location. Sensitivity analysis was carried out to investigate the effect of sensor noise on the proposed diagnosis technique. The results show that the proposed technique is less sensitive to noise at higher crack depth but at 1 mm crack depth, the technique is sensitive as the deviation increases beyond 0.0002.

Importantly, the diagnosis provides an approach to estimate the damage rate used by the adaptive sliding mode controller to regulate the healing rate in the next chapter.

Chapter 5

Integrated Sensing, Diagnosis and Active Self-healing

5.1 Introduction

The mathematical model formulated in Chapter 2 showed how a typical passive self-healing process is unregulated and does not guarantee a match with the damage rate during healing. In Chapter 3, an active self-healing system was formulated and simulated to demonstrate the effectiveness of a regulated self-healing process to matching the healing and the user or environmental demands such as the damage rate. Chapter 4 presented a novel crack diagnosis for beam structures. This essentially forms the basis for the formulation of the estimated damage rate used by the control algorithm as a reference model in this chapter.

In this chapter, the active self-healing is integrated with fault diagnosis. Importantly, the combined systems demonstrate the concept of a unified sensing, diagnosis and active self-healing system shown in Figure 5.1. The integrated system ensures a regulated healing process that will guarantee a match between the estimated damage rate from diagnosis and the actual healing rate during self-healing. Also for the chosen self-healing system (piezo-electrolytic self-healing), deterring factors such as dead-zone non-linearity, disturbances, unaccounted

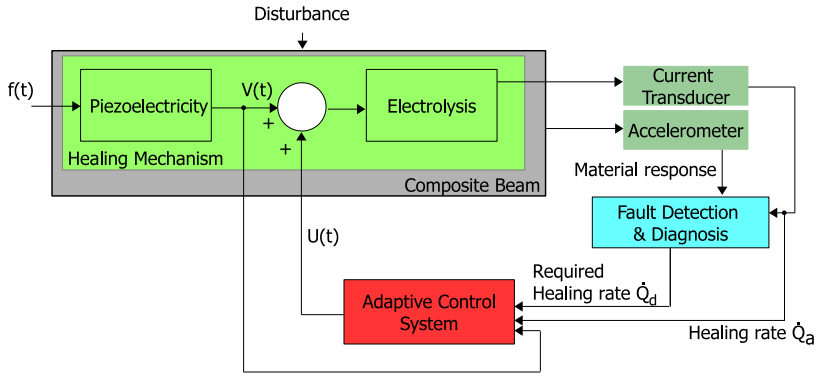

Figure 5.1: Application of the proposed unified sensing, diagnosis and active self-healing system.

uncertainties, etc. that may have adverse effect on the performance of self-healing are accommodated to ensure an effective self-healing process.

The chapter presents:

- A unified sensing, diagnosis and active self-healing system as an alternative to the passive self-healing system.
- A demonstration of the effectiveness of the proposed framework through simulation.

In the following (Kuponu et al., 2017b), the practical realisation and mathematical formulation of the proposed work, i.e. a unified sensing, diagnosis and active self-healing system, will be presented in Section 5.2 and Section 5.3 respectively. This will be followed by example simulations in Section 5.4 to demonstrate the proposed integrated system. A comparison with the equivalent passive self-healing system will also be demonstrated in this section. The chapter will then conclude with a summary in Section 5.5.

5.2 Practical Realisation

The self-healing cantilever beam in Figure 5.2 is a practical example of the unified sensing, diagnosis and active self-healing.

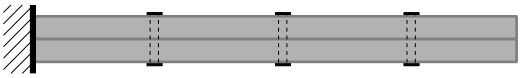

Figure 5.2: Self-healing cantilever beam. The definitions of the colours are: grey- piezo-electrolyte composite, black- electrically conductive material acting as electrodes (e.g. steel bolt).

The cantilever beam consists of layers of piezo-electrolyte composite held together by an electrically conductive material. Such materials have already been demonstrated to possess self-healing properties (Sayayr et al., 2014; Soroushian et al., 2012). The electrically conductive material acts as electrodes and in an open loop passive mode, the piezoelectric properties of the material converts induced stress from a vibration shaker on one of the electrodes into electrical energy. This converted energy drives the deposition of healing agent (copper nanoparticles) in the vicinity of the electrode. In the proposed active self-healing mode, additional components are added on the beam. Accelerometers are placed in strategic places on the beam to measure the beam's acceleration for the purpose of diagnosis. The control system and fault diagnosis can be implemented using either dSpace or National Instrument rapid control prototyping (RCP) hardware. The voltage demands of the control system is added by a power supply unit while a current transducer is attached to the electrodes to measure the current during electrolysis. An induced fault in form of a cut on the surface of the electrode changes the local stiffness of the beam. In the active self-healing mode, the desired healing rate is a function of the fault condition and is determined by the vibration analysis of the proposed fault diagnosis. Given that the cantilever beam is held together by more than one bolt (electrode), the diagnosed location determines the electrode to be activated. The control system demands a voltage from the power supply unit based on the output of the fault diagnosis (that is, the desired healing rate). Essentially, the controller adds to the vibration input (piezo-induced voltage) to ensure a desired current flow that will deposit a mass of the healing agent (copper nanoparticles) to seal the cut during self-healing process.

5.3 Mathematical Preliminaries

Figure 5.3 shows a cantilever beam with an induced fault in form of a cut on the surface of the electrode. This is analysed by the proposed fault diagnosis from Chapter 4 to estimate the crack depth and location.

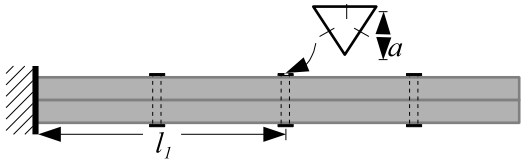

Figure 5.3: A cracked cantilever beam.

Given that the control system activates the electrode used to supply the voltage demands, the activation status s_{act} of r_o number of electrodes is defined as Equation (5.1):

$$s_{act} = \begin{bmatrix} b_1 & b_2 & b_3 & ... & b_{r_o} \\ 0 & 0 & 0 & ... & 0 \end{bmatrix}_{2\times r_o} \tag{5.1}$$

where b_{io} captures the position of the electrode and $io \in [1 \;\; r_o]$. The second row of Equation (5.1) represents the corresponding electrode status, given that a 0 implies a deactivated electrode and a 1 indicates an activated electrode. The estimated fault location l_{est} can be compared with the electrode locations to determine which element in the second row of Equation (5.1) to be flagged as 1. That is:

$$s_{act}(2, io) = \begin{cases} 1 & \text{if } l_{est} = b_{io} \\ 0 & \text{otherwise} \end{cases} \tag{5.2}$$

The estimated crack depth can be used to formulate a reference model for the control input to match. Equation (5.3) defines a normalised estimated crack depth such that $\frac{a_{est}}{h} = 0$ implies no crack and $\frac{a_{est}}{h} = 1$ indicates maximum crack depth; where h is the beam height.

$$\frac{a_{est}}{h} \sim [0, 1] \tag{5.3}$$

The reference model $\dot{Q}_d$ is defined by the normalised crack estimate and a gain g in Equation (5.4). The gain g adds the flexibility of increasing the control effort and reducing the self-healing time.

$$\dot{Q}_d(t) = g\frac{a_{est}(t)}{h} \tag{5.4}$$

A crack can form different shapes but in this research, the shape formed is taken to be an equilateral triangle and shown in Figure 5.3. This shape has been chosen primarily to demonstrate the proposed concept and may not necessarily represent all possible shapes of a propagated crack. Equation (5.5) defines the volume to be filled at the first instance of a crack.

$$V_{f_{est}} = \frac{\sqrt{3}}{3}a_{est}(t_f)^2 w \tag{5.5}$$

The term $a_{est}(t_f)$ is the estimated crack depth at the fault time t_f, w is the beam width. Since the width of the beam remains unchanged, equation (5.5) implies that the estimated volume $V_{f_{est}}$ to be filled and the square of the estimated crack depth a_{est}^2 are in direct proportionality. Equation (5.5) is expressed in terms of the estimated mass $M_{c_{est}}$ to fill the crack because of the choice of self-healing mechanism considered in this research. The estimated mass is defined as Equation (5.6).

$$M_{c_{est}} = \frac{\sqrt{3}}{3}\rho_{sh}a_{est}(t_f)^2 w \tag{5.6}$$

Figure 5.4: A step by step visual of the copper nanoparticles coating during healing.

During self-healing, it is assumed that surface coating is even to retain the equilateral shape of the reduced crack (see Figure 5.4). This is again for

simplicity and for the purpose of demonstrating the proposed concept. In practice, even coating may not necessarily represent the actual healing process since the ions move randomly during electrolysis. Thus, leading to an uneven coating of the crack surface (Sayayr et al., 2014; Soroushian et al., 2012), and this can be obtained experimentally. The healing agent with a density ρ_{sh} deposits a mass $\int_{t_f}^{t_h} \dot{M}_h(t)dt$ between the fault time t_f and the healed time t_h until the total depth filled $a_{sh}(t_h)$ is equal to the estimated crack depth $a_{est}(t_f)$. Also, ρ_{sh} is not necessary equal to the density ρ of the material. To achieve $a_{sh}(t_h) = a_{est}(t_f)$, equation (5.7) must hold.

$$\int_{t_f}^{t_h} \dot{M}_h(t)dt = M_{c_{est}} \tag{5.7}$$

In self-healing mode, the fault monitoring index in Equation (4.25) is redefined as Equation (5.8).

$$index(t) = \begin{cases} 0, & \text{if } \int_{t_f}^{t_h} \dot{M}_h(t)dt = M_{c_{est}} \text{ (fault healed)} \\ 1, & \text{otherwise (fault mode)} \end{cases} \tag{5.8}$$

Similarly, the second row of Equation (5.1) is reset to zero.

5.4 Active Self-healing Example Simulations

The self-healing system is modelled as a carbon-fibre/PVDF-HFP composite cantilever beam of dimensions 820 mm by 20 mm by 10 mm using a finite element model with 25 elements. The mechanical and electrical properties are presented in Table 5.1 while the control parameters are in Table 5.2. The density of the healing agent is ρ_{sh}=8950 kg/m^3, that is, the copper nanoparticles used in the experiments carried out by Sayayr et al. (2014) and Soroushian et al. (2012). All simulations and analyses are carried out in Matlab. These system properties are chosen to demonstrate the conceptual idea of a unified sensing, diagnosis and active self-healing system.

Table 5.1: Properties of a composite cantilever beam (Krawczuk et al., 1997; Kuponu et al., 2016; Reverchon and Cardea, 2006; Sayayr et al., 2014).

Properties	Matrix	Carbon-Fibre	PVDF-HFP
Young's Modulus E	3.43 GPa	275.6 GPa	44 GPa
Poisson ratio v	0.35	0.2	0.33
Density ρ	1250 kg/m^3	1900 kg/m^3	1780 kg/m^3
Volume fraction	17	45	38
Piezoelectric coupling d_{33}	-	-	-24 pC/N
Number of layers z	-	-	130
Resistance R	-	-	19.2 $k\Omega$
Capacitance C	-	-	1.59 μF

Table 5.2: Control and other system parameters. (Kuponu et al., 2017a)

Parameter	Value
K^*	2.5
λ_c	5
K_d	50
γ	0.5
m_{min}	0.01
ϵ	0.01
g	1
δ	8.4×10^{-7}

The deflections and radius of curvatures of four modes of the intact beam and a 3 mm cracked beam at location 295.2 mm are shown in Figure 5.5.

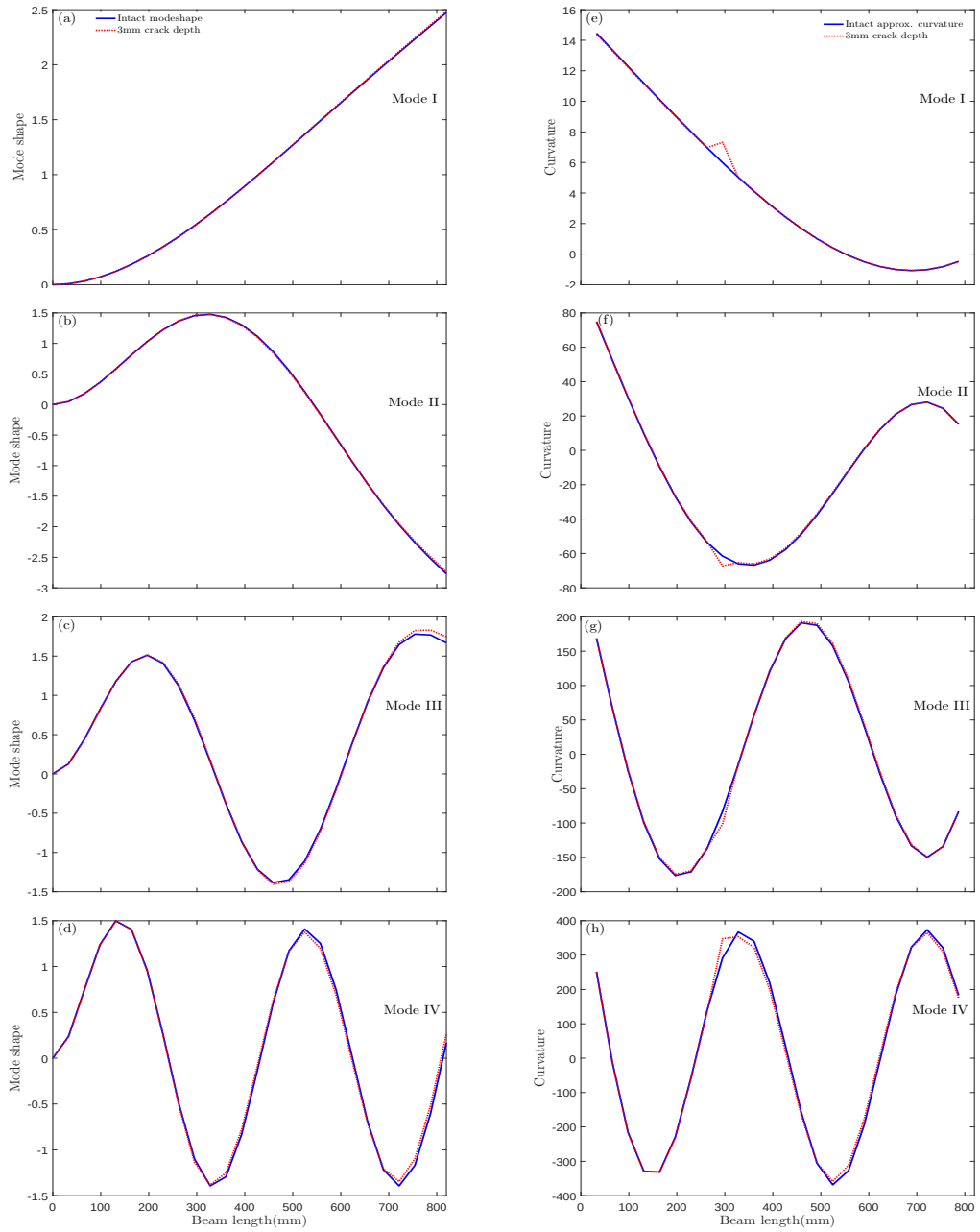

Figure 5.5: Mode shape (a-d) and radius of curvature (e-h) of the first four modes of an intact and a 3mm cracked beam at location 295.2mm

Similarly, the presence of a crack in the beam results in changes in the modal frequencies as seen in Table 5.3. The POD algorithm is applied to extract unique features associated with the intact curvature and the cracked curvature. According to Figure 5.6a, the difference between the extracted

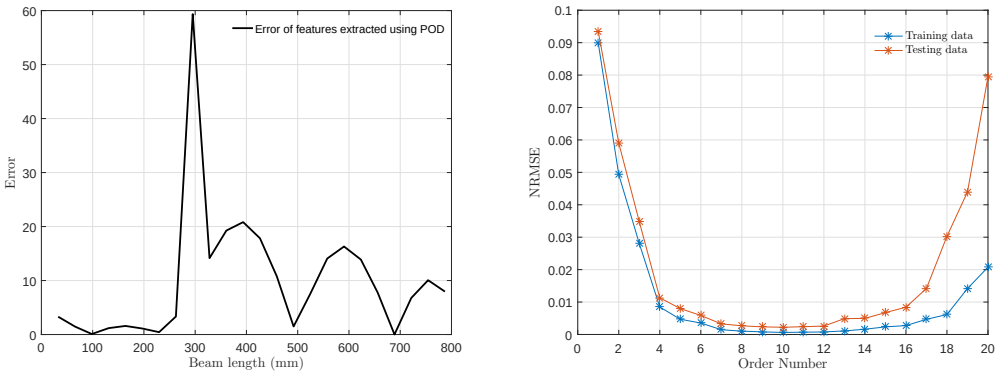

(a) **(b)**

Figure 5.6: (a) Difference between the unique features extracted by POD from an intact and the cracked beam curvatures. (b) Cross-validation: The normalised root mean square (NRMSE) of different polynomial order used to select the order number. This step avoids under and over fitting.

features suggests that the point of maximum peak is the crack location. The order of the polynomial expressed in Equation (4.31) is selected as $r = 10$ based on the cross-validation carried out in Figure 5.6b. This ensures that under and over fitting of the regression is avoided. The corresponding weightings are found in Equation (E.4) of Appendix E. The performance of the crack diagnosis to different crack depths and locations is shown in Table 5.3.

An open loop passive self-healing system is investigated when a 3 mm crack located at 295.2 mm (i.e., second electrode) is introduced at 10 $seconds$. Forces of 1 N and 0.6 N are applied continuously at a frequency of 100 rad/sec to the electromechanical composite material at $10s$ and $150s$ respectively. These forces are representative of the normal operating characteristics of a structure, for example, input from rotating machinery, footfall on a bridge, turbulence on an aircraft, waves on a ship, etc. This takes advantage of the piezoelectric effect of the electromechanical material to generate equivalent voltages of 1.86 mV and 1.11 mV respectively. The voltages are rectified to drive the electrolytic process. The results of the passive healing process are shown in Figure 5.7 to highlight the inherent drawback of this process. The healing process is not initiated because the chemical kinetic needed to deposit the healing agent i.e.

Table 5.3: Crack depth outcome of the FDD at different locations and the corresponding modal frequencies of a cantilever beam

Crack location (mm)		Crack depth (mm)			Frequency (Hz)			
Actual	*Estimated*	*Actual*	*Estimated*	*%Error*	f_1	f_2	f_3	f_4
-	-	-	-	-	15.51	97.21	272.20	533.40
98.40	98.40	1.00	1.00	0.28	15.49	97.18	272.19	533.34
98.40	98.40	1.50	1.50	0.05	15.46	97.13	272.19	533.28
98.40	98.40	2.00	2.00	-0.24	15.43	97.07	272.18	533.19
98.40	98.40	2.50	2.49	0.22	15.38	97.00	272.17	533.07
98.40	98.40	3.00	2.99	0.48	15.32	96.90	272.16	532.92
196.80	196.80	1.00	1.00	0.04	15.50	97.21	272.03	532.95
196.80	196.80	1.50	1.50	0.00	15.48	97.21	271.83	532.42
196.80	196.80	2.00	2.00	0.04	15.46	97.21	271.55	531.70
196.80	196.80	2.50	2.49	0.21	15.43	97.20	271.19	530.76
196.80	196.80	3.00	3.02	-0.78	15.39	97.20	270.73	529.57
295.20	295.20	1.00	1.00	0.12	15.50	97.16	272.00	533.40
295.20	295.20	1.50	1.50	0.01	15.49	97.11	271.77	533.39
295.20	295.20	2.00	2.00	-0.13	15.48	97.03	271.45	533.39
295.20	295.20	2.50	2.50	-0.04	15.46	96.92	271.03	533.39
295.20	295.20	3.00	2.97	1.11	15.44	96.79	270.50	533.39
393.60	393.60	1.00	1.01	-0.73	15.51	97.11	272.19	532.88
393.60	393.60	1.50	1.50	0.06	15.50	97.00	272.19	532.27
393.60	393.60	2.00	2.00	-0.01	15.50	96.84	272.18	531.44
393.60	393.60	2.50	2.50	-0.01	15.49	96.63	272.17	530.34
393.60	393.60	3.00	3.01	-0.36	15.48	96.37	272.16	528.95
492.00	492.00	1.00	1.01	-0.67	15.51	97.12	272.04	533.29
492.00	492.00	1.50	1.50	0.11	15.51	97.01	271.86	533.16
492.00	492.00	2.00	2.00	0.06	15.51	96.86	271.62	532.99
492.00	492.00	2.50	2.50	0.10	15.50	96.66	271.29	532.76
492.00	492.00	3.00	3.01	-0.47	15.50	96.41	270.88	532.46
590.40	590.40	1.00	1.01	-0.79	15.51	97.17	271.88	533.06
590.40	590.40	1.50	1.50	-0.05	15.51	97.11	271.51	532.68
590.40	590.40	2.00	2.00	0.15	15.51	97.03	271.00	532.15
590.40	590.40	2.50	2.50	-0.00	15.51	96.93	270.32	531.45
590.40	590.40	3.00	2.96	1.17	15.51	96.80	269.46	530.57
688.80	688.80	1.00	0.99	0.85	15.51	97.20	272.08	532.91
688.80	688.80	1.50	1.50	-0.23	15.51	97.19	271.94	532.33
688.80	688.80	2.00	2.00	0.03	15.51	97.18	271.74	531.53
688.80	688.80	2.50	2.50	-0.11	15.51	97.16	271.48	530.48
688.80	688.80	3.00	2.96	1.31	15.51	97.13	271.14	529.11

copper nanoparticles, is not present. The generated piezo-induced voltages are less than E_{rev}, and as a result, no current flow to deposit the healing agent (see Figures 5.7a - 5.7c). Figures 5.7d - 5.7e show a current flow when the voltages are amplified by a gain of 6. The piezoelectric and electrolytic components of the self-healing material are considered as separate elements, while the addition of amplification leads the system to operate more in an open-loop as opposed

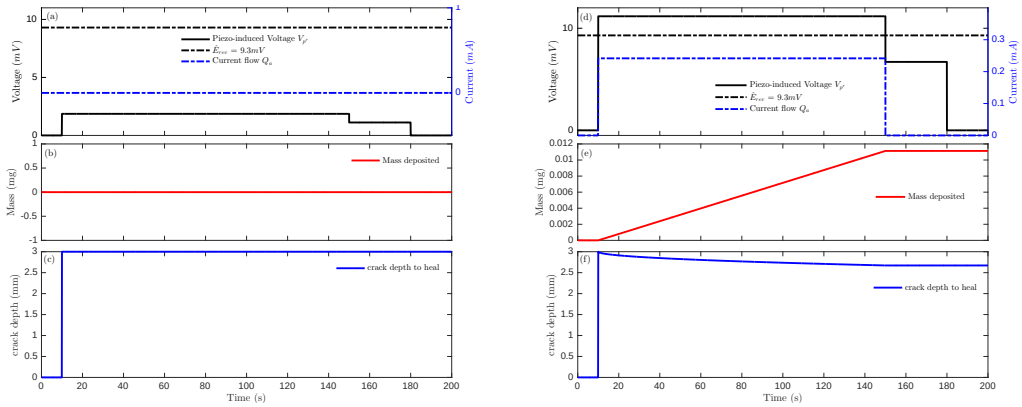

Figure 5.7: Illustration of an open loop self-healing process for a 3mm crack depth located at 295.2mm and introduced at 10seconds: (a-c) The electromechanical material converts applied force of 1 N and 0.6 N to 1.86 mV and 1.11 mV respectively. This causes a dead-zone i.e. no current flow because the voltages are less than E_{rev}. Thus no healing and no mass deposited to reduce the crack depth. (d-f) The amplified voltages produce current flow for mass deposition and the crack depth is reduced during healing.

to a passive self-healing mode. At 150 seconds, the system again experiences a dead-zone because the amplified voltage drops below E_{rev} (see black dashes in Figure 5.7d) as the crack is healed. The chemical kinetic produced between 10 and 150 seconds deposits a mass, leading to a reduction in the crack depth (see Figures 5.7f). However, a complete healing was not achieved because the crack depth does not reduce to zero. This is a result of the duration the applied stress and the inherent dead-zone of the self-healing mechanism. More so, amplification does not necessarily guarantee a desired response. An open loop system is unreliable and does not benefit from a feedback mechanism to achieve a desired response. The fundamental issue with this arrangement is that the piezoelectric and electrolyte are mixed in the self-healing material and can not be considered as separate elements. Nonetheless, this analysis shows the effect of amplification from a conceptual point of view. Similarly, the effect of uncertainties or disturbances defined in Section 2.5 of Chapter 2 was investigated on the self-healing system and shown in Figure 5.8. The voltage between 10 and 150 seconds is greater than E_{rev} but the system operates in

the dead-zone region; hence no self-healing. This shows that uncertainties have an adverse effect on the self-healing process.

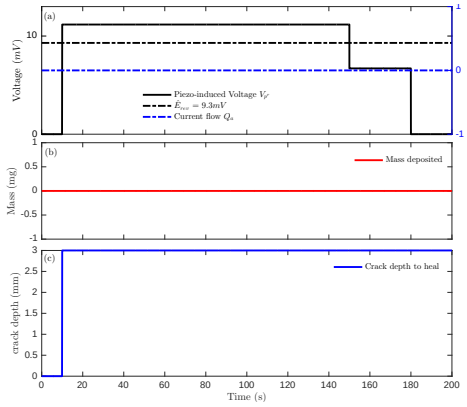

Figure 5.8: The effect of uncertainties on an open loop self-healing process for a 3mm crack depth located at 295.2mm and introduced at 10seconds: The voltage between 10 and 180 seconds is greater than E_{rev} but the system operates in the dead-zone region; hence no self-healing. This is due to the effect of uncertainties on the self-healing system.

In comparison, real time monitoring of the self-healing system in the presence of uncertainties or disturbances is presented to demonstrate the concept of unified sensing, diagnosis and active self-healing in Figures 5.9 - 5.11. Figure 5.9 shows an electrolytic self-healing process driven by the control input. Up until 10 seconds, the monitoring index indicates a healthy system shown as the blue dash-dotted line in Figure 5.9a. At 10 seconds, a crack is detected at location 295.2 mm and flagged by the monitoring index (see blue line in Figure 5.9a)The estimated crack location also allows the control system to trigger the second electrode based on Equations (5.1) - (5.2). The fault diagnosis quantifies and estimates the crack depth as 2.97 mm; that is, a deviation of 1.11% from the actual 3 mm crack depth. The adaptive controller gets information from the fault diagnosis algorithm and induces a matching external stimuli (black line of Figure 5.9b) that ensures a match between the damage and the healing rate (see red dashed line and blue line in Figure 5.9a). During healing, the crack gradually reduces (see red dotted line in Figure 5.9c) as the estimated required mass (Equation (2.8) and Figure 5.9d) is attained. However, poor estimates at lower crack depths cause the controller to supply the wrong external energy

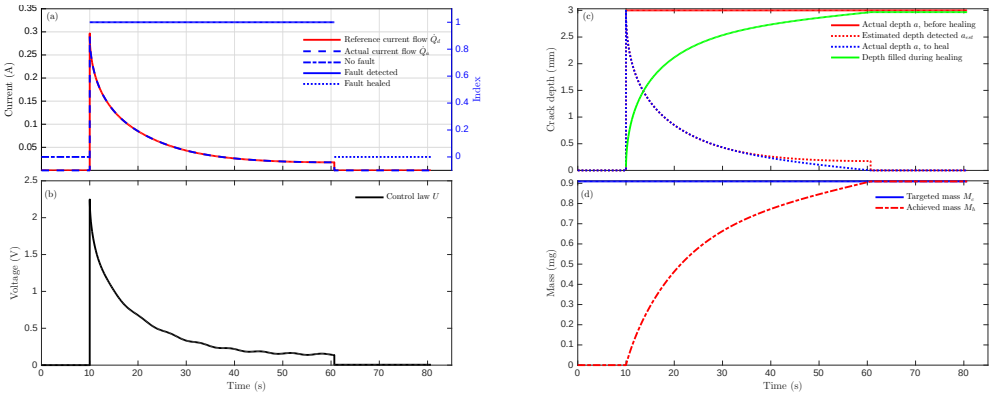

Figure 5.9: Integrated sensing, diagnosis and active self-healing system illustrated for a 3mm crack depth located at 295.2mm and introduced at 10 seconds. This ignores the piezoelectric effect and drives the electrolytic process with the control only. The control produces an external energy that matches the diagnosed estimated damage. This ensures that a desired healing response is achieved but as the crack decreases, the fault diagnosis becomes inaccurate in estimating the damage rate.

(see black line of Figure 5.9b and red dotted line of Figure 5.9c) from about 40 seconds. This is evident in Figure 5.9a where the measure of damage and the matching response abruptly jumps to zero and the monitoring index indicates the fault healed status (blue dotted line in Figure 5.9a). Other examples of poor estimates for different crack depths and locations can be found in Figure E.1 of Appendix E.

5.4.1 Active Self-healing with Modified Weightings

Despite the poor crack estimates at lower depth, the current flow during electrolysis achieved the estimated required mass. However, the effectiveness of the adaptive control to supply the correct external input for the self-healing process depends on the accuracy of the fault diagnosis. Hence, the need for an improved diagnosis. To estimate the crack depths as close as possible to zero, the weightings in Equation (4.35) are adapted as the crack depth reduces; this is expressed as Equation (5.9):

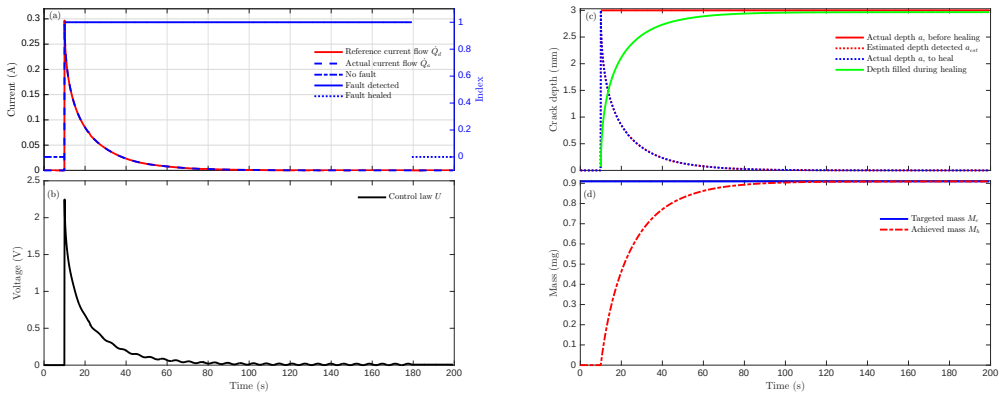

Figure 5.10: Integrated sensing, diagnosis and active self-healing system illustrated for a 3mm crack depth located at 295.2mm and introduced at 10 second with the adapted weightings. The diagnosis at lower crack depth becomes more accurate and the control produces an external energy that matches the diagnosed estimated damage rate. This ensures that a desired healing response is achieved all through the healing process.

$$\zeta = \begin{cases} \begin{bmatrix} \zeta 1_i & \zeta 2_i & \dots & \dots & \zeta rj_i \end{bmatrix}_{1\times rj} & \text{if } a > 0.75mm \\ \begin{bmatrix} \zeta 1_{ii} & \zeta 2_{ii} & \dots & \dots & \zeta rj_{ii} \end{bmatrix}_{1\times rj} & \text{if } a > 0.1mm \ \& \ a \leq 0.75mm \\ \begin{bmatrix} \zeta 1_{iii} & \zeta 2_{iii} & \dots & \dots & \zeta rj_{iii} \end{bmatrix}_{1\times rj} & \text{if } a > 0.03mm \ \& \ a \leq 0.1mm \\ \begin{bmatrix} \zeta 1_{iv} & \zeta 2_{iv} & \dots & \dots & \zeta rj_{iv} \end{bmatrix}_{1\times rj} & \text{if } a > 0.008mm \ \& \ a \leq 0.03mm \\ \begin{bmatrix} \zeta 1_{v} & \zeta 2_{v} & \dots & \dots & \zeta rj_{v} \end{bmatrix}_{1\times rj} & \text{if } a \leq 0.008mm \end{cases} \tag{5.9}$$

Figure 5.10 shows the result of the proposed self-healing framework with the adapted weightings. The corresponding adapted weightings are found in Equations (E.4) - (E.8) of Appendix E. Smaller crack depths are better estimated and the appropriate external energy is supplied by the control. The results in Figure 5.10 can be compared with its equivalent passive self-healing in Figures 5.7(d-f). The passive self-healing reduced the crack depth to less

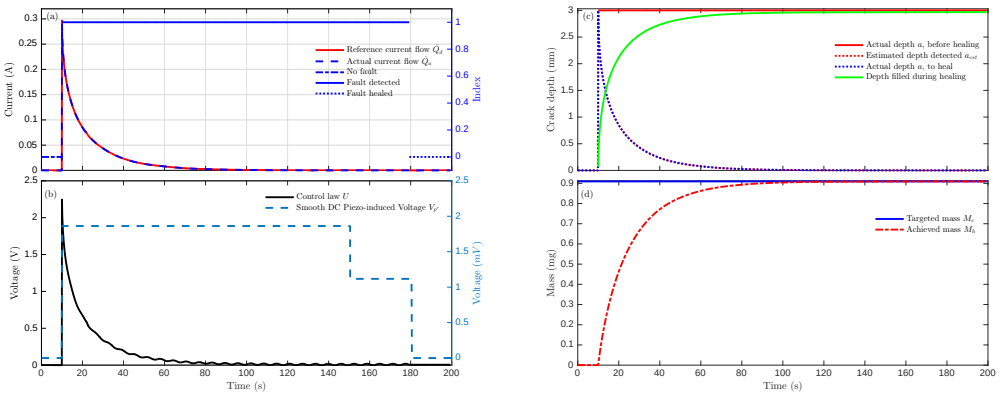

Figure 5.11: Integrated sensing, diagnosis and active self-healing system is demonstrated for a composite self-healing material whose healing mechanism is driven by piezoelectricity and electrolysis. The electromechanical material produces insufficient voltages when forces of 1 N and 0.6 N are applied. This leads to in a dead-zone and no healing but the adaptive control compensates and ensures that a desired healing response that is based on a diagnosed output is achieved.

than three quarters of the initial crack depth while the proposed self-healing framework achieved a crack depth that is closer to zero. This demonstrates some of the challenges faced by passive self-healing that the unified sensing, diagnosis and active self-healing system can overcome. However, the inclusion of secondary systems, sensors and actuators increases the complexity and cost of the self-healing system; and can potentially make the system unstable. Other example simulations of the proposed self-healing system at different crack locations are shown in Figures E.2 - E.3 of Appendix E. Figure 5.11 demonstrates a composite self-healing material whose healing mechanism is driven by piezoelectricity and feedback controlled electrolysis. Like with the open loop process in Figure 5.7a, the piezo-induced voltages are insufficient to drive the healing process. The adaptive controller supplies external energy to compensate for the insufficient voltages and to match the estimated damage rate. Also, the match between the estimated damage rate and the healing rate was achieved in the presence of uncertainties. The gradual decrease of the crack depth during the active self-healing process is shown in Figure 5.12.

The induced crack depth at 10 seconds begins to decrease at the healing agent (copper nanoparticles) is deposited over time.

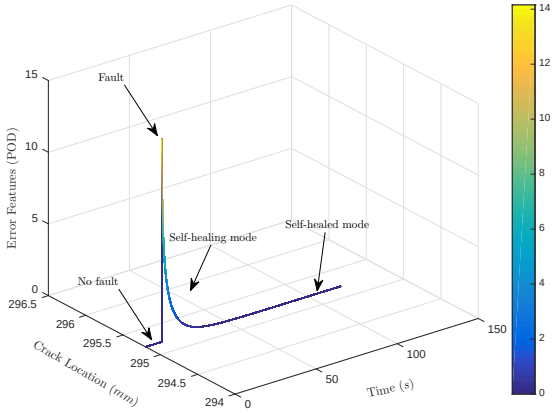

Figure 5.12: The effect of healing at a crack location using the difference between the unique features extracted by POD from an intact and a cracked beam of curvatures.

5.5 Conclusion

This chapter presents a novel concept of a unified sensing, diagnosis and active self-healing system framework as an alternative to a passive self-healing system. The framework integrates the self-healing mechanism modelled in Chapter 2, the feedback control formulation of Chapter 3 and the new fault diagnosis algorithm of Chapter 4. This ensures that a proper match between the estimated damage rate and the healing rate is achieved while taking into account the inherent dead-zone non-linearity of the self-healing mechanism, disturbances and uncertainties that may be encountered during self-healing. Self-healing composite materials were modelled and simulated as cantilever beams to represent a range of applications in engineering systems like footbridges, airliner wings, turbine blades, etc. The healing mechanisms demonstrated were that of an isolated electrolytic process and a piezo-electrolytic process. Simulation results successfully showed that:

1. Real-time condition monitoring and diagnosis enables early prediction of fault and current healing state.

2. Effective healing can depend on the condition monitoring and diagnosis to maximize healing at the fault location.

3. The self-healing process can be regulated and an effective match between the healing rate and the estimated damage rate (defined by the fault diagnosis) can be achieved. This was achieved in constant and changing environment particularly as the self-healing systems are exposed to uncertainties and disturbances.

Overall, the work presented in this chapter is an important milestone to the successful implementation of self-healing in industrial applications. The next chapter summarises and gives a conclusion on all the investigations made in this research. Possible future research directions are also recommended.

Chapter 6

Conclusion and Future Work

In this closing chapter, a conclusion of the current work are presented in Section 6.1 and future research directions are discussed in Section 6.2.

6.1 Conclusion

The emphasis of the work in this research was on addressing some of the technical drawbacks in self-healing. These include: (i) the passive way healing is initiated; (ii) the unregulated nature of the healing process; (iii) no monitoring of the current healing state or dynamics; (iv) The location of healing mechanisms determine the effectiveness of healing. This means that maximum healing is not guaranteed at the fault location. More importantly, the effect of these drawbacks is a mismatch between the healing rate and damage rate.

This research investigated how the rate of healing can be controlled and optimized with active self-healing. In Chapter 2, a mathematical model of a self-healing mechanism was formulated. The model is based on previous experimental works by Soroushian et al. (2012) and Sayayr et al. (2014), which proposed an electromechanical material system whose intrinsic self-healing mechanism is based on a piezo-electrolytic drive. The piezoelectric direct effect transforms an induced stress into electrical energy, which drives the healing agent (copper nano-particles) through an electrolysis process to the

damaged region. Importantly, the formulation laid the foundation to investigate the healing rate of a typical passive self-healing process and to develop the active self-healing system in subsequent chapters. In addition to the listed drawbacks above, this particular self-healing system suffers from an inherent non-linear dead-zone which limits the performance of self-healing. The analysis carried out on the passive self-healing system revealed that the healing process does not guarantee that the onset of damage is stopped. Also, the process is unable to achieve the desired healing response over a period of time and handling of uncertainty/disturbance is also poor. More so, amplification of the piezo-induced voltage was investigated from a conceptual point of view. The piezoelectric and electrolytic component of the self-healing material were considered as separate elements, rather than as a mixture in the self-healing material. In this arrangement, the system operates more in an open-loop as opposed to a passive self-healing mode but remains unreliable and does not guarantee a desired healing response; since the system does not benefit from any feedback mechanism.

An active self-healing system was presented in Chapter 3. This was a closed loop system that takes advantage of sensing and feedback control to regulate the healing rate to meet user or environmental demands, such as the need to match the damage rate. Adaptive sliding mode controllers were designed and implemented to overcome the unknown dead-zone, as well as to ensure a proper match between the healing and damage rate. By using sinusoidal stress inputs with constant and changing amplitudes, the effect of controlled self-healing system to constant and varying conditions was investigated. The control simulations successfully showed that the healing rate can be effectively regulated and matched with environmental demands (damage rate). In particular, the effect of uncertainties or disturbances was investigated and results revealed that the active self-healing system can potentially minimize this effect, while ensuring a desired healing response. In contrast, the passive self-healing performs poorly in the presence of uncertainties and a desired healing response

was not guaranteed. The active self-healing results are an important milestone in regulating the healing rate, with reference to an estimated damage rate, of a self-healing system. Also, an active self-healing system can benefit from a secondary fault diagnosis system to estimate the damage rate. Thus, Chapter 4 focussed on developing a fault diagnosis system for beam structures. This benefits from sensor measurements to detect and quantify faults. A beam structure was selected because it represents many industrial systems such as helicopter, airliner wings, bridges, turbine blades, etc. Precisely, the fault diagnosis system combined the beam curvature, proportional orthogonal decomposition, hölder exponent and supervised regression to estimate the crack depth and location associated with a faulty beam. Simulation results showed a high degree of accuracy in detecting the crack depth and location of cantilever and fixed beams. In particularly, a sensitivity analysis carried out shows the robustness of the fault diagnosis system to uncertainty / disturbance. Similarly, the proposed fault diagnosis system in this research was compared with the genetic algorithm implemented by Vakil-Baghmisheh and Peimani (2008); comparison affirmed the high degree of accuracy of the proposed fault diagnosis system.

Importantly, the works presented thus far formed the basis for which a unified sensing, diagnosis and active self-healing system was formulated in Chapter 5, as an alternative to the passive self-healing. This essentially combined sensing, monitoring and diagnosis, feedback control and self-healing to regulate the healing process. From a practical perspective, a beam was considered as a self-healing composite material, and the healing mechanisms demonstrated were that of an isolated electrolytic process and piezo-electrolytic process. The fault diagnosis system was used to estimate the damage rate of a cracked beam. The unified system was simulated and results revealed that real-time condition monitoring enabled early prediction of fault and current healing state of the process. Also, the effectiveness of healing depends on the condition monitoring and diagnosis; thus, maximizing healing at the fault location. The self-healing process is regulated, while the diagnosis system ensured that the

needed energy or effort required by the feedback controller to match the healing and estimated damage rate was achieved. These results were compared with those obtained from a passive self-healing system, and comparison showed a significant discrepancy between the two systems. Importantly, the unified self-healing system suggests an efficient way to counteract the effect of damage and improve the performance of self-healing, particularly as the materials are exposed to uncertainties.

In conclusion, improving the rate of healing of self-healing systems is one of key contributions of this research. System complexities and consumer requirements have resulted in a rise in the use of composite materials (Hale, 2006); hence, systems can potentially benefit from self-healing. More so as this contribution is an important milestone to successful implementation of self-healing in industrial applications. Hence, the proposed unified self-healing system potentially offers economic and environmental benefits, improved reliability and aversion of a disastrous event that could be life threatening. The unified self-healing system also overcomes some of the drawbacks of passive self-healing but has its challenges. The inclusion of secondary systems, sensors and actuators increases the complexity and cost of the self-healing system; and can potentially make the system unstable. Nonetheless, this research sets a theoretical framework for other research works on self-healing to develop into industrial application and improve the technological readiness. Other key contributions are set out in the following section.

6.2 Future Work

Below is a list of suggested future research directions.

i The unified sensing, diagnosis and active self-healing system presented in this research has been analysed and simulated using a computer aided tool, that is, Matlab. However, experimental validation of the proposed work is essential. This would give more insight into the findings and

help improve the mathematical formulations presented in this research. Assumptions such as the crack shape, the shape formed and the coating during self-healing will be well formulated with experimental validation.

ii This work has demonstrated a unified sensing, diagnosis and active self-healing system using two intrinsic self-healing mechanisms, that is, the electrolytic and the piezo-electrolytic self-healing mechanisms. Be that as it may, a variety of self-healing methods and mechanisms exist and the proposed work can be extended to other methods. This will validate the flexibility and adaptability of unified sensing, diagnosis and active self-healing system to other self-healing methods and mechanism.

iii While the current work suggests a maximum healing at a location detected by the fault diagnosis system, a distributed network of sensors and actuation can be considered for further exploration. This should investigate how healing can be more effective by channelling energy from the distributed actuation to the point of maximum need.

iv In the absence of experimental validation, a comparison of the presented fault diagnosis system with the works of Vakil-Baghmisheh and Peimani (2008) was made for validation. However, the fault diagnosis system can benefit from experimental validation and an extension to other beam structures such as a simply supported beam.

References

Amezquita-Sanchez, J. and Adeli, H. (2016). Signal processing techniques for vibration-based health monitoring of smart structures. *Archives of Computational Methods in Engineering*, 23(1):1–15.

Angrisani, L., Daponte, P., and D'Apuzzo, M. (1999). A method for the automatic detection and measurement of transients. Part I: the measurement method. *Measurement*, 25(1):19–30.

Aviation Safety Council (2005). China Airlines Flight CI-611 Crash Report Released. Technical report, International Aviation Safety Organisation.

Barambones, O. and Alkorta, P. (2011). A robust vector control for induction motor drives with an adaptive sliding-mode control law. *Journal of the Franklin Institute*, 348(2):300–314.

Bartolini, G., Pisano, A., and Punta, E. (2003). A survey of applications of second-order sliding mode control to mechanical systems. *International Journal of control*, 76(9-10):875–892.

BBC (2013). Bangladesh factory collapse toll passes 1,000.

Bessa, W. M., Dutra, M. S., and Kreuzer, E. (2010). Sliding Mode Control with Adaptive Fuzzy Dead-Zone Compensation of an Electro-hydraulic Servo-System. *Journal of Intelligent and Robotic Systems*, 58(1):3–16.

Blaiszik, B., Kramer, S., Olugebefola, S., Moore, J., Sottos, N., and White, S. (2010). Self-Healing Polymers and Composites. *Annual Review of Materials Research*, 40(1):179–211.

Bleay, S. and Loader, C. (2001). A smart repair system for polymer matrix composites. *Composites Part A: Applied Science and Manufacturing*, 32(12):1767–1776.

Brown, E., Kessler, M., Sottos, N., and White, S. (2003). In situ poly (Urea-Formaldehyde) Microencapsulation of Dicyclopentadiene. *Journal of Microencapsulation*, 20(6):719–730.

Buljak, V. (2011). *Inverse analyses with model reduction: proper orthogonal decomposition in structural mechanics*. Springer Science & Business Media.

Burattini, S., Colquhoun, H. M., Greenland, B. W., and Hayes, W. (2009). A novel self-healing supramolecular polymer system. *Faraday Discussions*, 143:251–264.

Canadell, J., Goossens, H., and Klumperman, B. (2011). Self-Healing Materials Based on Disulfide Links. *Macromolecules*, 44(8):2536–2541.

Chen, H., Reuss, D. L., and Hung, D. L. S. (2013). A practical guide for using proper orthogonal decomposition in engine research. *International Journal of Engine Research*, 14(4):307–319.

Chen, Q., Ren, X., Na, J., and Zheng, D. (2016). Adaptive robust finite-time neural control of uncertain PMSM servo system with nonlinear dead zone. *Neural Computing and Applications*, pages 1–12.

Chen, X., Dam, M., Ono, K., Mal, A., and Shen, H. (2002). A Thermally Re-mendable Cross-linked Polymeric Material. *Science*, 295(5560):1698–1702.

Chen, X., Wudl, F., Mal, A., Shen, H., and Nutt, S. (2003). New Thermally Remendable Highly Cross-Linked Polymeric Materials. *Macromolecules*, 36(6):1802–1807.

Cho, H. and Bai, E.-W. (1998). Convergence results for an adaptive dead zone inverse. *International Journal of Adaptive Control and Signal Processing*, 12(5):451–466.

Corr, L. R. and Clark, W. W. (2002). Comparison of Low-Frequency Piezoelectric Switching Shunt Techniques for Structural Damping. *Smart Materials and Structures*, 11(3):370–376.

Corradini, M. and Orlando, G. (2003). Robust practical stabilization of nonlinear uncertain plants with input and output nonsmooth nonlinearities. *IEEE Transactions on Control Systems Technology*, 11(2):196–203.

Cui, R., Chen, L., Yang, C., and Chen, M. (2017). Extended State Observer-Based Integral Sliding Mode Control for an Underwater Robot With Unknown Disturbances and Uncertain Nonlinearities. *IEEE Transactions on Industrial Electronics*, 64(8):6785–6795.

Dash, S. and Venkatasubramanian, V. (2000). Challenges in the industrial applications of fault diagnostic systems. *Computers & Chemical Engineering*, 24(2):785–791.

Dawari, V. B. and Vesmawala, G. R. (2013). Structural damage identification using modal curvature differences. *IOSR Journal of Mechanical and Civil Engineering*, 4:33–38.

Doebling, S., Farrar, C., and Prime, M. (1998). A summary review of vibration-based damage identification methods. *Shock and vibration digest*, 30(2):91–105.

Dong, B., Wang, Y., Fang, G., Han, N., Xing, F., and Lu, Y. (2015). Smart Releasing Behavior of a Chemical Self-Healing Microcapsule in the Stimulated Concrete Pore Solution. *Cement and Concrete Composites*, 56:46–50.

Dong, G., Chen, J., and Zou, J. (2004). Parameter identification of a rotor with an open crack. *European Journal of Mechanics-A/Solids*, 23(2):325–333.

Douka, E., Loutridis, S., and Trochidis, A. (2003). Crack identification in beams using wavelet analysis. *International Journal of Solids and Structures*, 40(13):3557–3569.

Draženović, B. (1969). The invariance conditions in variable structure systems. *Automatica*, 5(3):287–295.

Fan, W. and Qiao, P. (2011). Vibration-based damage identification methods: a review and comparative study. *Structural Health Monitoring*, 10(1):83–111.

Feenstra, J., Granstrom, J., and Sodano, H. (2008). Energy Harvesting through a Backpack Employing a Mechanically Amplified Piezoelectric Stack. *Mechanical Systems and Signal Processing*, 22(3):721–734.

Feng, Y., Yu, X., and Man, Z. (2002). Non-singular terminal sliding mode control of rigid manipulators. *Automatica*, 38(12):2159–2167.

Frei, R., McWilliam, R., and Derrick, B. (2013). Self-Healing and Self-Repairing Technologies. *The International Journal of Advanced Manufacturing Technology*, 69(5-8):1033–1061.

Garcia, M. E., Lin, Y., and Sodano, H. A. (2010). Autonomous materials with controlled toughening and healing. *Journal of Applied Physics*, 108(9):093512.

García-Valverde, R., Espinosa, N., and Urbina, A. (2012). Simple PEM water electrolyser model and experimental validation. *International Journal of Hydrogen Energy*, 37(2):1927–1938.

Ghribi, D., Khelifa, A., Diaf, S., and Belhamel, M. (2013). Study of hydrogen production system by using PV solar energy and PEM electrolyser in Algeria. *International Journal of Hydrogen Energy*, 38(20):8480–8490.

González, I., Salazar, S., and Lozano, R. (2014). Chattering-Free Sliding Mode Altitude Control for a Quad-Rotor Aircraft: Real-Time Application. *Journal of Intelligent & Robotic Systems*, 73(1-4):137–155.

Goyal, D. and Pabla, B. (2016). The vibration monitoring methods and signal processing techniques for structural health monitoring: A review. *Archives of Computational Methods in Engineering*, 23(4):585–594.

Hager, M. D., Greil, P., Leyens, C., van der Zwaag, S., and Schubert, U. S. (2010). Self-healing materials. *Advanced Material*, 22(47):5424–5430.

Hale, J. (2006). Boeing 787 from the ground up. *Aero*, 4(24):7.

Hall, J., Qamar, I. P. S., Rendall, T. C. S., and Trask, R. S. (2015). A Computational Model for the Flow of Resin in Self-Healing Composites. *Smart Materials and Structures*, 24(3):037002.

Hamilton, A. R., Sottos, N. R., and White, S. R. (2010). Self-Healing of Internal Damage in Synthetic Vascular Materials. *Advanced Materials*, 22(45):5159–5163.

Han, S.-I. and Lee, J.-M. (2013). Backstepping sliding mode control with FWNN for strict output feedback non-smooth nonlinear dynamic system. *International Journal of Control, Automation and Systems*, 11(2):398–409.

Hansen, C. J., Wu, W., Toohey, K. S., Sottos, N. R., White, S. R., and Lewis, J. A. (2009). Self-Healing Materials with Interpenetrating Microvascular Networks. *Advanced Materials*, 21(41):4143–4147.

Harris, C. J. and Billings, S. (1985). *Self-Tuning and Adaptive Conrol: Theory and Applications*. Peter Peregrinus Ltd., London UK, 2nd edition.

Hayes, S., Jones, F., Marshiya, K., and Zhang, W. (2007). A Self-Healing Thermosetting Composite Material. *Composites Part A: Applied Science and Manufacturing*, 38(4):1116–1120.

Hayes, S., Jones, F., and Zhang, W. (2006). Solid-State Self-Healing of Fibre-Reinforced Composites Materials. *In Proceedings of 15th US National Congress of Theoretical and Applied Mechanic*.

Hoseini Vaez, S. R. and Fallah, N. (2017). Damage Detection of Thin Plates Using GA-PSO Algorithm Based on Modal Data. *Arabian Journal for Science and Engineering*, 42(3):1251–1263.

Hossain, M., Chao, O., Ismail, Z., Noroozi, S., and Yee, K. S. (2016). Artificial Neural Networks for Vibration Based Inverse Parametric Identifications: A Review. *Applied Soft Computing*.

Hou, S., Zhang, H. B., and Ou, J. P. (2012). A PZT-based Smart Aggregate for Compressive Seismic Stress Monitoring. *Smart Materials and Structures*, 21(10):105035.

Hou, Z., Noori, M., and Amand, R. (2000). Wavelet-based approach for structural damage detection. *Journal of Engineering mechanics*, 126(7):677–683.

Huang, H., Ye, G., Qian, C., and Schlangen, E. (2016). Self-healing in cementitious materials: Materials, methods and service conditions. *Materials & Design*, 92:499–511.

Hurley, D. and Huston, D. (2011a). Coordinated Sensing and Active Repair for Self-Healing. *Smart Materials and Structures*, 20(2):025010.

Hurley, D. A. and Huston, D. R. (2011b). Self-Sealing Pneumatic Pressure Vessel With Passive and Active Methods. In *Pressure Vessels and Piping Conference: Volume 6*, pages 107–112. ASME.

Huyang, G., Debertin, A., and Sun, J. (2016). Design and development of self-healing dental composites. *Materials & design*, 94:295–302.

Huyang, G. and Sun, J. (2016). Clinically Applicable Self-Healing Dental Resin Composites. *MRS Advances*, 1(8):547–552.

Isermann, R. (2006). *Fault-Diagnosis System, An Introduction from Fault Detection to Fault Tolerance*. Springer.

Isermann, R., Lachmann, K.-H., and Matko, D. (1992). *Adaptive Control Systems*. Prentice-Hall International (UK) Ltd.

Ivanov, V. and Stabnikov, V. (2017). Advances and Future Developments of Construction Biotechnology. *Construction Biotechnology*, pages 271–277.

Jasim, I. (2013). Improved Observer-Based Robust Adaptive Control for a Class of Nonlinear Systems with Unknown Deadzone. *Proceedings of the Institution of Mechanical Engineers, Part I: Journal of Systems and Control Engineering*, 227(2):184–197.

Jasim, I. F. and Plapper, P. W. (2013). Adaptive sliding mode control of switched constrained robotic manipulators. In *2013 11th IEEE International Conference on Industrial Informatics (INDIN)*, pages 305–310. IEEE.

Jena, P. K. and Parhi, D. R. (2015). A Modified Particle Swarm Optimization Technique for Crack Detection in Cantilever Beams. *Arabian Journal for Science and Engineering*, 40(11):3263–3272.

Jiang, X., Ma, Z. J., and Ren, W.-X. (2012). Crack Detection from the Slope of the Mode Shape Using Complex Continuous Wavelet Transform. *Computer-Aided Civil and Infrastructure Engineering*, 27(3):187–201.

Jones, A. S., Rule, J. D., Moore, J. S., Sottos, N. R., and White, S. R. (2007). Life Extension of Self-Healing Polymers with Rapidly Growing Fatigue Cracks. *Journal of the Royal Society, Interface / the Royal Society*, 4(13):395–403.

Kauranen, P., Lund, P., and Vanhanen, J. (1993). Control of battery backed photovoltaic hydrogen production. *International Journal of Hydrogen Energy*, 18(5):383–390.

Keller, M. W., White, S. R., and Sottos, N. R. (2007). A Self-Healing Poly(Dimethyl Siloxane) Elastomer. *Advanced Functional Materials*, 17(14):2399–2404.

Kessler, M. R. (2007). Self-Healing: A New Paradigm in Materials Design. *Proceedings of the Institution of Mechanical Engineers, Part G: Journal of Aerospace Engineering*, 221(4):479–495.

Korovin, S. and Utkin, V. (1974). Using sliding modes in static optimization and nonlinear programming. *Automatica*, 10(5):525–532.

Krawczuk, M. (2002). Application of spectral beam finite element with a crack and iterative search technique for damage detection. *Finite Elements in Analysis and Design*, 38(6):537–548.

Krawczuk, M., Ostachowicz, W., and Zak, A. (1997). Dynamics of cracked composite material structures. *Computational Mechanics*, 20(1):79–83.

Krstic, M., Kokotovic, P. V., and Kanellakopoulos, I. (1995). *Nonlinear and Adaptive Control Design*. John Wiley & Sons, Inc. New York, 1st edition.

Kuponu, O. S., Kadirkamanathan, V., Bhattacharya, B., and Pope, S. A. (2016). Using feedback control to actively regulate the healing rate of a self-healing process subjected to low cycle dynamic stress. *Smart Materials and Structures*, 25(5):055028.

Kuponu, O. S., Kadirkamanathan, V., Bhattacharya, B., and Pope, S. A. (2017a). Integrated Sensing, Monitoring and Healing of Composite Systems. In *Advances in Science and Technology*, pages 62–68.

Kuponu, O. S., Kadirkamanathan, V., Bhattacharya, B., and Pope, S. A. (2017b). Integrating Self-healing, Control and Fault Diagnosis. *Journal of Intelligent Material Systems and Structures.*

Lee, A., Wang, Y., and Inman, D. (2014). Energy Harvesting of Piezoelectric Stack Actuator from a Shock Event. *Journal of Vibration and Acoustics*, 136(1).

Liu, J. and O'Connor, W. (2014). Electromechanical Modelling for Piezoelectric Flextensional Actuators. *Smart Materials and Structures*, 23(2):025005.

Liu, Y.-L., Chuo, T.-W., Sottos, N. R., Anseth, K. S., Bowman, C. N., Braun, P. V., Sottos, N. R., White, S. R., and Moore, J. S. (2013a). Self-healing polymers based on thermally reversible Diels-Alder chemistry. *Polymer Chemistry*, 4(7):2194.

Liu, Y.-T., Kung, T.-T., Chang, K.-M., and Chen, S.-Y. (2013b). Observer-based adaptive sliding mode control for pneumatic servo system. *Precision Engineering*, 37(3):522–530.

Loutridis, S., Douka, E., and Trochidis, A. (2004). Crack identification in double-cracked beams using wavelet analysis. *Journal of Sound and Vibration*, 277(4):1025–1039.

Luo, X., Ou, R., and Eberly, D. (2009). A Thermoplastic/Thermoset Blend Exhibiting Thermal Mending and Reversible Adhesion. *Applied Materials & Interfaces*, 1(3):612–620.

Man Zhihong, Paplinski, A., and Wu, H. (1994). A robust MIMO terminal sliding mode control scheme for rigid robotic manipulators. *IEEE Transactions on Automatic Control*, 39(12):2464–2469.

Manage, M. and Sorensen, E. (2014). A modelling approach to assessing the feasibility of the integration of power stations with steam electrolysers. *Chemical Engineering Research and Design*, 92(10):1988–2005.

McEvoy, M. and Correll, N. (2015). Materials that Couple Sensing, Actuation, Computation, and Communication. *Science Magazine*, 347(6228):1378.

Meirovitch, L. (2001). *Fundamentals of vibrations*. International Edition, McGraw-Hill.

Mergheim, J. and Steinmann, P. (2013). Phenomenological Modelling of Self-Healing Polymers Based on Integrated Healing Agents. *Computational Mechanics*, 52(3):681–692.

Mignon, A., Devisscher, D., Graulus, G. J., Stubbe, B., Martins, J., Dubruel, P., and Van Vlierberghe, S. (2017a). Combinatory approach of methacrylated alginate and acid monomers for concrete applications. *Carbohydrate Polymer*, 155:448–455.

Mignon, A., Vagenende, M., Martins, J., and Dubruel, P. (2017b). Development of amine-based pH-responsive superabsorbent polymers for mortar applications. *Construction and Building Materials*, 321:556–564.

Minakuchi, S., Sun, D., and Takeda, N. (2014). Hierarchical System for Autonomous Sensing-Healing of Delamination in Large-Scale Composite Structures. *Smart Materials and Structures*, 23(11):115014.

Mirabedini, S., Dutil, I., Gauquelin, L., Yan, N., and Farnood, R. (2015). Preparation of Self-Healing Acrylic Latex Coatings Using Novel Oil-filled Ethyl Cellulose Microcapsules. *Progress in Organic Coating*, 85:168–177.

Nanda, J., Das, L., Das, S., and Das, H. C. (2015). Influence of multi-transverse crack on cantilever shaft. *International Journal of Damage Mechanics*, 24(7):1047–1069.

National Transportation Safety Board (2010). Enbridge Incorporated Hazardous Liquid Pipeline Rupture and Release, Marshall, Michigan. *Pipeline Accident Report NTSB/PAR-12/01*.

Nekoukar, V. and Erfanian, A. (2011). Adaptive fuzzy terminal sliding mode control for a class of MIMO uncertain nonlinear systems. *Fuzzy Sets and Systems*, 179(1):34–49.

Norris, C. J., White, J. A. P., McCombe, G., Chatterjee, P., Bond, I. P., and Trask, R. S. (2012). Autonomous stimulus triggered self-healing in smart structural composites. *Smart Materials and Structures*, 21(9):094027.

Pandey, A. K., Biswas, M., and Samman, M. M. (1991). Damage detection from changes in curvature mode shapes. *Journal of sound and vibration*, 145(2):321–332.

Pereira, F., Mitchell, T., and Botvinick, M. (2009). Machine learning classifiers and fMRI: A tutorial overview. *NeuroImage*, 45(1):S199–S209.

Pérez-Herranz, V., Pérez-Page, M., and Beneito, R. (2010). Monitoring and control of a hydrogen production and storage system consisting of water electrolysis and metal hydrides. *International Journal of Hydrogen Energy*, 35(3):912–919.

Petyt, M. (2010). *Introduction to finite element vibration analysis*. Cambridge university press.

Pisano, A. and Usai, E. (2011). Sliding mode control: A survey with applications in math. *Mathematics and Computers in Simulation*, 81(5):954–979.

Polikar, R. (1996). The wavelet tutorial.

Rao, R. (1998). *Wavelet transforms: Introduction to theory and applications*. Pearson Education India.

Recker, D., Kokotovic, P., Rhode, D., and Winkelman, J. (1991). Adaptive Nonlinear Control of Systems Containing a Deadzone. *Proceedings of the 30th IEEE Conference on Decision and Control*, pages 2111 – 2115.

Reverchon, E. and Cardea, S. (2006). PVDF-HFP Membrane Formation by Supercritical CO2 Processing: Elucidation of Formation Mechanisms. *Industrial & engineering chemistry research*, 45(26):8939–8945.

Robertson, A., Farrar, C., and Sohn, H. (2003). Singularity detection for structural health monitoring using holder exponents. *Mechanical Systems and Signal Processing*, 17(6):1163–1184.

Robertson, A. N. and Farrar, C. R. (2003). Singularity Detection for Structural Health Monitoring Using Holder Exponents. *Mechanical Systems and Signal Processing*, 17(6):1163–1184.

Satkoski, C. (2011). Dynamic Modeling of a Piezoelectric Actuated Fuel Injector. *Journal of Dynamic Systems, Measurement, and Control*, 133(5):051011.

Sayayr, M., Weerasiri, R. R., Balachandra, A. M., and Soroushian, P. (2014). Inherently Adaptive Polymer Nanocomposites. *Journal of Applied Polymer Science*, 131(16):40620.

Shen, M., Bennett, N., Ding, Y., and Scott, K. (2011). A Concise Model for Evaluating Water Electrolysis. *International Journal of Hydrogen Energy*, 36(22):14335–14341.

Shen, M., Zhang, J., and Scott, K. (2004). The General Rule of Power Converted from Chemical Energy to Electrical Energy. *Fuel Cells*, 4(4):388–393.

Sherir, M., Hossain, K., and Lachemi, M. (2016). Self-healing and expansion characteristics of cementitious composites with high volume fly ash and MgO-type expansive agent. *Construction and Building Materials*, 127:80–92.

Slotine, J. and Li, W. (1991). *Applied Nonlinear Control*. Prentice-Hall International, Inc.

Smith, M. and Janet DiGiacomo, C. (2014). Delta Plane Loses Wing Panel During Flight.

Song, F. and Smith, S. (2000). Design of sliding mode fuzzy controllers for an autonomous underwater vehicle without system model. In *In Oceans 2000 MTS/IEEE Conference and Exhibition, IEEE*, pages 835–840.

Song, Y., Lee, K., Kim, D., and Chung, C. (2016). A Microcapsule-Type Fluorescent Probe for the Detection of Microcracks in Cementitious Materials. *Sensors and Actuators B: Chemical*, 222:1159–1165.

Soroushian, P., Nassar, R. U. D., and Balachandra, A. M. (2012). Piezo-Driven Self-Healing by Electrochemical Phenomena. *Journal of Intelligent Material Systems and Structures*, 24(4):441–453.

Spurgeon, S. (2008). Sliding mode observers: a survey. *International Journal of Systems Science*, 39(8):751–764.

Spurgeon, S. K. and Davies, R. (1993). A nonlinear control strategy for robust sliding mode performance in the presence of unmatched uncertainty. *International Journal of Control*, 57(5):1107–1123.

Su, C. and Stepanenko, Y. (2000). Robust Adaptive Control of a Class of Nonlinear Systems with Unknown Backlash-like Hysteresis. *IEEE Transactions on Automatic Control*, 45(12):2427 – 2432.

Tao, G. and Kokotovic, P. (1995a). Adaptive control of plants with unknown hystereses. *IEEE Transactions on Automatic Control*, 40(2):200–212.

Tao, G. and Kokotovic, P. (1995b). Adaptive control of system with unknown output backlash. *IEEE Transactions on Automatic Control*, 40(2):326–330.

Tasaltin, R. and Jafarov, E. (2000). Robust sliding-mode control for the uncertain MIMO aircraft model F-18. *IEEE Transactions on Aerospace and Electronic Systems*, 36(4):1127–1141.

Thakur, V. K. and Kessler, M. R. (2015). Self-healing polymer nanocomposite materials: A review. *Polymer*, 69(9):369–383.

Toohey, K., Sottos, N., Lewis, J., Moore, J., and SR White (2007). Self-Healing Materials with Microvascular Networks. *Nature Materials*, 6:581–585.

Toohey, K., Sottos, N., and White, S. (2009a). Characterization of Microvascular-Based Self-Healing Coatings. *Experimental Mechanics*, 49:707–717.

Toohey, K. S., Hansen, C. J., Lewis, J. A., White, S. R., and Sottos, N. R. (2009b). Delivery of Two-Part Self-Healing Chemistry via Microvascular Networks. *Advanced Functional Materials*, 19(9):1399–1405.

Trask, R., Bond, I., and Norris, C. (2011). Stimuli Triggered Deployment of Bio-Inspired Self-Healing Functionality. In *Conference on Smart Materials, Adaptive Structures and Intelligent Systems, Volume 2*, pages 753–758. ASME.

Trask, R. S., Norris, C. J., and Bond, I. P. (2013). Stimuli-Triggered Self-Healing Functionality in Advanced Fibre-Reinforced Composites. *Journal of Intelligent Material Systems and Structures*, 25(1):87–97.

Urdl, K., Kandelbauer, A., Kern, W., Müller, U., Thebault, M., and Zikulnig-Rusch, E. (2017). Self-healing of densely crosslinked thermoset polymers—a critical review. *Progress in Organic Coatings*, 104:232–249.

Utkin, V. (1977). Variable structure systems with sliding modes. *IEEE Transactions on Automatic Control*, 22(2):212–222.

Utkin, V. (1993). Sliding mode control design principles and applications to electric drives. *IEEE Transactions on Industrial Electronics*, 40(1):23–36.

Utkin, V. and Hoon Lee (2006). Chattering Problem in Sliding Mode Control Systems. In *International Workshop on Variable Structure Systems, 2006. VSS'06.*, pages 346–350. IEEE.

Vakil-Baghmisheh, M. and Peimani, M. (2008). Crack detection in beam-like structures using genetic algorithms. *Applied Soft COmputing*, 8(2):1150–1160.

Valenciaga, F. and Evangelista, C. (2010). Control design for an autonomous wind based hydrogen production system. *International Journal of Hydrogen Energy*, 35(11):5799–5807.

Venkatasubramanian, V. (2005). Prognostic and diagnostic monitoring of complex systems for product lifecycle management: Challenges and opportunities. *Computers & Chemical Engineering*, 29(6):1253–1263.

Wahab, M. M. A. and De Roeck, G. (1999). Damage detection in bridges using modal curvatures: application to a real damage scenario. *Journal of Sound and Vibration*, 226(2):217–235.

Wang, J., Ersan, Y., Boon, N., and Belie, N. D. (2016). Application of microorganisms in concrete: a promising sustainable strategy to improve concrete durability. *Applied microbiology and biotechnology*, 100(7):2993–3007.

Wang, Q. and Deng, X. (1999). Damage detection with spatial wavelets. *International Journal of Solids and Structures*, 36(23):3443–3468.

Wang, Q. and Wu, N. (2012). A Review on Structural Enhancement and Repair using Piezoelectric Materials and Shape Memory Alloys. *Smart Materials and Structures*, 21(1):013001.

Wang, X.-S., Su, C.-Y., and Hong, H. (2004). Robust Adaptive Control of a Class of Nonlinear Systems with Unknown Dead-zone. *Automatica*, 40(3):407–413.

Wei, Z., Yang, J. H., Zhou, J., Xu, F., Zr?nyi, M., Dussault, P. H., Osada, Y., Chen, Y. M., Vunjak-Novakovic, G., Kowollik, C. B., and Stang, P. J. (2014). Self-healing gels based on constitutional dynamic chemistry and their potential applications. *Chem. Soc. Rev.*, 43(23):8114–8131.

Wen, Z., Chen, J., Wang, H., Zhong, S., Hu, Y., Wang, Z., and Zhang, Q. (2016). Abalone water-soluble matrix for self-healing biomineralization of tooth defects. *Materials Science and Engineering: C*, 67:182–187.

Wertzberger, B. E., Steere, J. T., Pfeifer, R. M., Nensel, M. A., Latta, M. A., and Gross, S. M. (2010). Physical Characterization of a Self-Healing Dental Restorative Material. *Journal of Applied Polymer Science*, 118(1):428–434.

White, S. R., Sottos, N. R., Geubelle, P. H., Moore, J. S., Kessler, M. R., Sriram, S. R., Brown, E. N., and Viswanathan, S. (2001). Autonomic Healing of Polymer Composites. *Nature*, 409(6822):794–797.

Wu, J., Weir, M., Melo, M., Strassler, H., and Xu, H. (2016a). Effects of water-aging on self-healing dental composite containing microcapsules. *Journal of dentistry*, 47:86–93.

Wu, J., Weir, M. D., Melo, M. A. S., and Xu, H. H. (2015). Development of novel self-healing and antibacterial dental composite containing calcium phosphate nanoparticles. *Journal of Dentistry*, 43(3):317–326.

Wu, J., Weir, M. D., Zhang, Q., Zhou, C., Melo, M. A. S., and Xu, H. H. (2016b). Novel Self-Healing Dental Resin with Microcapsules of Polymerizable Triethylene Glycol Dimethacrylate and N, N-Dihydroxyethyl-P-Toluidine. *Dental Materials*, 32(2):294–304.

Yan, Y. and Yam, L. (2002). Online Detection of Crack Damage in Composite Plates using Embedded Piezoelectric Actuators/Sensors and Wavelet Analysis. *Composite structures*, 58(1):29–38.

Ye, X. J., Song, Y. X., Zhu, Y., Yang, G. C., Rong, M. Z., and Zhang, M. Q. (2014). Self-Healing Epoxy with Ultrafast and Heat-Resistant Healing System Processable at Elevated Temperature. *Composites Science and Technology*, 104:40–46.

Yeom, C., Kim, Y., and Lee, J. (2002). Microencapsulation of Water-Soluble Herbicide by Interfacial Reaction. II. Release properties of Microcapsules. *Journal of Applied Polymer Science*, 84(5):1025–1034.

Yeom, C. and Oh, S. (2000). Microencapsulation of Water-Soluble Herbicide by Interfacial Reaction. I. Characterization of Microencapsulation. *Journal of Applied Polymer Science*, 78(9):1645–1655.

Young, K., Utkin, V., and Ozguner, U. (1996). A control engineer's guide to sliding mode control. *Variable Structure Systems, 1996. VSS'96. Proceedings., 1996 IEEE International Workshop on*, pages 1–14.

Yuan, C., Rong, M. Z., Zhang, M. Q., Zhang, Z. P., and Yuan, Y. C. (2011). Self-Healing of Polymers via Synchronous Covalent Bond Fission/Radical Recombination. *Chemistry of Materials*, 23(22):5076–5081.

Yuan, Y. C., Yin, T., Rong, M. Z., and Zhang, M. Q. (2008). Self Healing in Polymers and Polymer Composites. Concepts, Realization and Outlook: A Review. *Express Polymer Letters*, 2(4):238–250.

Yue, H.-B., Fernández-Blázquez, J. P., Beneito, D. F., and Vilatela, J. J. (2014). Real Time Monitoring of Click Chemistry Self-Healing in Polymer Composites. *Journal of Materials Chemistry A*, 2(11):3881.

Zemskov, S. V., Jonkers, H. M., and Vermolen, F. J. (2012). A Mathematical Model for Bacterial Self-Healing of Cracks in Concrete. *Journal of Intelligent Material Systems and Structures*, 25(1):4–12.

Zhang Yan and Utkin, V. (2002). Sliding mode observers for electric machines-an overview. In *IEEE 2002 28th Annual Conference of the Industrial Electronics Society. IECON 02*, volume 3, pages 1842–1847.

Zheng, H., Li, Z., and Chen, X. (2002). Gear fault diagnosis based on continous wavelet transform. *Mechanical Systems and Signal Processing*, 16(2-3):447–457.

Zheng, J., Wang, H., Man, Z., Jin, J., and Fu, M. (2015). Robust Motion Control of a Linear Motor Positioner Using Fast Nonsingular Terminal Sliding Mode. *IEEE/ASME Transactions on Mechatronics*, 20(4):1743–1752.

Zhong, N. and Post, W. (2015). Self-Repair of Structural and Functional Composites with Intrinsically Self-Healing Polymer Matrices: A Review. *Composites Part A: Applied Science and Manufacturing*, 69:226–239.

Zhonghua, W., Bo, Y., Lin, C., and Shusheng, Z. (2006). Robust adaptive deadzone compensation of DC servo system. In *IEE Proceedings - Control Theory and Applications*, volume 153, pages 709–713.

Zhou, J., Er, M., and Veluvolu, K. (2006). Adaptive output control of nonlinear time-delayed systems with uncertain dead-zone input. In *American Control Conference, 2006. IEEE*.

Zhou, T. and Francois, B. (2009). Modeling and control design of hydrogen production process for an active hydrogen/wind hybrid power system. *International Journal of Hydrogen Energy*, 34(1):21–30.

Zhu, Y., Yin, T., Ren, J., Liu, C., Fu, D., and Ge, L. (2016). Self-Healing Polyelectrolyte Multilayer Composite Film with Microcapsules. *RSC Advances*, 6:12100–12106.

Appendix A

Proof of Stability

Proof. The Lyapunov candidate W is given by Equation (A.1).

$$W(t) = \frac{1}{2}\left(\frac{1}{m}s_\epsilon^2 + \frac{1}{\gamma}\tilde{\phi}^2 + \frac{1}{\Gamma}\tilde{V}_{p^r}^2\right) \tag{A.1}$$

The derivative of W along the system trajectory is expressed in Equation (A.3).

$$W(t) = \frac{1}{2}\left(\frac{1}{m}s_\epsilon^2 + \frac{1}{\gamma}\tilde{\phi}^2 + \frac{1}{\Gamma}\tilde{V}^2\right) \tag{A.2}$$

$$\dot{W}(t) = \frac{1}{m}s_\epsilon\dot{s} + \frac{1}{\gamma}\tilde{\phi}\dot{\tilde{\phi}} + \frac{1}{\Gamma}\tilde{V}\dot{\tilde{V}} \tag{A.3}$$

Equation (3.26) and Equation (3.27) are substituted into Equation (A.3) to give Equation (A.4).

$$\begin{aligned}\dot{W}(t) = \quad & -\lambda_c K_d s_\epsilon s + \lambda_c s_\epsilon\left(V(t) - \hat{V} + \hat{\phi}\dot{Q}_d(t) - k^* sat\left(\tfrac{s}{\epsilon}\right)\right) \\ & +\lambda_c s_\epsilon\left(\tfrac{\Delta I(t)}{m} - \phi\dot{Q}_d(t)\right) + \tfrac{1}{\gamma}\tilde{\phi}\dot{\tilde{\phi}} + \tfrac{1}{\Gamma}\tilde{V}\dot{\tilde{V}}\end{aligned} \tag{A.4}$$

From Equation (A.4), the adaptive laws become Equation (A.5) and Equation (A.6).

$$\dot{\tilde{\phi}} = -\gamma\lambda_c\dot{Q}_d(t)s_\epsilon \tag{A.5}$$

$$\dot{\tilde{V}} = \lambda_c\Gamma s_\epsilon \tag{A.6}$$

Substituting the adaptive laws Equation (A.5) and Equation (A.6) into Equation (A.4) gives the expression in Equation (A.7).

$$\dot{W}(t) = -\lambda_c K_d s_\epsilon s - \lambda_c k^* s_\epsilon sat\left(\frac{s}{\epsilon}\right) + \frac{\Delta I(t)}{m}\lambda_c s_\epsilon \tag{A.7}$$

$$\dot{W}(t) = -\lambda_c K_d s_\epsilon \left(s_\epsilon + \epsilon sat\left(\frac{s}{\epsilon}\right)\right) - \lambda_c k^* s_\epsilon sat\left(\frac{s}{\epsilon}\right) + \frac{\Delta I(t)}{m}\lambda_c s_\epsilon \tag{A.8}$$

When $|s| \leq \epsilon$, $|s_\epsilon| = 0$ and Equation (A.8) is zero Equation (A.9).

$$\dot{W}(t) = 0 \qquad \forall |s| \leq \epsilon \tag{A.9}$$

When $|s| > \epsilon$, $|s_\epsilon| = s_\epsilon sat(s/\epsilon)$. By also taking into account $k^* \geq \rho/m_{min}$, Equation (A.8) is expressed to give Equation (A.12).

$$\dot{W}(t) = -\lambda_c K_d s_\epsilon^2 - (K_d\epsilon + k^*)\lambda_c |s_\epsilon| + \frac{\Delta I(t)}{m}\lambda_c s_\epsilon \tag{A.10}$$

$$\dot{W}(t) \leq -\lambda_c K_d s_\epsilon^2 - K_d\epsilon\lambda_c |s_\epsilon| - \left(k^* - \frac{\Delta I(t)}{m}\right)\lambda_c |s_\epsilon| \tag{A.11}$$

$$\dot{W}(t) \leq -\lambda_c K_d s_\epsilon^2 \qquad \forall |s| > \epsilon \tag{A.12}$$

The above formulations in Equation (A.9) and Equation (A.12) indicate that s_ϵ, $\tilde{\phi}$ and $\tilde{V}$ are globally bounded. This also means that $s(t)$ is bounded and the control design guarantees that the system trajectory will converge to the sliding mode.

Appendix B

Simulation Results of Active Self-healing

The following figures are the simulation results of the active self-healing proposed in Chapter 3.

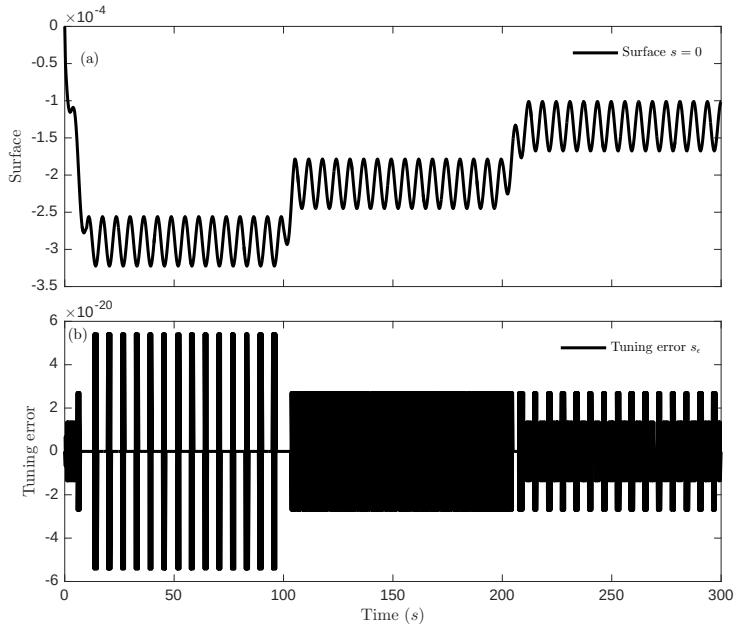

Figure B.1: (a) The sliding surface $s = 0$ of the adaptive Sliding mode controller. (b) The tuning error s_ϵ used during the control design in place of the sliding surface s to avoid chattering.

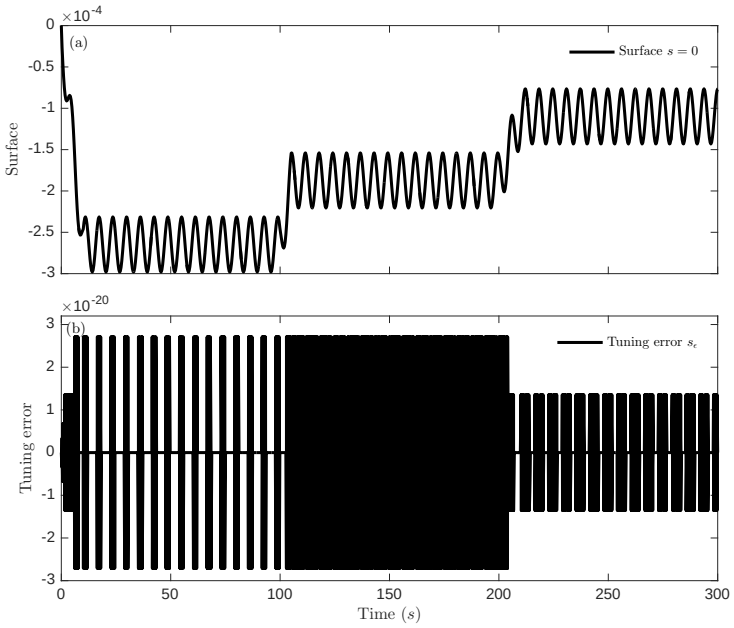

Figure B.2: (a) The sliding surface $s = 0$ of the adaptive Sliding mode controller in constant environmental conditions. (b) The tuning error s_ϵ used during the control design in place of the sliding surface s to avoid chattering.

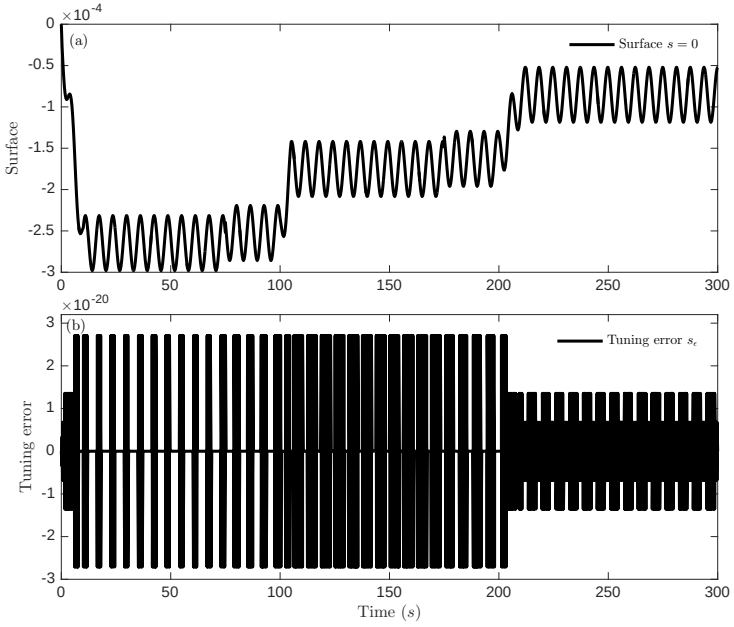

Figure B.3: (a) The sliding surface $s = 0$ of the adaptive Sliding mode controller in varying environmental conditions. (b) The tuning error s_ϵ used during the control design in place of the sliding surface s to avoid chattering.

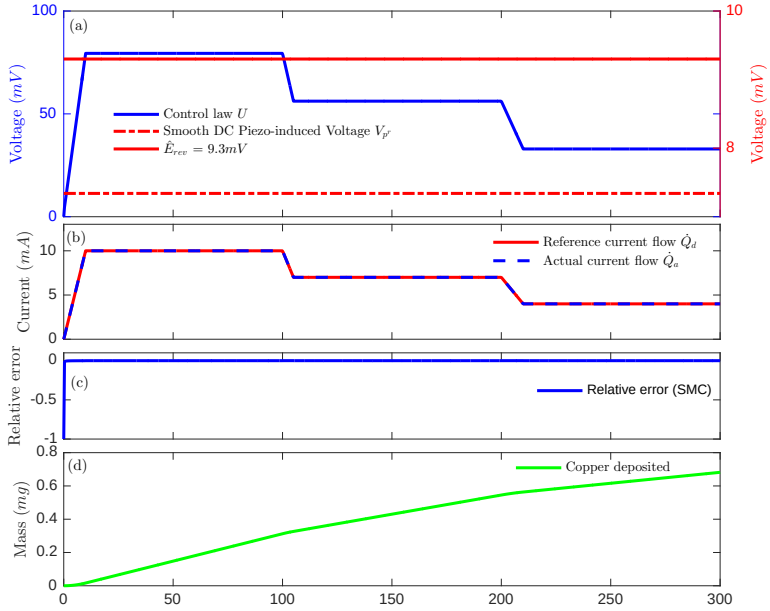

Figure B.4: Adaptive SMC applied to a case where the composite material is subjected to constant load input in the presence of uncertainties. This depicts a material exposed to constant environmental conditions. (a) The piezo-induced voltage is insufficient to drive the healing process since $V_{p^r} < \hat{E}_{rev}$. The feedback adaptive controller contribute an external input that ensures that the current flow during electrolysis tracks the desired performance. (b) The actual current flow during electrolysis matches a defined reference current flow. The reference and actual current represent the damage rate and healing rate respectively. (c) Relative error of the adaptive SMC defined as the difference between the actual and reference current divided by the reference current. (d) The equivalent mass deposited over time for the closed loop active self-healing process.

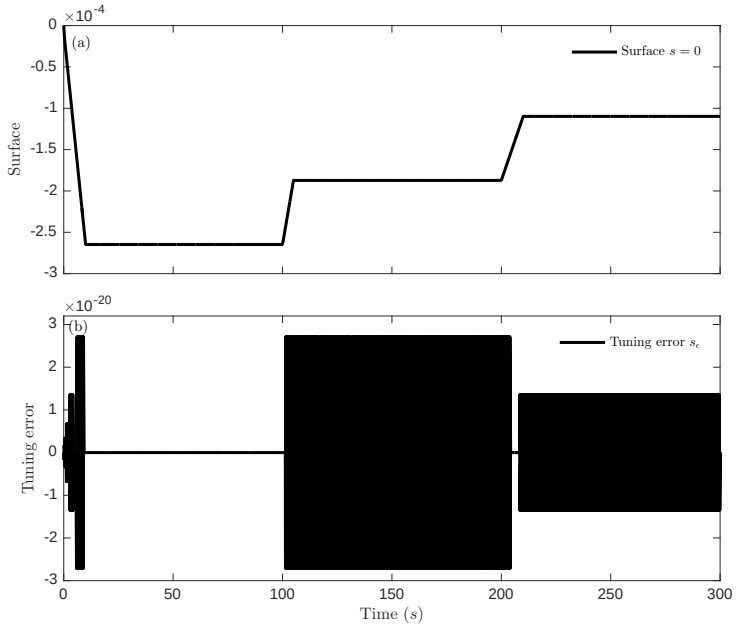

Figure B.5: (a) The sliding surface $s = 0$ of the adaptive Sliding mode controller in constant environmental conditions. (b) The tuning error s_ϵ used during the control design in place of the sliding surface s to avoid chattering.

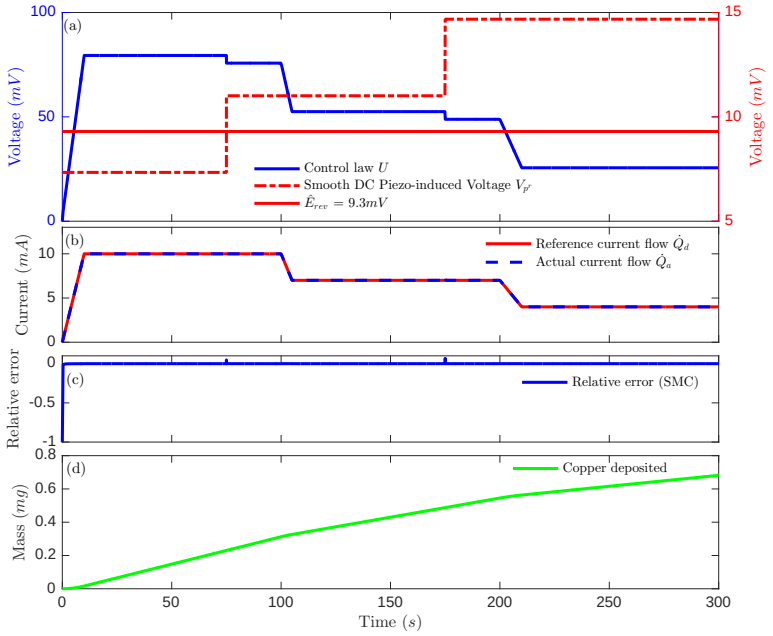

Figure B.6: Adaptive SMC applied to a case where the composite material is subjected to different load inputs at different time instants and in the present of uncertainties. This depicts a material exposed to varying environmental conditions. (a) The piezo-induced voltage is insufficient to drive the healing process during the first 75 seconds since $V_{pr} < \hat{E}_{rev}$. The feedback adaptive controller contributes an input and ensures that the current flow during electrolysis tracks the desired performance. (b) The actual current flow during electrolysis matches a defined reference current flow. The reference and actual current represent the damage rate and healing rate respectively. (c) Relative error of the adaptive SMC defined as the difference between the actual and reference current divided by the reference current. (d) The equivalent mass deposited over time for the closed loop active self-healing process.

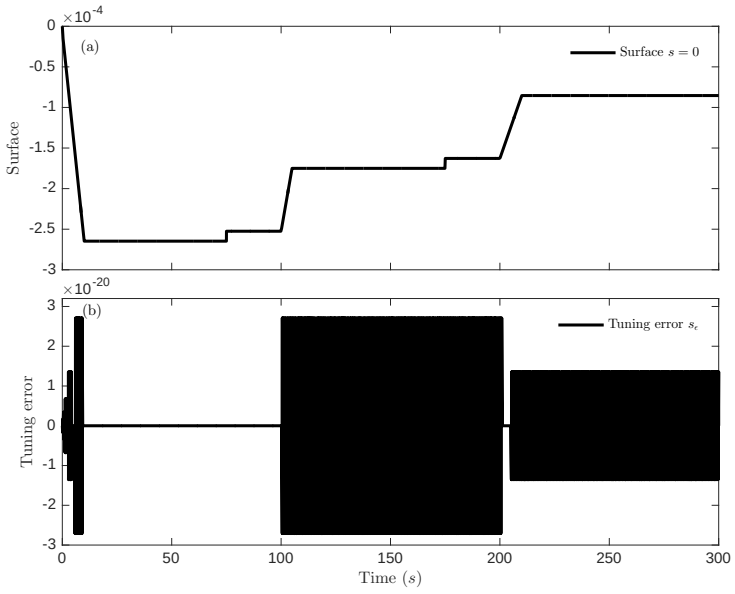

Figure B.7: (a) The sliding surface $s = 0$ of the adaptive Sliding mode controller in varying environmental conditions. (b) The tuning error s_ϵ used during the control design in place of the sliding surface s to avoid chattering.

Appendix C

Beam Preliminary Mathematics

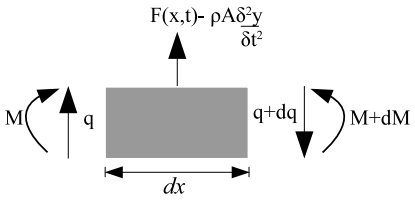

Figure C.1: An element of a beam acted upon by forces.

Consider the forces acting on an element of a beam of length dx in Figure C.1. $F(x,t)$, q, and M represent the concentrated force, shear force and moment acting on the element respectively. Equation (C.1) gives the balanced moments.

$$M - f(x,t)dx\frac{dx}{2} - (M + dM) + (q + dq)dx = 0 \tag{C.1}$$

Given that $dq = \frac{\partial q}{\partial x}dx$ and $dM = \frac{\partial M}{\partial x}dx$, Equation (C.1) can be expressed as:

$$-f(x,t)\frac{dx^2}{2} - \frac{\partial M}{\partial x}dx + qdx + \frac{\partial q}{\partial x}dx^2 = 0 \tag{C.2}$$

Disregarding the second order terms of dx gives:

$$q = \frac{\partial M}{\partial x} \tag{C.3}$$

Equation (C.4) gives the balance forces in the vertical direction, given the cross sectional area A, density ρ, shear force q, moment of inertia I and Young's modulus E.

$$F(x,t)dx + q - (q+dq) - \rho A dx \frac{\partial^2 y(x,t)}{\partial t^2} = 0 \tag{C.4}$$

$$F(x,t)dx - \frac{\partial q}{\partial x}dx - \rho A dx \frac{\partial^2 y(x,t)}{\partial t^2} = 0 \tag{C.5}$$

$$F(x,t) - \frac{\partial q}{\partial x} - \rho A \frac{\partial^2 y(x,t)}{\partial t^2} = 0 \tag{C.6}$$

Substituting Equation (C.3) in Equation (C.6) gives Equation (C.7).

$$F(x,t) = \frac{\partial}{\partial x}\Big(\frac{\partial M}{\partial x}\Big) + \rho A \frac{\partial^2 y(x,t)}{\partial t^2} \tag{C.7}$$

Since $M = EI\frac{\partial^2 y(x,t)}{\partial x^2}$, Equation (C.7) becomes Equation (C.8).

$$F(x,t) = EI\frac{\partial^4 y(x,t)}{\partial x^4} + \rho A \frac{\partial^2 y(x,t)}{\partial t^2} \tag{C.8}$$

When $F(x,t) = 0$, Equation (C.8) can be written as Equation (C.9).

$$EI\frac{\partial^4 y(x,t)}{\partial x^4} + \rho A \frac{\partial^2 y(x,t)}{\partial t^2} = 0 \tag{C.9}$$

Equation (C.8) and Equation (C.9) are the Euler-Bernoulli beam's differential equations for a forced and free vibration respectively, while neglecting damping.

Given the displacement of a beam at x location as $y(x,t) = Y(x)sin(\omega t)$, the following expressions are derived from Equation (C.9) to express the general solution.

$$\frac{\partial^4 Y(x)}{\partial x^4} - \frac{\rho A \omega^2}{EI} Y(x) = 0 \tag{C.10}$$

The general solution for the fourth order ordinary differential equation becomes:

$$Y(x) = \eta_1 cosh\left(\lambda\frac{x}{L}\right) + \eta_2 sinh\left(\lambda\frac{x}{L}\right) + \eta_3 cos\left(\lambda\frac{x}{L}\right) + \eta_4 sin\left(\lambda\frac{x}{L}\right) \tag{C.11}$$

Where $\lambda = \sqrt[4]{\omega^2 \rho A L^4 / EI}$.

Appendix D

Other Simulation Results of Crack diagnosis

Cantilever beam parameters

The following represents the fault diagnosis parameters used in Chapter 4 to evaluate the crack depth:

$$p = 0.001, \quad min\left(\frac{N}{l_{est}^{p}}\right) = 0.448260839514567$$

$$max\left(\frac{N}{l_{est}^{p}}\right) = 6.854110199159990 \tag{D.1}$$

$$\zeta = \begin{bmatrix} -0.00759980609749430 & 0.00832618944773892 & 0.0271956645747414 & 0.0393925075913558 \\ 0.00700148483014249 & 0.00363881893359507 & 0.0339472366522346 & -0.277785191084162 \\ -0.328746524887996 & -0.431469259177307 & -0.0247307359288862 & -0.00766393683413206 \\ -0.0108751062429764 & 2.00663053781348 & 1.74706886637574 & 2.85655063224483 \\ 0.0346856626431481 & 0.0173092954273048 & -0.410118174343845 & -4.85936664784864 \\ -3.50347550929267 & -11.9171728494472 & 0.00433895303359672 & -0.0300621203306145 \\ 1.84527983074886 & 0 & 0 & 31.0061038368959 & -0.0900378848550543 & 0.0356592886451499 \\ -4.02851417549175 & 11.2335887743531 & 0 & -47.4746976509623 & 0.146816839904475 \\ -0.0289424366038142 & 4.32005229973420 & 0 & 0 & 34.9672153576652 & -0.122983721284062 \\ 0.0162944535149795 & 0 & -15.8193661633137 & 0 & 0 & 0.0591028971195407 & -0.00637157444294319 \\ -6.17764269732311 & 0 & 0 & -12.1308856361644 & -0.0150982312704148 & 0.00170021015480035 \\ 7.80336110982638 & 0 & 0 & 0 & 0.00113826177211712 & -0.000295623928407927 & -4.29188049825062 \\ 0 & 0 & 0 & 0.000305850286591823 & 3.02140394729395 \times 10^{-05} & 0.924541679195303 \\ 14.5141765439079 & 0 & 3.68575991045567 & -5.53494346103474 \times 10^{-05} \\ -1.37784853516319 \times 10^{-06} \end{bmatrix}^{T} \tag{D.2}$$

Figures D.1 - D.6 depict the deflection and curvature of an intact and cracked cantilever beam.

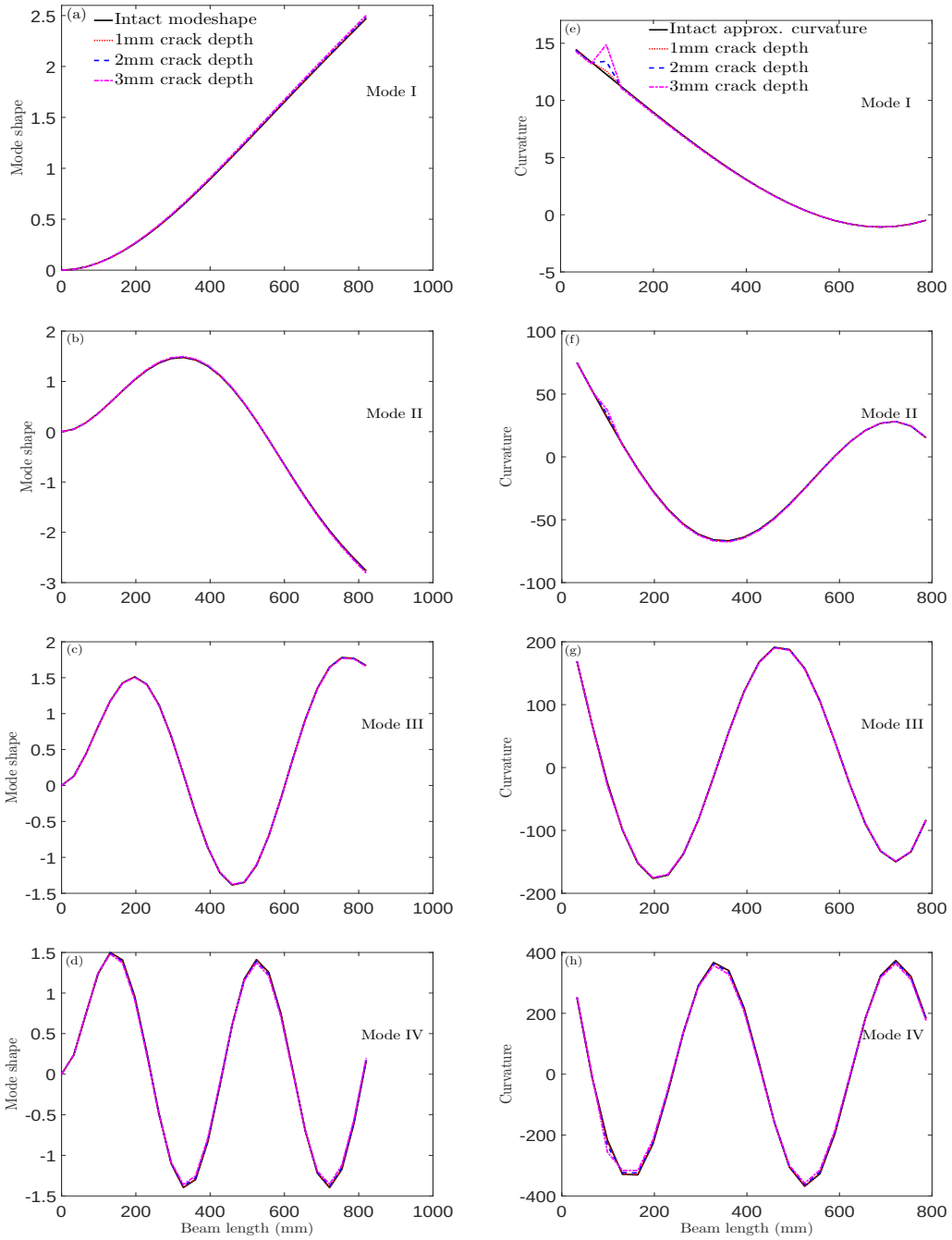

Figure D.1: Deflections (a-d) and curvatures (e-h) of the first four modes of an intact and damaged cantilever beam of different crack depths located at 98.4mm.

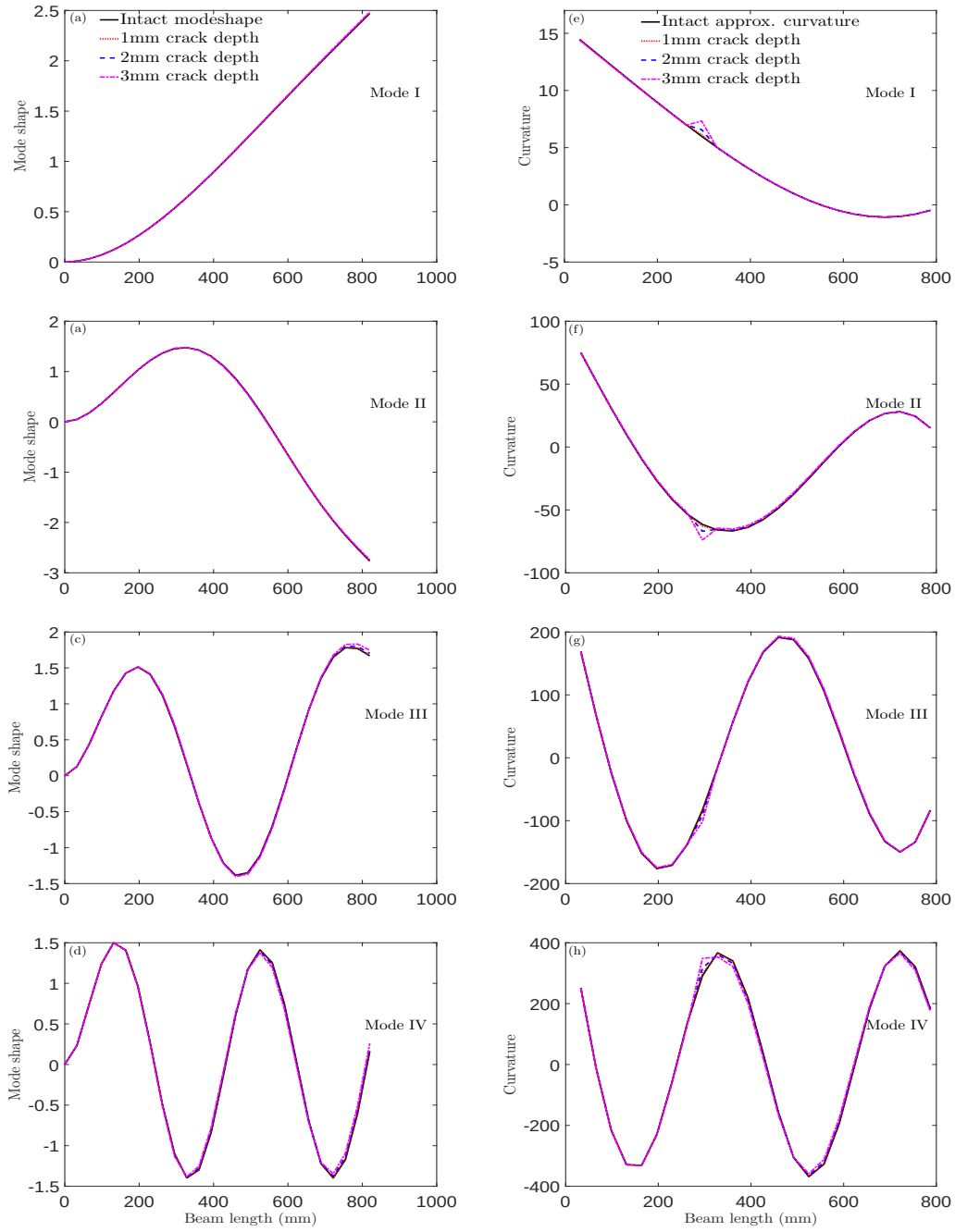

Figure D.2: Deflections (a-d) and curvatures (e-h) of the first four modes of an intact and damaged cantilever beam of different crack depths at location 295.2mm.

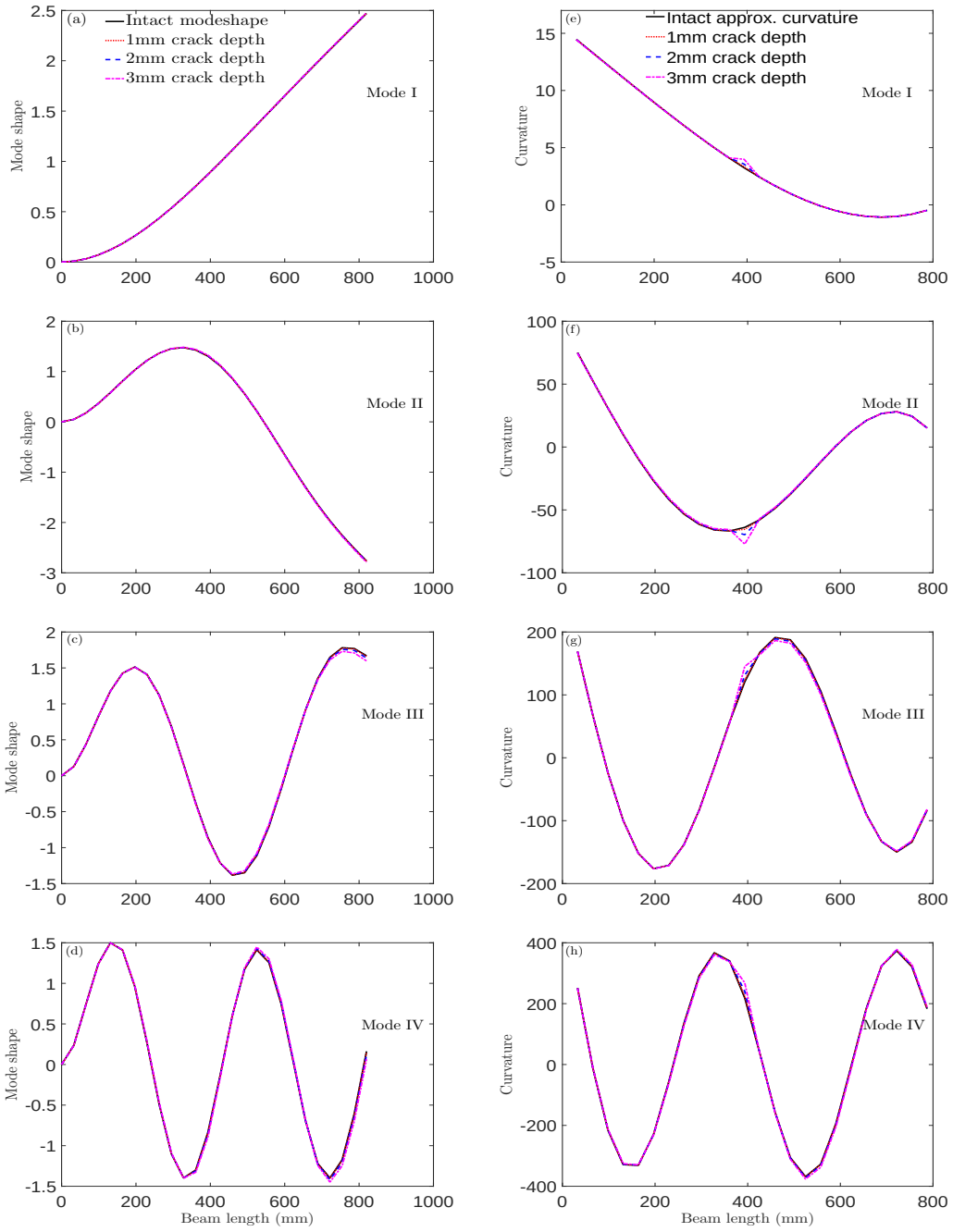

Figure D.3: Deflections (a-d) and curvatures (e-h) of the first four modes of an intact and damaged cantilever beam of different crack depths located at 393.6mm.

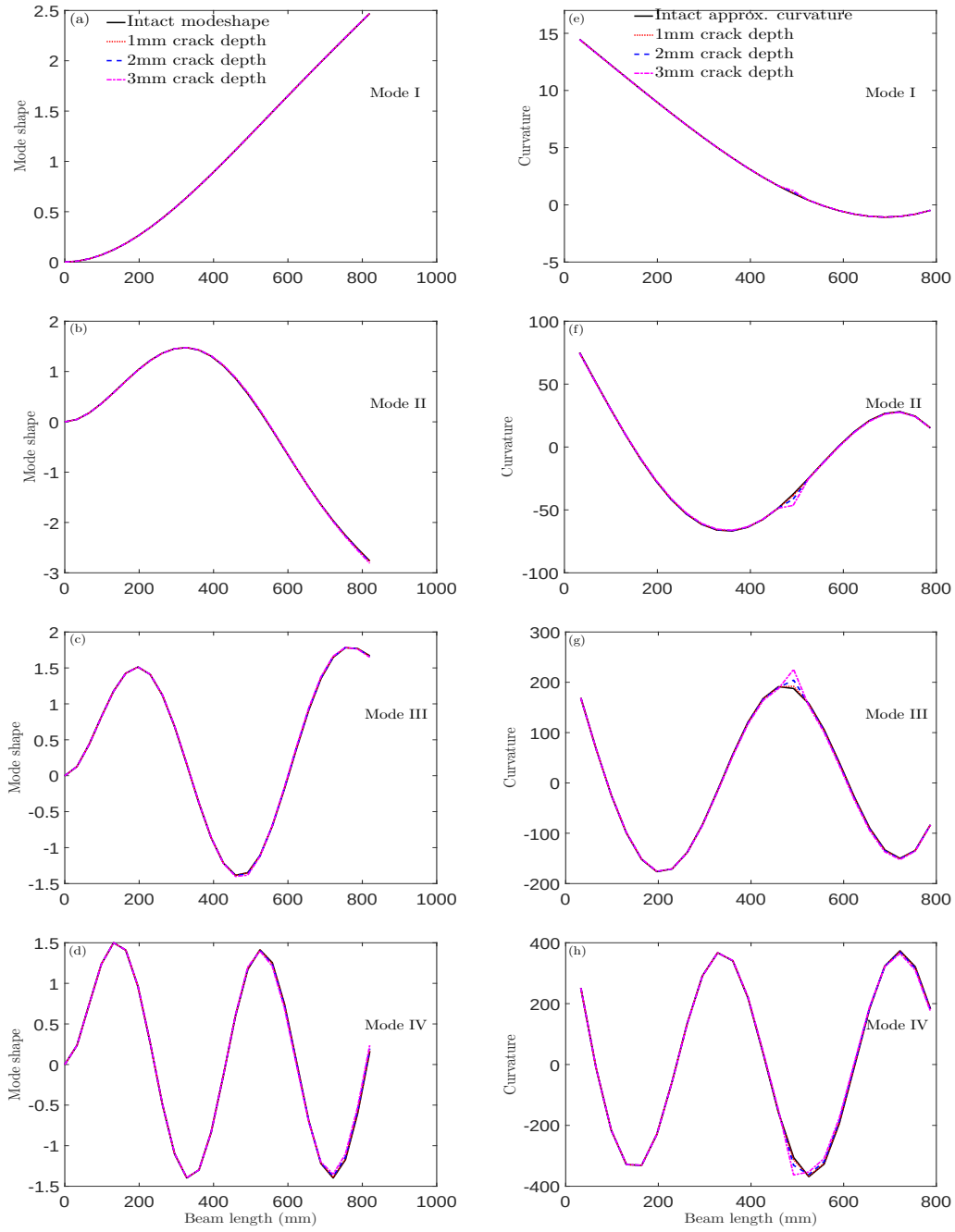

Figure D.4: Deflections (a-d) and curvatures (e-h) of the first four modes of an intact and damaged cantilever beam of different crack depths located at 492mm.

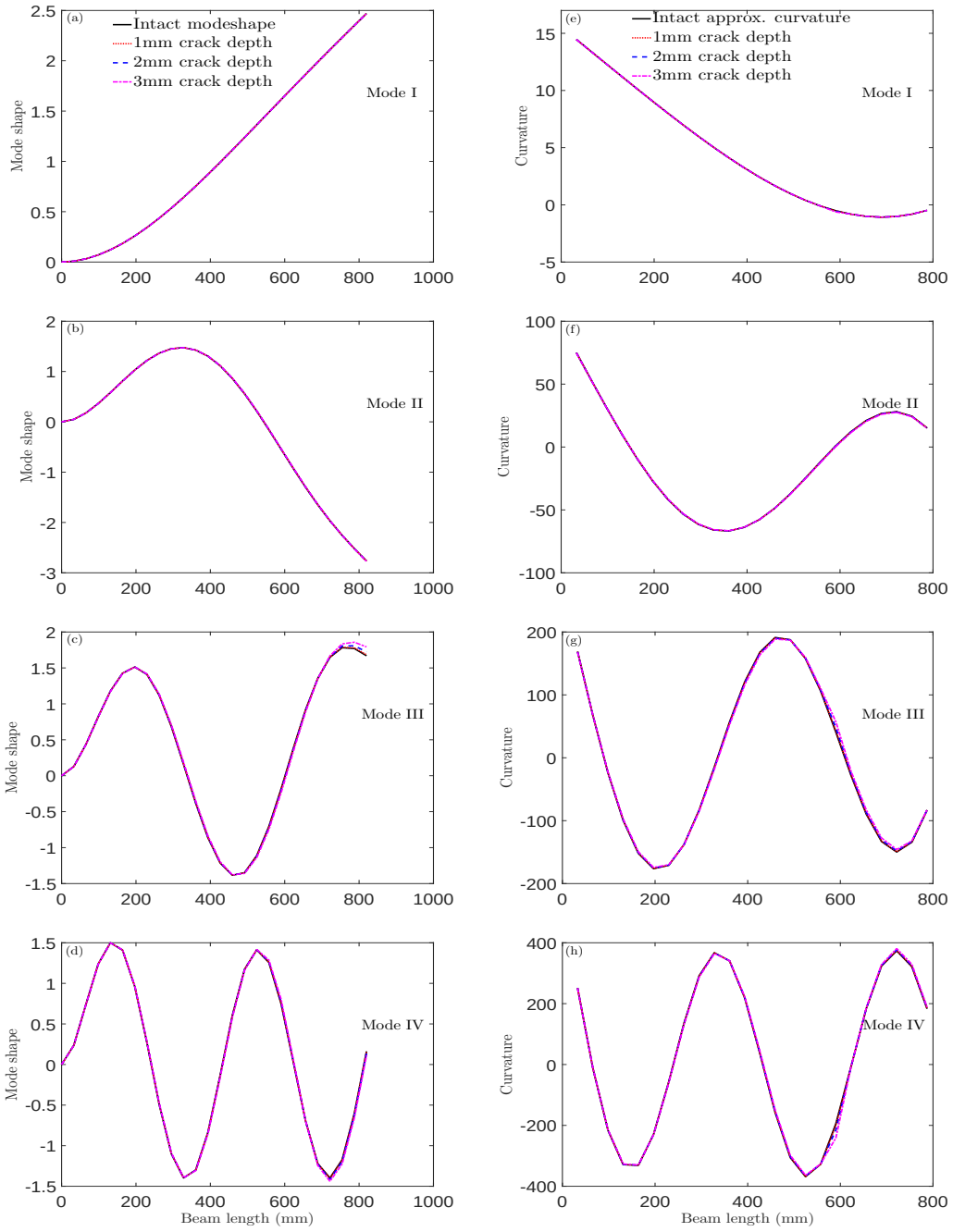

Figure D.5: Deflections (a-d) and curvatures (e-h) of the first four modes of an intact and damaged cantilever beam of different crack depths located at 590.4mm.

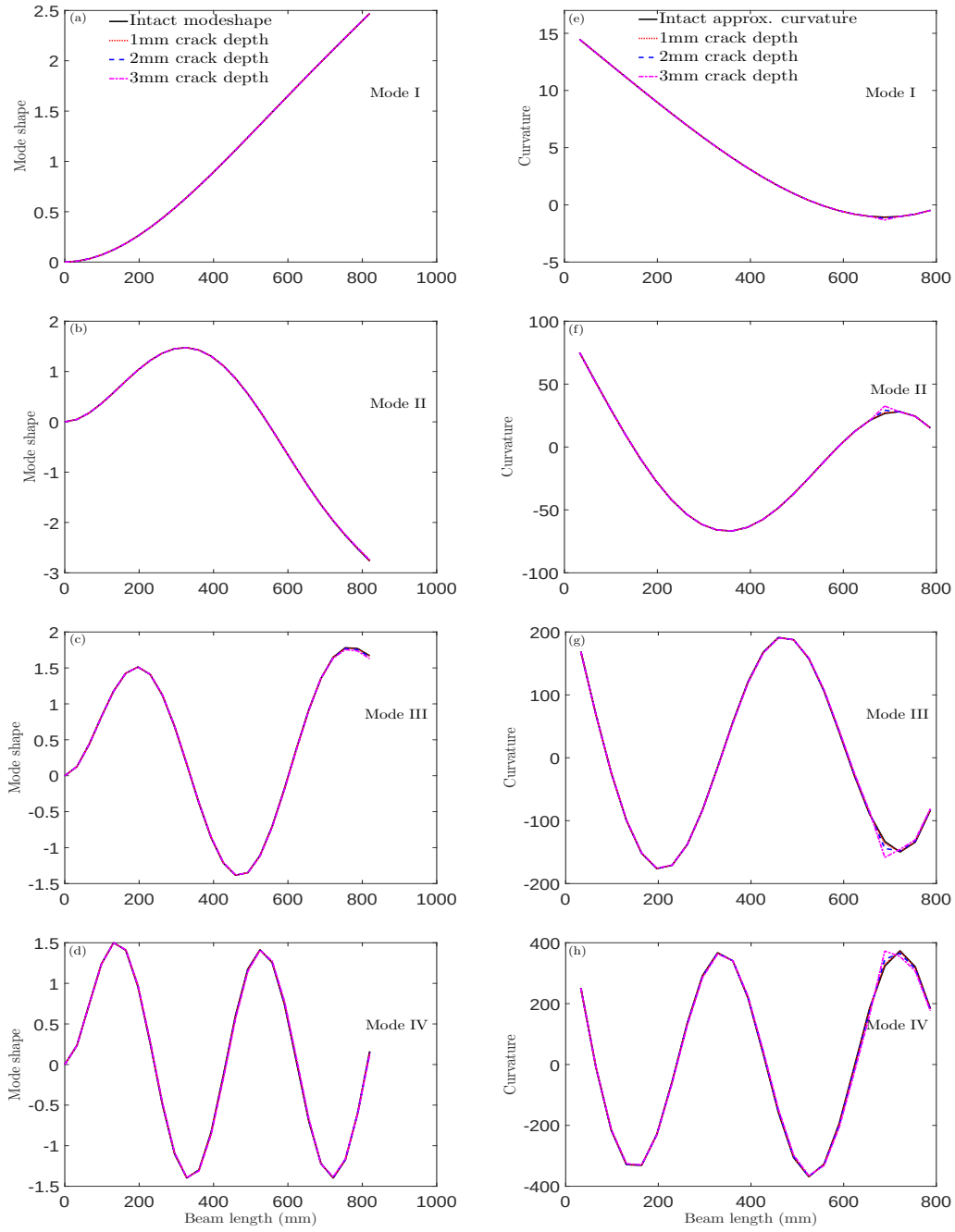

Figure D.6: Deflection (a-d) and radius of curvature (e-h) of the first four modes of an intact and damaged cantilever beam of different crack depths located at 688.8mm.

Fixed beam

An aluminium fixed beam of dimensions $820mm$ by $20mm$ by $10mm$ is modelled using a finite element model with 24 elements. The beam's mechanical properties include Young's modulus of 70 GPA, density of 2700 kg/m^3 and Poisson ratio of 0.3. Equation (D.3) - (D.4) are the parameters used for the crack diagnosis.

$$p = 0.001, \quad min\left(\frac{N}{l_{est}^{p}}\right) = 0.428667496955623$$
$$max\left(\frac{N}{l_{est}^{p}}\right) = 6.974021712690253, \quad r = 12 \tag{D.3}$$

$$\zeta = \begin{bmatrix} -0.00759980609749430 & 0.00832618944773892 & 0.0271956645747414 & 0.0393925075913558 \\ 0.00700148483014249 & 0.00363881893359507 & 0.0339472366522346 & -0.277785191084162 \\ -0.328746524887996 & -0.431469259177307 & -0.0247307359288862 & -0.00766393683413206 \\ -0.0108751062429764 & 2.00663053781348 & 1.74706886637574 & 2.85655063224483 \\ 0.0346856626431481 & 0.0173092954273048 & -0.410118174343845 & -4.85936664784864 \\ -3.50347550929267 & -11.9171728494472 & 0.00433895303359672 & -0.0300621203306145 \\ 1.84527983074886 & 0 & 0 & 31.0061038368959 & -0.0900378848550543 & 0.0356592886451499 \\ -4.02851417549175 & 11.2335887743531 & 0 & -47.4746976509623 & 0.146816839904475 \\ -0.0289424366038142 & 4.32005229973420 & 0 & 0 & 34.9672153576652 & -0.122983721284062 \\ 0.0162944535149795 & 0 & -15.8193661633137 & 0 & 0 & 0.0591028971195407 & -0.00637157444294319 \\ -6.17764269732311 & 0 & 0 & -12.1308856361644 & -0.0150982312704148 & 0.00170021015480035 \\ 7.80336110982638 & 0 & 0 & 0 & 0.00113826177211712 & -0.000295623928407927 & -4.29188049825062 \\ 0 & 0 & 0 & 0.000305850286591823 & 3.02140394729395 \times 10^{-05} & 0.924541679195303 & 14.5141765439079 \\ 0 & 3.68575991045567 & -5.53494346103474 \times 10^{-05} & -1.37784853516319 \times 10^{-06} \end{bmatrix}^{T} \tag{D.4}$$

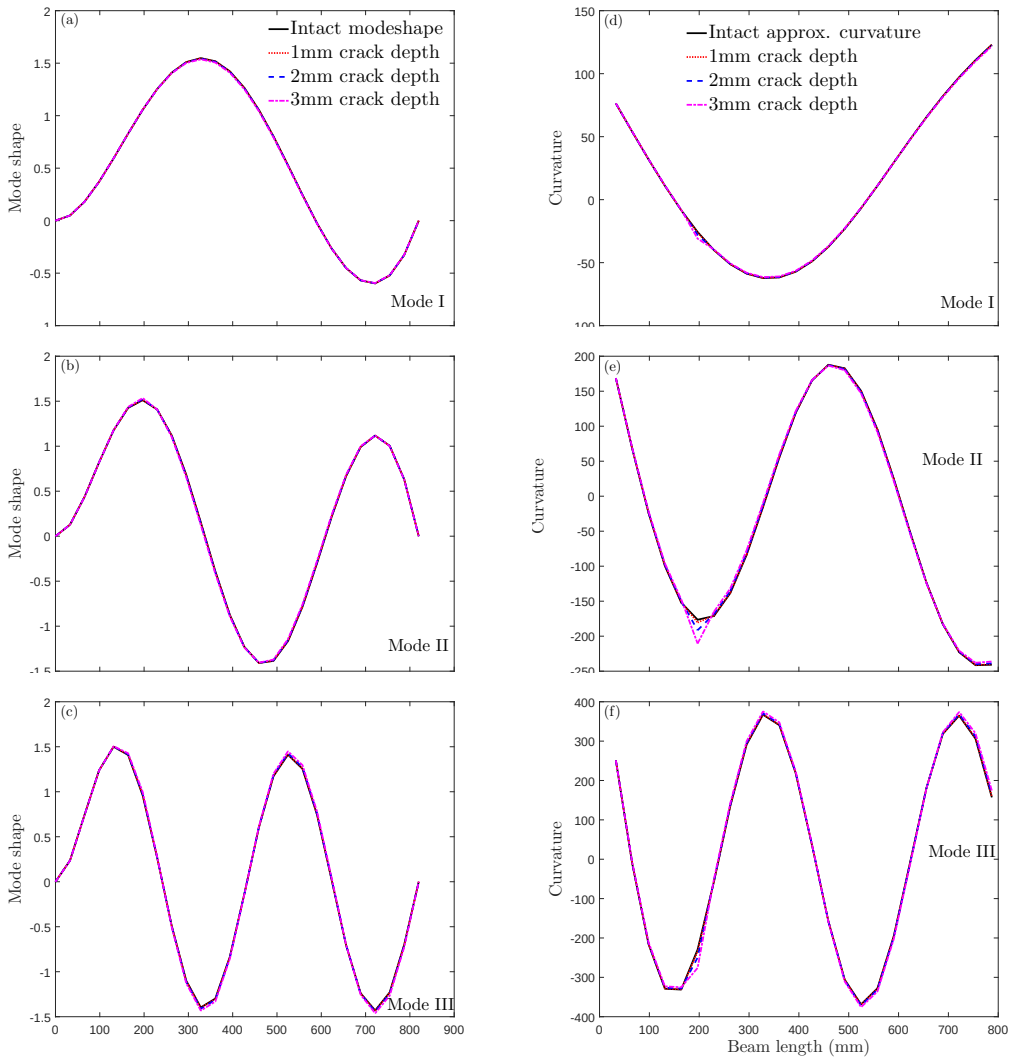

Figure D.7: Modeshapes (a-c) and curvatures (d-f) of the first four modes of an intact and damaged fixed beam of different crack depths located at 196.8mm.

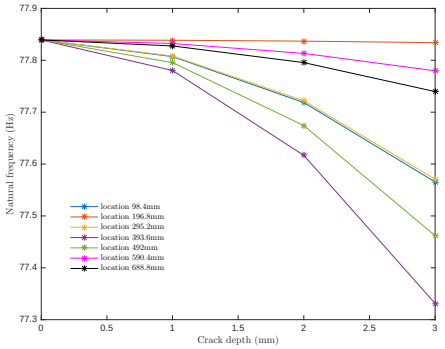

(a) Mode I

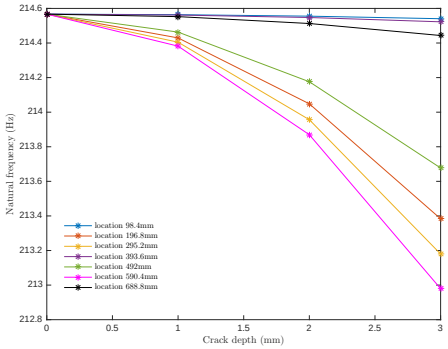

(b) Mode II

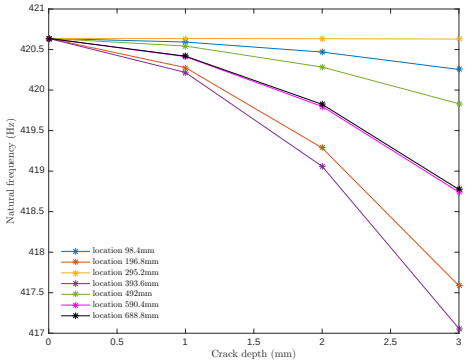

(c) Mode III

Figure D.8: Natural frequency of the first four modes of an intact and a damaged fixed beam of different crack depths at different crack locations.

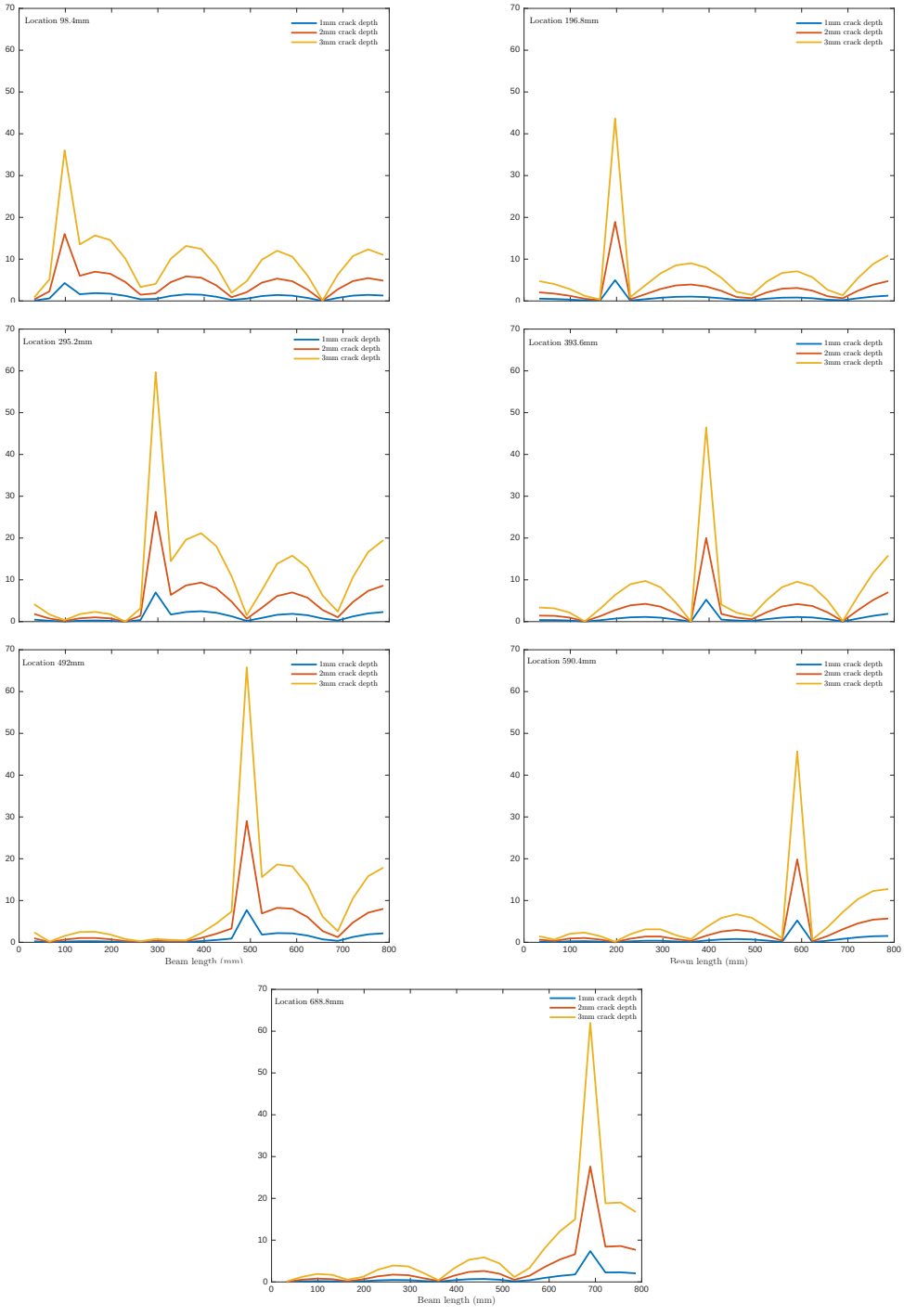

Figure D.9: Difference between the unique features extracted by POD from an intact and the cracked beam curvatures of all crack depths at different locations.

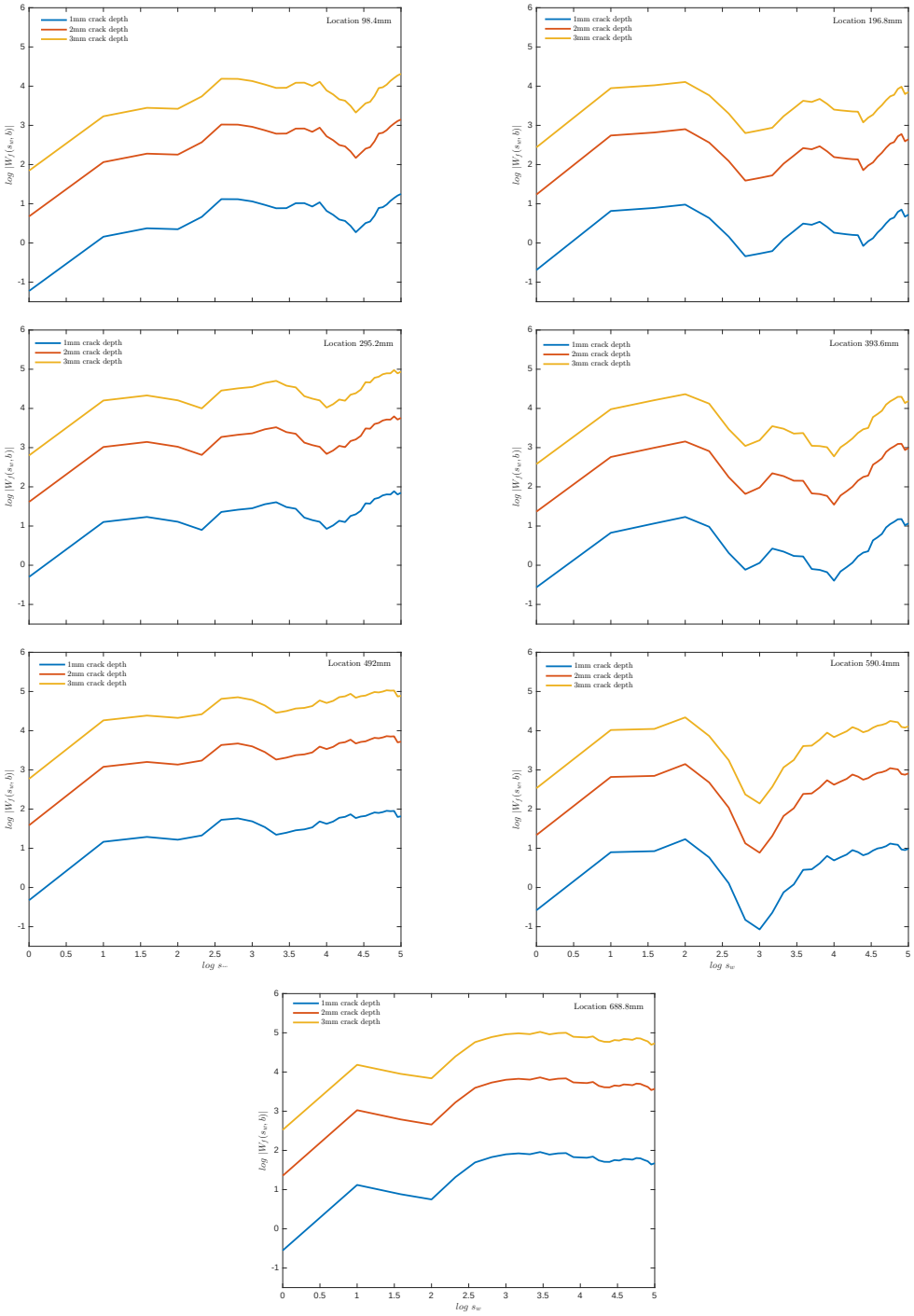

Figure D.10: Logarithm plot of the scale and Wavelet maxima of different crack depths at the same location.

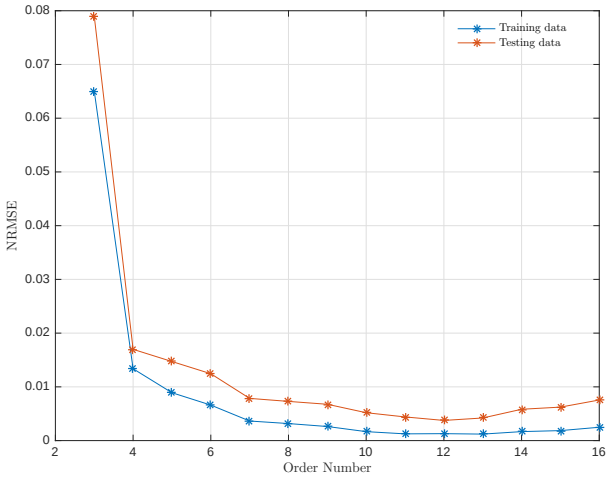

Figure D.11: Cross-validation: The normalised root mean square (NRMSE) of different polynomial order used to select the order number. This step avoids under and over fitting.

Appendix E

Other Simulation Results of Integrated Sensing, Diagnosis and Active Self-healing

The following parameters are used in Chapter 5 to evaluate the integrated sensing, diagnosis and active self-healing. The results are also presented in this appendix.

$$min\left(\frac{N}{l_{est}^{p}}\right) = \begin{cases} 0.225288903540750 & \text{if } a > 0.75mm \\ 0.006407108948543 & \text{if } a > 0.1mm \ \& \ a \leq 0.75mm \\ 0.001038031929001 & \text{if } a > 0.03mm \ \& \ a \leq 0.1mm \\ 3.319022474065476 \times 10^{-05} & \text{if } a > 0.008mm \ \& \ a \leq 0.03mm \\ 4.725889910130049 \times 10^{-07} & \text{if } a \leq 0.008mm \end{cases} \tag{E.1}$$

$$max\left(\frac{N}{l_{est}^{p}}\right) = \begin{cases} 6.777170820806177 & \text{if } a > 0.75mm \\ 0.514706858179394 & \text{if } a > 0.1mm \ \& \ a \leq 0.75mm \\ 0.011527105382106 & \text{if } a > 0.03mm \ \& \ a \leq 0.1mm \\ 0.003401138722255 & \text{if } a > 0.008mm \ \& \ a \leq 0.03mm \\ 0.004858371372370 & \text{if } a \leq 0.008mm \end{cases} \tag{E.2}$$

$$p = \begin{cases} 0.001 & \text{if } a > 0.75mm \\ 0.1 & \text{if } a \leq 0.75mm \end{cases} \tag{E.3}$$

$$\zeta_i = \begin{bmatrix} -0.00900655941376520 & 0.0234955176645215 & 0.0204180404290648 & 0.0310112615957771 \\ 0.00694225506134393 & 0.00282785801494934 & 0.0593321444685955 & -0.510773848518792 \\ -0.248650671283095 & -0.350741113529932 & -0.0331990630793342 & -0.00461172462528490 \\ -0.0671670949606370 & 3.76874481746282 & 1.16138443162369 & 2.25128005201025 \\ 0.0819976949152733 & 0.00685524083274062 & -0.654998739357619 & -12.1950552414492 \\ -1.34613190741654 & -8.79513766349179 & -0.125580397213464 & -0.00804434144125601 \\ 3.62754944619229 & 15.7046298634835 & -2.72524280276304 & 20.8742611705238 \\ 0.125989278097750 & 0.00638207477869918 & -9.12522528453657 & 0.213918008859322 \\ 0.704534767503835 & -28.1935608542326 & -0.0839701944212565 & -0.00327272346990417 \\ 13.3110897787820 & -11.9633628173177 & 0 & 15.8895483241197 & 0.0367715603049510 \\ 0.00106647389969174 & -11.5364230535061 & -0.341895665116853 & 0 & 7.36471896889013 \\ -0.0101522471417756 & -0.000213012605134284 & 5.52213277719602 & -0.0829121056536580 \\ 0 & -14.7476341640874 & 0.00160073558847242 & 2.37618601753438 \times 10^{-05} & -1.12601967864597 \\ 7.56642810991896 & 0 & 5.70427174713219 & -0.000109806286595392 & -1.13306287527313 \times 10^{-06} \end{bmatrix}^T \tag{E.4}$$

$$\zeta_{ii} = \begin{bmatrix} 0.00274534702759858 & 0.00570062504586821 & -0.0150692565514790 & 0.0160611117854582 \\ -0.00530238052013787 & 0.00629634670432414 & -0.00921599612249572 & -0.0773540353511428 \\ 7.61681546236885 & -4.55718626326245 & 0.121108852660213 & -0.348701406897452 \\ 0.0568815104258999 & 0.441866566000618 & -1643.01150559212 & 389.350377223878 \\ -6.54752120587821 & 10.5365042224893 & -0.271896561306082 & -1.13162262793539 \\ 160982.094099435 & -16520.1279303398 & 280.895184024591 & -188.727683473797 \\ 0.866098497702244 & 0.943735564644804 & -5405121.70229425 & 373549.849045294 \\ -6479.18489142354 & 2068.26874026095 & -1.87483855074376 & 0.644942440373053 \\ 0 & -4282015.21999903 & 85988.0060966366 & -14212.0773385594 & 2.72844683730134 \\ -0.670978302576738 & 0 & 19498252.0608915 & -683024.497615056 & 61427.7714166337 \\ -2.52883366845141 & 0 & 0 & 0 & 3210581.40451703 & -162039.921940290 & 1.33377264799862 \\ -2.51765818405344 & 0 & 0 & -8238518.10098416 & 238142.927021956 & -0.302186515292112 \\ 2.71262791354819 & 0 & 0 & 8896513.99625433 & -149320.559132094 \end{bmatrix}^T \tag{E.5}$$

$$\zeta_{iii} = \begin{bmatrix} 0.000138239374424293 & 0.000758383579628823 & -0.0163022171512385 & 0.0707815960004926 \\ 0.0369149051070974 & -0.00366918971744654 & -0.00231537058483783 \\ -0.00117253238901906 & 1493.06509524443 & -104.091946008691 & -30.6582293632139 \\ 4.54173790777281 & 0.0357565513982684 & -0.0270010469764871 & -3996329.26290791 \\ 58857.1208219742 & 10486.8277111944 & -1334.88844851506 & -0.273482179004119 \\ 0.109613260068148 & 0 & 0 & -1225036.77213007 & 140124.673274442 & 1.17134979627851 \\ -0.0560983581766418 & 0 & 0 & 0 & -4608995.99668688 & -3.00857147440226 \\ -0.199975761346076 & 0 & 0 & 0 & 0 & 4.73801078318580 & 0.0469576910294730 & 0 & 0 & 0 & 0 \\ -4.47992172660205 & 0 & 0 & 0 & 0 & 0 & 2.33312008617679 & 0.983985391205596 & 0 & 0 & 0 \\ 0 & -0.514047056748619 & -0.978583876480006 & 0 & 0 & 0 & 0 \end{bmatrix}^T \tag{E.6}$$

$$\zeta_{iv} = \begin{bmatrix} 5.27336591249154 \times 10^{-05} & 0.000114769635433247 & 1.42088022166294 & 0.205683961868445 \\ 0.0634700021681524 & 0.00211453827808398 & 0.00149566931603524 & -0.000222882376544880 \\ -22907.2816436722 & -277.690790878731 & -44.5584324800381 & 3.31547366282596 \\ -0.0608496787524267 & -0.00342896901949640 & 0 & 0 & -16385.1422052932 & 2570.73700019034 \\ 0.826635704602967 & 0.0176943360075441 & 0 & 0 & 0 & 1138359.54058042 & -6.03739100244704 \\ -0.0251207155275042 & 0 & 0 & 0 & 0 & 26.3730487416182 & -0.00432618600032248 & 0 & 0 & 0 & 0 \\ -70.2772911525635 & 0.0219864895712447 & 0 & 0 & 0 & 0 & 110.058001595968 & 0 & 0 & 0 & 0 & 0 \\ -91.5336633498976 & 0.0203443352941708 & 0 & 0 & 0 & 0 & 30.6453059627211 \\ -0.0332319199472199 & 0 & 0 & 0 & 0 \end{bmatrix}^T \tag{E.7}$$

$$\zeta_v = \begin{bmatrix} 0.000165394941931857 & -5.01861139658774 \times 10^{-05} & 6.11981053262675 \\ 1.12059987314967 & 0.306066336670421 & -0.00277078554586443 & -0.00790967120949056 \\ 0.00153554087542543 & -2070173.80180902 & -89634.0223051641 & -10342.3064536609 \\ -40.1478451509181 & 0.395364835444394 & -0.0124338194624916 & 0 & 0 & 0 \\ 593.333172520039 & -5.13754949919667 & 0.04156143452998480 & 0 & 0 & 0 \\ 35.9325848644363 & -0.0544643481215550 & 0 & 0 & 0 & -18036457.0719485 \\ -146.102424279988 & 0 & 0 & 0 & 0 & 0 & 354.180074733055 & 0.0415817123625751 \\ 0 & 0 & 0 & 0 & -501.330547377409 & 0 & 0 & 0 & 0 & 0 & 379.191974688314 \\ 0 & 0 & 0 & 0 & 0 & -117.119577749656 & -0.0248863621248757 & 0 & 0 & 0 & 0 \end{bmatrix}^T \quad \text{(E.8)}$$

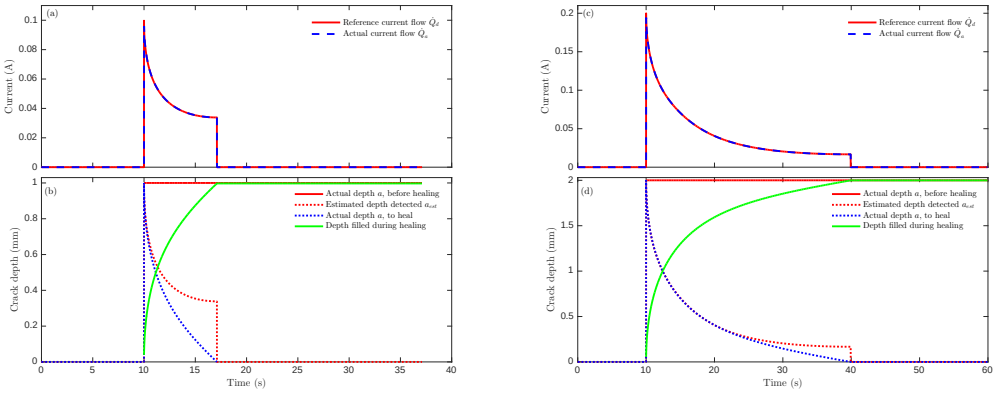

Figure E.1: Crack depth estimation becomes less accurate as crack close up during healing. This is the result of poor diagnosis at lower crack depth

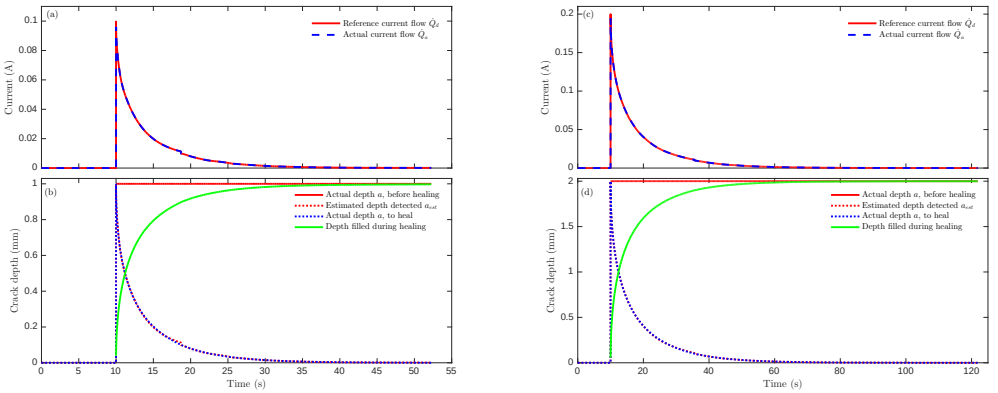

Figure E.2: Illustration of integrated sensing, diagnosis and active self-healing system for (a-b) 1mm crack depth introduced at location 98.4mm. (c-d) 2mm crack depth introduced at location 196.8mm.

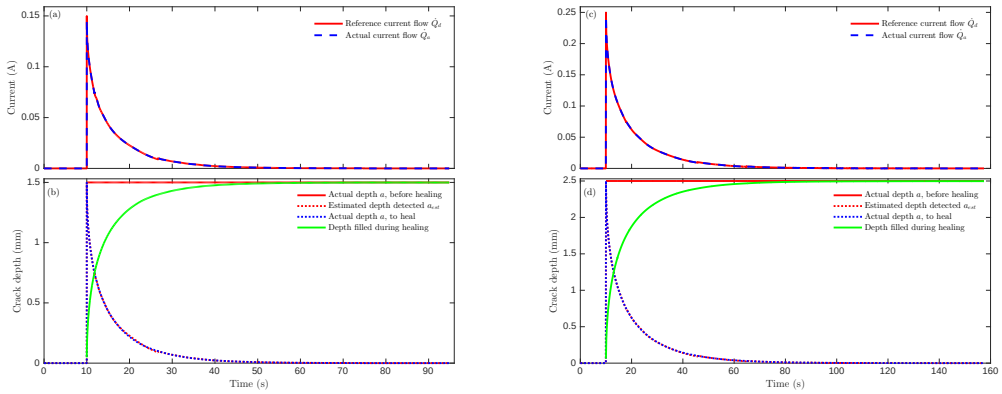

Figure E.3: Illustration of integrated sensing, diagnosis and active self-healing system for (a-b) 1.5mm crack depth introduced at location 393.6mm. (c-d) 2.5mm crack depth introduced at location